ELECTRO-MECHANICAL CHARACTERIZATION OF PIEZO-METALLIC CELLULAR SOLIDS FOR SPINE IMPLANTS

BY

Rodrigo Dennis Perea Camargo

Submitted to the graduate degree program in Bioengineering and the Graduate Faculty of the University of Kansas in partial fulfillment of the requirements for the degree of Master's of Science.

Dr. Elizabeth A. Friis, Chair

Dr. Kenneth J. Fischer

Dr. Sara E. Wilson

Date defended: March 12th, 2010

The Thesis Committee for Rodrigo Dennis Perea Camargo certifies that this is an approved version of the following Thesis:

ELECTRO-MECHANICAL CHARACTERIZATION OF PIEZO-METALLIC CELLULAR SOLIDS FOR SPINE IMPLANTS

Dr. Elizabeth A. Friis, Chair

Dr. Kenneth J. Fischer

Dr. Sara E. Wilson

Date approved: _____

Acknowledgments

I would like to extend my thanks to Dr. Lisa Friis for giving me the opportunity to work in the Biomaterials lab and become part of her team. I am very thankful for her support the one to one meetings and group meetings which made me achieved my objectives towards my work, cleared my future perspectives and became a better investigator. I am very confident that thanks to all her help I have gained the desired knowledge and experience on this biomedical field as well broader my horizons in this biomedical field.

I am also thankful for the help, learning process, and advice given to me by many professors in the bioengineering, mechanical and aerospace engineering departments. I specially thank my committee members Dr. Ken Fischer and Dr. Sara Wilson for spending some valuable time with myself in one to one meeting and giving me advice towards the end goal of this investigation. I would also like to thank the director of the program Dr. Carl Luchies and Leigh Ann Livingston who were always available to talk and solve any concerns presented.

I would like to express my sincere recognition to my lab team who were also supported with me and were always there to discuss any problems or doubts that I had. I specially thank Dr. Nicolas Jaumard who provided me introductory training to continue with my work with patience and enthusiasm. Thanks to the students John Domann and Luis Quiros who were helpful in deliberating and discussing my results and methodologies to overcome difficult situations during my experiments.

Finally, I would to thank my family that were always present and were the main motivation to continue with my career. My parents, Dennis and Miriham who were always supportive with my work and encouraged me to succeed and my sister Paola who I also admired much and love by giving me the motivation to continue my hard work.

Abstract

Many different electrical stimulation methods are currently used to enhance bone growth in spine fusion. In this study, the feasibility of a novel electrical stimulation method using piezoelectric materials embedded into metallic cellular solid structures was presented. The aim of this study was to proof the feasibility to create a new generation of electrically stimulated implants that will mimic and enhance bone osteogenesis in the implanted area while preserving the mechanical characteristics of the environment where are implanted. Cellular composites with different geometric and dimensions were handcrafted and characterized mechanically and electrically. The following study was divided in two parts and was presented in two chapters with the mechanical and electro-mechanical characterization of the structures.

First, structures with no piezoelectric plates were mechanically characterized. Non-linearity at small strain, negative compressive strain ratios (CSR), stress strain curves, modulus of elasticity and their relationship with relative densities were investigated. The feasibility of tailoring the mechanical parameters of the implants to mimic the characteristics of the replaced tissue by controlling its geometry, dimension and aspect ratio was investigated.

Secondly, electromechanical structures (with embedded piezoelectric ceramics) were characterized when compressed axially. Electrical signals, force and displacements were recorded. Alternated electrical signals generated by the piezoelectric ceramics were electrically rectified and then compared to previous direct electrical current stimulators that have proven to enhance bone osteogenesis [1]. The feasibility to create implants that mimic the mechanical behavior of its environment and present embedded electrical stimulation was validated in this study.

Additionally, finite element analysis (FEA) was used to validate the experimental results, design of optimal structures, and understanding in the influence on manufacturing parameters. Models with the same dimensions and geometries were created in FEA and compared to physically tested structures. After the experimental methods were finalized, the feasibility of this investigation and its potential use was discussed while conclusions were brought

Table of Contents

List of Figures

Figure 5-2. Test set up for every structure. Piezoelectric plates were embedded in the middle section of the structure while a non-conducting methyl methacrylate surface was added in the top and bottom surfaces to avoid shortening. Electrical wires soldered into the metallic structures conduct the electrical signal.

Figure 5-3. Electronic circuit to rectified the signal coming from the piezoelectric (Vs) into an essential dc voltage (Vout).

Figure 5-4. Electromechanical structures modeled in FEA with piezo-plates embedded in the middle section of the metallic structure. Boundary conditions are shown in orange: displacement in the top analytics rigid body, x- fixed in the bottom symmetrical section of the bowtie and x-y-fixed in the bottom rigid body.

Figure 5-5a. pXXL1 structure voltage (AC and rectified) when subjected to sine wave compressive cycles up to 0.01 strain at two different frequencies 1Hz (top) and 2Hz (bottom).

Figure 5-5b. Zoomed view of rectified signals at 2Hz (pXXL1). Voltage ripples are shown due to the charging and discharging of the capacitor at the different alternated sine waves.

Figure 5-6. Average strain vs. compressive forces for all the structures at two difference frequencies. There was a small compressive force variation with different frequencies shown by small standard deviations.

Figure 5-7. Average peak to peak voltage output of the structures at the different strain level when subjected to axial strain deformation at a frequency of 1Hz and 2Hz. Standard deviations shown as y-error bars show a great variability in the results.

Figure 5-8. pXXL stress distribution in the y-direction (S_{22}) when fully bonded. Model presents compressive and tensional stresses at the corners of each structure. Very small stresses were presented at the middle surface of the piezoelectric plates.

Figure 5-9. Stress distribution in the y-direction of the pXL model fully bonded.

Figure 5-10. Stress distribution in the y-direction of the pXXL models after separated contact interactions between piezo-plates and metallic structures at the corners. **Figure 5-10.** Stress distribution in the y-direction of the pXL models after separated contact interactions between piezo-plates and metallic structures at the corners.

Figure 5-11. Piezoelectric structures showing the different manufacturing limitations when piezo-plates were bonded into the metallic structures. Successful and unsuccessful bonding is found in the different electromechanical structures.

Figure 5-12. Piezoelectric structures showing the different manufacturing limitations where the piezo-plates were bonded into the metallic structures.

List of Tables

Chapter 1: Introduction

1.1 Scope

It has been proven by several studies that electrical stimulation increases the success rate of bone osteogenesis [8-13]. Electrical stimulation prevents complications with long-term regeneration of bone and promotes a more rapid response in the site increasing osteogenesis**.** The main focus in this study was to evaluate and characterize new piezo-metallic composite grafts for eventual use in spine fusions. It was hypothesized that these novel graft materials will provide electrical stimulation in site while withstanding- the mechanical loading of spine. This investigation improved methods used in a previous study [7] and extended its characterization with additional and new testing methodologies. Re-entrant structures with hexagonal inverted segments similar to bowtie geometries were manufactured with and without embedded piezoelectric ceramics and characterized during this investigation. Piezo-electric ceramics supplied electrical stimulation while the metallic structure bowties provided ductile behavior and compressive load transmission to the piezo-ceramic plates.

Mechanical and electrical behaviors were evaluated from manufactured handcrafted structures. In addition, the structures were mechanically simulated using finite element analysis (FEA) computer software. The mechanical behavior of the physical structures were compared with FEA models created by a commercial FEA software (Abaqus 6.8.2, Simulia Inn, Providence, RI) for better characterization of optimal manufacturing structures. Additional mechanical behavior (such as stress distributions) at interactions surfaces were investigated between the metallic and piezoelectric surfaces. This study provides information to assist future researchers to expand the investigation of these cellular solids that can be used as a potential new generation of bone implants by providing both mechanical and electrical stimuli. The long term goal of this project is to create novel graft materials for spine fusion devices that have controllable mechanical behavior that can be achieved by changing the material

properties, geometry and dimensions of the structure while providing electrical stimulation that could enhance bone fusion.

1.2 Motivation

The motivation for this study is based on the very low success rate of spine fusion. Spine fusion surgical procedures are performed to alleviate pain of a damaged vertebral segment. As mentioned by the American Academy Orthopaedic Surgeons (AAOS), the main reasons for spine fusions are injuries in spinal vertebrae, protrusion and degeneration of cushioning disk between vertebrae, abnormal curvatures of the spine, and/or weak or unstable spine caused by infections or tumors [14]. The use of electrical stimulation has shown to improve the effectiveness of spine fusion procedures, especially in people who have lower success rate due to risk factors such as obesity, diabetes, smokers, people in need of multi-level fusions, or when a second surgical procedure is needed due to a failed primary procedure [15].

Success rates of patients who had undergone anterior and posterior lumbar fusion surgical procedures under electrical stimulation were investigated and compared [14-18]. On average, it was found that the success rate for patients that had direct current electrical stimulation was 95% compared to 75% of a non-stimulated group. Also, patients who were smokers and had direct current stimulation had a much higher success rate of 93% to 71% for non-stimulated smoker patients [17]. Another study showed a higher success rate of 91% for patients who receive direct current stimulation compared to 81% who did not receive any kind of stimulation [15, 18].

Many different methods are currently used to improve spine fusion using electrical stimulation. Each electrical stimulation method has disadvantages such as surgical insertions and removals, patient compliance, electrical power supply for stimulators, biocompatibility, etc. In this study, the feasibility of a new novel electrical stimulation incorporated within the implant itself was examined. This novel stimulation method may eliminate many of the drawbacks of current stimulators. The use of piezoelectric

materials embedded into the metallic cellular structure of the implant is presented where two main advantages are desired. First, this new methodology will present direct electrical current stimulation in the area implanted and secondly, there will be no need of external electrical power supplies. Charges of opposite signs are generated in the piezoelectric ceramics when an adequate mechanical loading is transferred from the metallic structure to the piezo-ceramic embedded into it. These electrical charges will generate electric potentials, which will create charges to flow in one direction generating an electrical current if the structures are not short-circuited. This electrical current will flow throughout a conductive media (metallic structure and conductive tissue environment) and thus generate electrical stimulation into the injured site or implanted area. The use of piezoelectric materials has been studied in fracture healing and biological fixation of hip and knee replacements, but not in spine fusion implants [19-21]. To this author's knowledge, only one patent has been published on use of direct electrical stimulation without the use of electrodes by transforming vibrational energy into electrical energy [22] but no published literate explained the use of piezoelectric materials to provide this kind of stimulation.

1.3 Summary of main goals

The main goal of this investigation was to prove and electromechanically characterize the behavior of piezo-metallic cellular solids. It was assumed that these cellular solids will electrically stimulate bone tissue while providing similar mechanical behavior in the implanted area. The bowtie metallic structures were hypothesized to provide ductile behavior for the overall composite structure while transmitting primarily compressive loads to the piezo-ceramic plates. The behavior of piezo-ceramic-metal composites was studied with physical mechanical testing and the analysis of stress distributions was simulated with finite element analysis (FEA). Abaqus 6.8.2 commercial finite element software was used as a tool to validate, characterize, and expand the results and behavior at the interaction surfaces where stress distribution and mechanical loading were significant to be determined. Two major sections are presented in this thesis. In part one, an extension of previous mechanical characterization on three types of cellular solids

structures is presented. Mechanical structures (with no piezoelectric plates) with different dimensions and/or relative densities were manufactured, tested, and mechanically analyzed using a servo hydraulic machine (Mini Bionix 858, MTS, Eden Praire, MN) when axial cyclic compression was applied up to an adequate strain value to limit the analysis into linear elasticity regions found from previous study [7]. Mechanical characteristics of these cellular solids (such as relative densities and relative Young modulus) were investigated in three different specimen types. In addition, the utilization of FEA as part of the investigation will provide approximate results for optimal manufacturing structures since unavoidable manufacturing limitations and possible experimental testing could lead to erroneous results.

The second part focuses on the electrical characterization such as voltages, electrical currents and electrical resistivity of the piezo-metallic structures. Two types of electro-mechanical structures with similar dimensions as previous mechanical structures but with piezo plates embedded into the middle sections of the metallic cellular solids were manufactured and characterized. Electro-mechanical characterization was done using the same servo hydraulic machine and a data acquisition system (TestStar II, MTS, Eden Praire, MN). Alternate and direct electrical voltages were created when the structures were subjected to axial mechanical loading at frequencies found in normal walking (1Hz and 2Hz). These alternated voltages were converted into direct electrical signals with a simple electronic circuit. In addition, the use of Ohm's law and a known resistor value was used to characterize the direct electrical current and thus compare it with literature on how electrical stimulation levels enhance osteogenesis and increase spine fusion rates [11, 12, 14, 15, 17, 18, 23, and 24]. Electrical current values were recorded when different axial forces were applied.

Finite element analysis with 2D plane strain quadrilateral elements was used to simulate and approximate results for the different structures. The analysis helped elucidate the accuracy in manufacturing and how the structures might behave when subjected to axial compressive forces as done in the experimental testing. Similar relative Young modulus and compressive strain ratio values were recorded

experimentally and computationally for mechanical structures. For the electro-mechanical structures, stresses distributed around the piezoelectric plates were analyzed. FEA approximates the actual behavior of optimal manufactured structures and extended the characterization of the cellular solids by providing useful information of stresses distributed in the piezoelectric plates which are directly related to the voltage being generated. In addition, it supported the variability in the results for similar structure due to manufacturing errors. Piezoelectric FEA was not utilized due to very limited behavior found when piezoelectric elements were used.

After this introductory chapter, a background chapter with extended information is presented. The background chapter presents relevant information of different topics that encompasses this investigation. A methodology chapter (Chapter 3) presents in detailed the manufacturing process, the testing protocol and the number of specimens created for experimental testing. This chapter also presents the procedures to create the finite element analysis simulations. Two more chapters are presented in research manuscript format to submit for publication. Chapter 4 presents the mechanical characterization of novel cellular metallic solids. It was hypothesized that a more controllable metallic cellular solid could yield to a more controllable mechanical behavior which could be tailored to resemble similar mechanical behavior of the replaced tissue (in this case, osseous tissue). This chapter introduces and investigates the main mechanical characteristics of re-entrant cellular solids; these structural materials will be modified to piezoelectric elements in the next chapter. Chapter 5 will discuss the electro-mechanical characterization of metallic cellular solids presented in chapter. The feasibility of producing electrical stimulation is discussed and compared to previous spine fusion stimulators [11]. Finally, in Chapter 6, a brief conclusion and discussion of future work for this investigation is presented.

Chapter 2: Background

2.1 Bone Characterization

2.1.1 Basics of bone

Bone is a lightweight, strong, and hard living tissue, which provides mechanical, synthetic and metabolic functions such as protection for organs, support and movement, blood production, mineral storage, etc. In the cellular level, several types of cells constitute bone. *Osteoblasts* (bone-forming cells) which produce a protein mixture called ostoids mainly made of Type I collagen (the main protein of connective tissue found in animals) that mineralized to form bone. *Osteoclasts* are large cells that break down bone tissue, a process called bone resorption. They come from the main marrow and are found in the surface of old bone which will be dissolved. *Osteocytes* are mature bone cells made from osteoblasts. These cells maintain healthy bone tissue by secreting enzymes and controlling the bone mineral content; they also control the calcium release from the bone tissue to the blood. *Osteogenic* cells respond to traumas, such as fractures, by giving rise to bone-forming cells and bone-destroying cells. Finally, *bone-lining* cells which are made from osteoblasts along the surface of most bones in an adult. Bone-lining cells are thought to regulate the movement of calcium and phosphate into and out of the bone [25, 26].

Wolff's law states that bone in a healthy person will adapt to the loads it is subjected, thus bone grows in response to stress [27, 28]. In addition, bone is piezoelectric and it has been suggested that in some way this is responsible for stress-induced growth. At glance, bone looks fairly solid but most bones are made up of an outer shell of dense *compact* bone, enclosing a core of porous cellular, *cancellous* bone. It is worthwhile to understand the mechanical behavior of cancellous bone when dealing with several biomedical applications since most of the bone replaced (artificial hips, vertebrae, etc) is cancellous. Fractures are mostly common due to a reduction in the amount of cancellous bone in the affected areas. Cancellous mass bone varies between patients as the mass of bone decreases over time in a extend that fractures could occur

even under normal healthy conditions. The mismatch of properties between orthopedic implants and the surrounding bone is thought to be one reason that they work loose. Thus, high variation of cancellous bone between different patients brought difficulties in creating effective implants.

Vertebral Column

Some of the functions the vertebral column have are protection of spinal cords and nerve roots, base of ligaments, muscles and tendons, support for head, shoulders, chest, connection of upper and lower body, balance and weight distribution, flexibility and mobility, mineral storage and production of bone cells.

It is formed of thirty three vertebrae categorized as irregular bones. These vertebrae are divided into four different regions: cervical, thoracic, lumbar, and pelvic (Figure 2-1). The cervical region is the most superior region and is composed of 7 vertebrae (C1-C7). It is subdivided into two parts: the upper cervical region (C1 and C2) and the lower cervical region (C3 through C7). C1 is called the Atlas and C2 the Axis. The Atlas supports the skull and it is different in appearance from the other spinal vertebrae. The Axis provides a type of pivot and collar allowing the head and Atlas to rotate. The next region is the thoracic region where 12 vertebrae are present (T1-T12). These vertebrae increase in size from T1 to T12. The rib cage is joined to the thoracic region with the exception of T11 and T12 which are called “floating ribs”. The thoracic spine’s range of motion is limited due to many rib/vertebrae connections.

Next, there is the lumbar region composed of L1-L5 vertebrae. They are similar in size and it is where much of the body’s weight is withstood. It is the region related to the biomechanical stress. The last region is called the pelvic region where the sacrum and coccyx are located. Five bones (S1-S5) fused into a triangular shape and it forms the sacrum. Right after the sacrum, there are five additional bones fused together to form the Coccyx or tailbone [29].

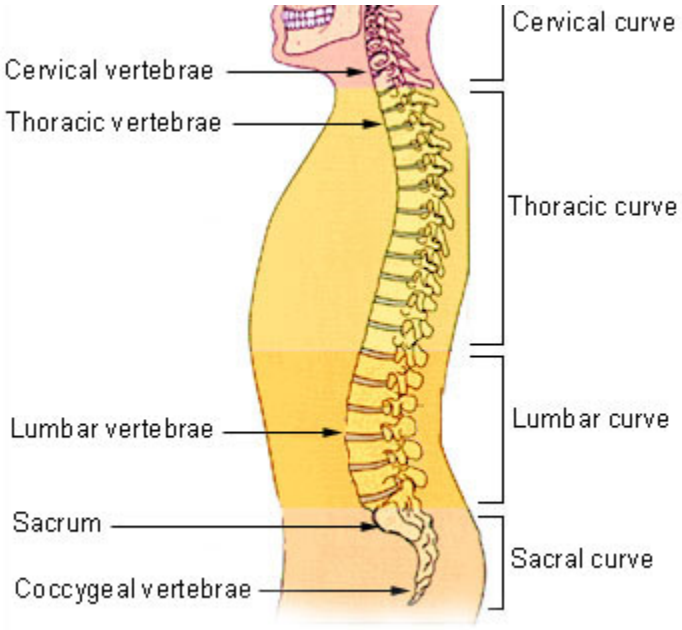

Figure 2-1. Vertebral column (This is a file from the Wikimedia Commons, a freely license media file repository).

Lumbar Vertebrae

The lumbar spine region is where the body weight is supported and thus it is subjected to the largest stresses in the body. It is also the region most of the vertebral stress-induced injuries are located [30]. It is composed of five vertebrae similar in shape. Figure 2-2 shows the main components of a single vertebra located in the lumbar region. There exists two essential parts in a lumbar vertebra: the vertebral body and the posterior part of the vertebra. The vertebral body has a cylindrical shape and provides support for movements, sitting, standing and walking. It is mainly composed of trabecular (cancellous) bone with a cortical bone section surrounding the intervertebral body (as shown in the figure). The top and bottom surfaces of the vertebral body are rough and flattened for easy attachment of the intervertebral discs (IVD) that connects each vertebra. The IVD is the cause of pain in this region when malfunction. The posterior

section of the vertebra is a combination of irregular bones. Pedicles are thick processes that project from the intervertebral body and are made of thick cortical bone making it very stiff. Extending from the pedicles, there is the lamina. Between the anterior and posterior regions of the vertebrae, there is a section called vertebral foramen which its main function is to protect the spinal cord.

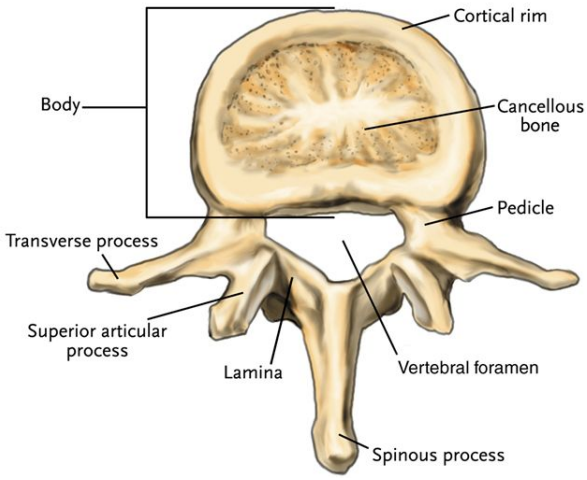

Figure 2-2. Main components of common vertebrae found in the lumbar spine region [5]. “Reprinted from [5] with permission from Medtronic Inc”

Intervertebral Discs

Intervertebral discs (IVDs) are found between each vertebral body. There are fibro cartilaginous cushions serving as shock absorbers which protect the vertebrae [30]. The intervertebral discs are subjected to considerable variety of forces and moments. Along with the facet joints they are responsible for all the compressive loading the trunk supports. Is has been determined that the force on a lumbar disc when a person is sitting is more than three times the weight of the trunk [31]. IVDs constitute 20-33% of the entire height of the vertebral column. IVDs are composed of three distinct parts: the nucleus pulposus, the annulus fibrosus, and the cartilaginous end plates. The *nucleus pulposus* is a centrally located area where the water content range from 70-90%. It is highest in birth but tends to decrease with age [32]. The nucleus pulposus fill around 30

to 50% of the total area in cross-section at the lumbar area. The *annulus fibrosus* forms the outer boundary of the disc. It is composed of fibrous tissue in concentric laminated bands. The fiber are arranged in a helicoids manner and are attached to the cartilaginous end planes in the inner zone, while in the more peripheral zone they attach directly into the osseous tissue of the vertebral body. The *cartilaginous end plates* are composed of hyaline cartilage that separates the other components of the IVD to the vertebral body. An active growth of the cartilage is present at very short ages but it starts to disappear with time and is replaced by bone.

The compression test has been the most popular mechanical test for the study of IVD due to its major compression-carrying component of the spine. Typically, the load-displacement curve with concavity towards the load axis initially followed by a straight line implies little resistance at low loads and thus non-linear behavior. However, when the load increases, the disc becomes stiffer. They could probably answer why the flexibility at low loads and stability at high loads.

Intervertebral discs constitute the largest organ without own blood supply. Proteoglycans soak up nutrients and water as they move. However, when this gaining of nutrients is blocked due to incorrect repetitive moving or poor posture, then they become thinner and more prone to injury. If this process increases over time, then gradual regeneration of the intervertebral disc is conceived causing low back pain and chance for surgery.

Procedure and Treatment of Herniated IVDs

Repeatedly incorrect postures, moving, injury, normal wear and tear, disease, and overweight may cause the IVDs to bulge abnormally or break (Figure 2-3). This bulge or break abnormalities are called herniated or slipped disc abnormalities. If the herniated disc presses on a nerve root, it may cause pain, numbness, tingling, muscle spasm or cramping, and leg weakens or loss of leg function [6].

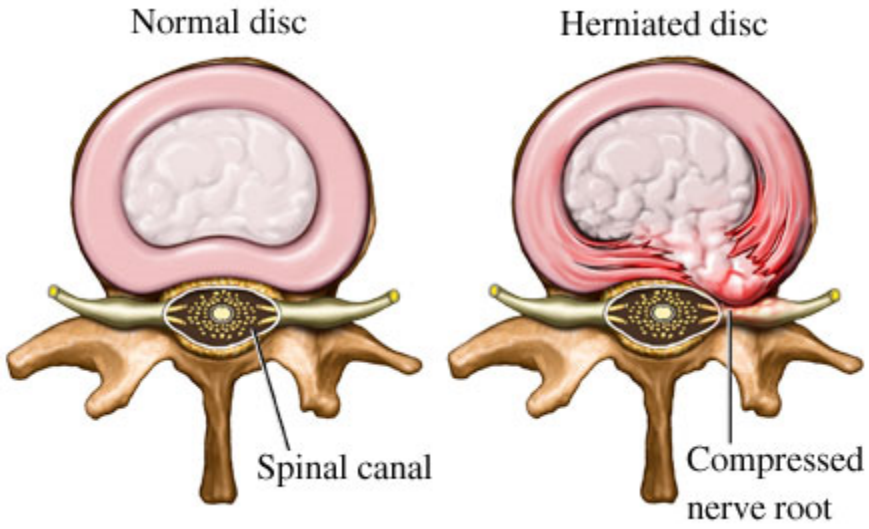

Figure 2-3. Top view of a normal vs. herniated disc with a cracked region in the annulus pulposus. Disc herniation occurs when the annulus fibrous beaks open or cracks, allowing the nucleus pulposus to escape.[5]. "Reprinted from [5] with permission from Medtronic Inc"

A herniation could develop suddenly or over weeks or months. Four major stages are presented. The first stage is known as disc degeneration where chemical changes associated with aging causes a disc to degenerate but with no herniation. The second stage is called prolapse, where the form or position changes called bulge or protrusion. Extrusion is the next stage where the nucleus pulposus breaks through the annulus fibrosus wall but remains within the disc. The final stage is called the sequestered disc or sequestration where the nucleus pulposus breaks and lies outside the disc in the spinal canal.

Spine surgery is suggested when non-surgical procedures alleviate the symptoms cause by herniated discs. Discectomy, which involves removal of the IVD and spine fusion are suggested as the long-term solution. Spine fusion also known as spondylodesis or spondylosyndesis is a technique used to combine two or three vertebrae. This procedure is achieved in many ways and through several different techniques. Anterior or posterior procedures approaches (in some cases both) are determined by the surgeon once x-ray studies are investigated [33]. Titanium screws usually attached to a rod or plate

contoured to your spine may be used typically placed through the pedicle bone. These screws will present immediate strength to your spine during the process of spine fusion. Other procedures may include a titanium metal “cage” or bone cylinder placed into the IVD space called the interbody fusion [33]. Graft materials typically accompany these procedures. Most common graft materials are bone autografts taken from the patients’ pelvis (ileum) or tailbone (spinous processes and laminar bone) yielding to a second surgical procedure. Other graft materials include biodegradable bone composites under investigation [34]. The main function of these grafts is to immediately serve as a load-bearing substance and also be gradually replaced by host bone.

The healing process of a spine fusion can take months or over a year in some cases to be completed. A successful spine fusion is very rare being lower in patients who smoke, are overweight, have diabetes or other significant illnesses, have osteoporosis, or who have had radiation treatments that included the lower back. Good nutrition and slowly increasing activity can help achieved success. Also, a new development of electrical stimulation can enhance the healing process and increase the success rate. Kane et al. [15] has shown, in a randomized prospective that electrical stimulation improves the success rate in spinal fusion. A control group of 28 patients had a fusion rate of 54%, and the group of 31 that was electrically stimulated fused at an 81% rate ($p > 0.005$).

2.1.2 Bone Mechanics

The most accurate implantable device is the one that resembles most accurately. Many researchers in many biomedical fields have tried to resemble similar characteristics with different implantable devices such as cardiac assist devices, limb implants (hip, leg or shoulder implants), stents and/or spine fusion implants, etc. In spine fusion, current implants need to present similar properties in the linear region such as mechanical stiffness or yield strength to resemble the major characteristics of its environment. In the case of spine fusions, the environment to resemble is mostly the vertebral body consisting on compact and cancellous bone. Thus, implantable materials specially adapted for bone spine fusion such as screws, cages, or grafts need to present adequate behavior similar to

the vertebral bodies. Mechanical properties such as density or porosity, strain behavior, degeneration and fragility, directionally (anisotropy in case of cancellous bone) would need to take in consideration when implants are manufacturing.

Relative Density and Porosity

Bone is composed in two kinds of bone, cortical bone and cancellous bone. Bone looks mostly solid; however it enclosed a core of porous cancellous bone. Cancellous bone has similar mechanical behavior as most common cellular solids. Thus, the presence of cancellous bone reduces weight while still meeting its primary mechanical function. Gibson and Ashby [2, 15] mentioned that the single most important feature of any cellular solid and such, cancellous bone is its relative density ρ^*/ ρ_s, which is referred as the density of the cellular solid divided by the density of its material which it is made or a function of a ratio between the length and the thickness of the cell members [7, 15].

The cellular structure of bone is made up of interconnected network of rods or plates. At lowest densities the cells are open, like a network of rods. However, as density increases the rods progressively spread and flatten becoming more plate-like and finally fuse to almost closed cells. Relative density of cancellous bone varies from 0.05 to 0.07 [2]. Compact bone presents higher relative density values. It presents high compressive strength but poor tensile strength which resists significant compressive forces but not tensile loading. In some areas (as at joints between vertebrae or at the end of long bones) the design and presence of cancellous bone minimizes the weight of bone while still providing a large bearing area. Porosity though varies between each individual and thus it is difficult to find adequate standard values. The causes of different porosity could be due to age, diseases such as osteoporosis or gender. There is a high level of porosity in cancellous bone relative to cortical bone. This porosity leads to more free surfaces and thus to more of the cellular constituents that inhabit those surfaces. Thus, cancellous bone is more responsive to stimuli than in cortical bone. As Jacobs [35]

suggested, this extends the relationship between cancellous bone's internal structure and external mechanical loading.

Non-linear Behavior at Small Strains

Due to the different discrepancies on what is actually occurring at small strains (below 1.2% strain), it is highly important to mention the current studies of bone at these strain levels. Morgan et. al[36] studied 155 cylindrical cores from human vertebrae, proximal tibiae, proximal femora, and bovine proximal tibiae to characterize the subtle concave downward stress-strain non-linearity. Tension and compression axial testing up to 0.4% strain was performed. Concave downward nonlinearity in the initial stress-strain curve was found for all anatomic sites in both compression and tension. However, other investigators [37] concluded that the pre-yield behavior for every specimen was fully linear indicating that the non-linear 'toe' is due to an experimental artifact.

Currently it is unclear if there exist a non-linearity characteristic in cancellous bone at small strains and what possible reasons could provide this behavior. One possible cause could be the damaged generated at these low strains serving as a remodeling stimulus [38-40].

2.1.3 Electro-mechanical studies in bone

Since the 1950s bone piezoelectricity has been studied arising great perspectives and new ideas on the bone electro-mechanical behavior [41]. Chakkalakal [42] suggested that two possible mechanisms are responsible for this effect: classical piezoelectricity due to molecular asymmetry of collagen in dry bone, and fluid flow, possibly streaming potentials in wet bone [43]. Electronegative potentials are found in areas of compression while electropositive potentials are found in areas of tension. It has been hypothesized that this electric field may form the basis for bone remodeling and in response to

mechanical stimuli (Wolff's Law). Bone forms in electronegative regions [44, 45]. Electric fields are also generated at injury sites in soft tissue and bone (injury-induced potentials) and at areas of active bone formation such as at the growth plates of developing limbs [11].

It is unclear whether dry or wet bone exhibits similar piezoelectric characteristics [46, 47]. Fukada and Yasuda [48] demonstrated that dry bone exhibits the piezoelectric effect by applying mechanical stresses or electric fields as a converse effect while other investigators such as Reinish et. al [49] demonstrated that the piezoelectric effect in wet bone occurred in the kilohertz range, when subject to different frequencies, above any physiological significance. Piezoelectric properties of bone [50] and dielectric properties [51] are frequency dependant. The magnitude of the piezoelectric sensitivity coefficients of bone depends on frequency, on direction of load, and on relative humidity. Values up to 0.7pC/N were observed [50].

The dielectric permittivity, which determines capacitance, can exceed 1,000 partially in hydrated bone. It was found that the dielectric permittivity bone increases dramatically with increased humidity and decreased frequency [49]. The resistivity of bone is about 45-48 ohm-m for the longitudinal direction, and three to four times greater in the radial direction [52]. Since the physiological saline solution has a resistivity of 72 Ω-m, it can be said that bone under conditions of fully hydrated saline solution behaves differently than actual wet bone. Since the resistivity of fully hydrated bone is about 100 times greater than that of bone fewer than 98% relative humidity, it is suggested that at 98% humidity the larger pores are not fully filled with fluid [42].

In addition of electric polarization and piezoelectric characteristics, compact bone also exhibits pyroelectricity (change of polarization with temperature) due to the polar structure of collagen molecule attributed to the polar collagen molecule oriented in bone [53-55]. It is still unclear whether wet bone present piezoelectricity at relatively low physiological frequencies. However, these electrical properties are relevant for bone remodeling and electrical stimulation either in internal or external methodologies explained later in this chapter.

2.1.4 Spine Bone Stimulators

Bone healing due to electrical stimulation first came from the information of bone tissue electrical properties by Yasuda, Basset and Becker [41, 56, and 57]. Due to the effect on bone when some electric fields are applied, various electrical stimulation devices have been designed to deliver this field to enhance bone, primarily for spine fusion. Several electrical stimulations therapies have been investigated for more than thirty years [11, 12, 14, 15, 17, 18, 24, 58, and 59]. The many devices can be categorized in two sources of electrical stimulation: direct and indirect electrical stimulation. Direct stimulation consists in surgically implanted electrodes that provide low level electrical signals from a battery to the area inserted. On the other hand, indirect stimulators are non-invasive devices that provide electrical stimulation from electrical or electromagnetic fields. The FDA has approved three types of electrical stimulation technologies for clinical use: direct current (DC), capacitive coupling (CC), and inductive coupling (IC) such as pulsed electromagnetic fields (PEMF) and combined magnetic fields (CMF).

Direct Electrical Stimulators

Direct electrical stimulation (DC) devices consist of electrodes that are surgically inserted in the site of fusion, mostly made out of titanium. These electrodes act as cathodes and are connected to a hermetically sealed power supply acting as the anode. These electrodes can vary by size, configuration, and materials and will create a constant localized electrical current in the area where implanted. Accompanied with normal physiologic regulators of bone formation, this localized electrical current demonstrated to improve the success rate of spine fusion [15, 16, and 60]. In vivo studies show that advances healing were found in different levels of electrical current changing from .05μA-100μA of direct current [3, 6, 57, and 58]. Higher values of direct electrical current have shown to produce necrosis at the area of stimulation [57].

The first reported clinical study using DC to enhance spinal fusion was in 1988 [15]. The results of three independent studies were published in this article. In the first

study, it was found that patients under DC stimulation had a success rate of 91.5% compared to 80.5% of the control group. The second study considered population with previous failed fusions, patients with grade II or worse spondylolistheis, patients with multiple level fusions and patients with other risks such as obesity, smoking and diabetes. The populations with DC stimulation had a success rate of 81% compared to 54% in the control group. The third study with population in the second study with uncontrollable group was evaluated. A success rate of 93% was reported. In 1994 other investigation [17] presented patients undergoing anterior and posterior lumbar interbody fusions with allograft. The DC-stimulated group had a 92% success rate versus 71% in a non-stimulated group. During post lateral fusion, another study was carried out on patients undergoing posterior spinal fusion with and without pedicle screw instrumentation [60]. DC stimulated group had a success rate of 96% compared to 85% in the control group. Smokers were also found to heal better with a success rate of 83% compared to 66% in a control group. Patients undergoing spinal fusions without instrumentation showed also a success rate that varied between 91 and 93% in a median 5-year follow up period [16].

Indirect Electrical Stimulators

Currently non-invasive indirect electrical stimulators are categorized in two technologies: capacitive coupling and inductive coupling. Capacitive coupling (CC) electrical stimulators consist of electrodes with conductive gel placed paraspinally on the skin. These electrodes are connected to an alternating current (ac current) signal generator and produce an electric field. A multicenter randomized double-blind study carried out by Goodwin et al. [61] showed a statistically higher success rate in the CC-stimulated group (85%) compared to in the control group (65%).

Inductive coupling is another non-invasive technology consisting of external current-carrying coils driven by a signal generator. A magnetic field is produces which

induces a secondary electric field at the fusion site. These coils are worn across the area of spinal fusion for about 3-8 /day for 3-6 months depending on the study and the therapy the patients are given. Two kinds of capacitive coupling have been approved by the FDA: pulsed electromagnetic fields (PEMF) devices and combined magnetic fields (CMF). CMF differs from PEMF in that it is made up of a time-varying magnetic field superimposed on a static magnetic field. Most investigations have been performed with the PEMF signal, which is FDA, approved for fracture healing but not for spinal fusion [62-65]. Only one study was clinically approved for spinal fusion [66] while few studies with CMF [23, 67, 68]. Clinical efficacy of PEMG was first reported in 1985 where 13 patients with established pseudarthrosis undergone posterior lumbar interbody fusion. It was reported that 77% of patients with healed interbody pseudarthrosis [69]. The fusion rates were found to be dependent on patient compliance in wearing the PEMF unit. Spine fusion rates were significantly lower than demonstrated with DC stimulators. There is only one published clinical study on the use of CMF for spinal fusion [70] showing a success rate of 64% in the CMF-treated group compared to 43% in the control group for 201 patients who went under non-instrumented posterolateral spinal fusions. CMF appeared to be effective only in women; fusion rate were not enhanced in men.

As shown by previous investigations over the past 30 years, studies shows that direct electrical stimulation to be superior to indirect technologies particularly when used to treat posterior spinal fusions. The main focus in this investigation is to combine direct electrical stimulation in bone with graft materials such as cages to enhance bone osteogenesis with direct electrical stimulus and an adequate mechanically similar graft. If validation of these new kind of implants is successfully proven, a new generation of graft materials could be vision, study and investigated for more optimal success rates.

2.2 Cellular Solids

A cellular solid is one made up of an interconnected network of solid struts or plates which form the edges and faces of cells [2, 71]. Foaming cellular solids extend greatly the range of properties for different applications. Almost any material can be a porous making polymer the most popular. Metals, ceramics, glasses and even composites can be fabricated into cells. There is a great variation on the applications of cellular solids such as thermal insulation, packaging, structural, buoyancy, filters, water repellants membranes, etc. These cellular solids present physical, mechanical and thermal properties, which are measured by the same methods use for fully dense solids.

The single most important characteristic of the solids according to Gibson and Ashby [2] is its relative density. Another important characteristic of cellular solids is the shape of the cell that creates the solid. As an example, when the cell shape is equiaxed, the properties are isotropic, but when the cells are even slightly elongated or flattened the properties depend on its direction. At first, one might suppose that *cell size* is also an important parameter but almost every mechanical and thermal properties depend only weakly on cell size as stated [2].

2.2.1 Cell Shape

Two-dimensional cellular cells present less variation than three dimensional cell shapes. In two dimensions, even when the cell shape is fixed, the cells can be stacked in more than one-way giving structures different edge connectivity, and different properties. Possible two dimensional man-made honeycomb shapes are triangles, squares, parallelograms, regular hexagon or irregular hexagons. Natural two-dimensional cells are less regular. Some examples of natural two dimensional cells are the soap foam between glass slides, the cells of the retina of the eye, even the bee’s honeycomb [72]. These

natural two-dimensional cells contain elements of randomness, which are visible as four, five, seven and even eight-sided cells. In three dimensions, a greater variety of cell shapes are possible. They must be packed as two dimension cells to fill a space. Some examples of undistorted three-dimensional cellular shapes include triangular, rhombic and hexagonal prisms, the rhombic dodecahedron (a body with 12 diamond-shape face) and the tetrakaidecahedron (a body with six squares and eight hexagonal faces). However, most foam are not regular packing of identical unit but contain cells of different sizes and shaped with differing numbers of faces and edges. Even most random cell shapes of foams in two or three dimensions obey topological rules as those govern by honeycombs and precise and useful statements can be made about them.

Two dimensional hexagonal shape cells with inverted segments were manufactured and characterized during this investigation. It was expected as one of the main characteristics that the structures, due to its inverted segments, will provide negatively Poisson values. Foams with negative Poisson ratios present a re-entrant behavior. As hypothesized, this cell should present non-linear behavior that will be on characteristic tested in this study. According to Gibson and Ashby [2], by knowing the cell shape and size, the mechanical properties could be tailored and modified for an desired behavior. If a controllable cellular solid is created, it can be modified to behave similar to the tissue is being replaced (in this case osseous tissue).

2.2.2 Relative Density

The single most important structural characteristic of a cellular solid where all foams and honeycomb depend are their relative density ρ^*/ ρ_s, which is referred as the density of the cellular solid divided by the density of its material which it is made or a function of a ratio between the length and the thickness of the cell members [2, 7, 72]. The relative density of the cellular solids depends on the thickness and length of the

structure. The proper choice of these equations depends on the dimensionality of the structure (honeycomb or foam) and the presence of open or close cells:

If the cell edge length is l (letter l) and the cell wall thickness is t, and t << l, the relative density is low-then for all honeycombs:

$$\frac{\rho^*}{\rho_s} = C_1 \cdot (\frac{t}{l}) \qquad \text{[Eq. 2.2.1]}$$

for all open-cell foams with edges of length l and thickness t:

$$\frac{\rho^*}{\rho_s} = C_2 \cdot (\frac{t}{l})^2 \qquad \text{[Eq. 2.2.2]}$$

and for all closed cell foams with faces of side l and uniform thickness t:

$$\frac{\rho^*}{\rho_s} = C_3 \cdot (\frac{t}{l}) \qquad \text{[Eq. 2.2.3]}$$

,where the Cs are numerical constant, near unity, that depend on the details of the cell shape.

For most purposes the mechanical behavior is calculated in terms of t and l and converted to relative (equations 2.2.2 to 2.2.3) while constant values determined by simple experimental measurements. The relative density of the bowtie cellular solid characterized in this investigation is shown in Eq. 2-4 by Jaumard [7]**:**

$$\frac{\rho^*}{\rho_s} = \frac{Occupied\ Area}{Total\ Area} = \frac{\left(\frac{width}{length}+1\right)\cdot\frac{t}{l}}{\left(\frac{width}{length}-\sin(\theta)\right)\cdot\cos(\theta)} \approx \frac{4}{\sqrt{3}}\cdot(\frac{t}{l})$$

,for θ equal to 60 degree. [Eq. 2.2.4]

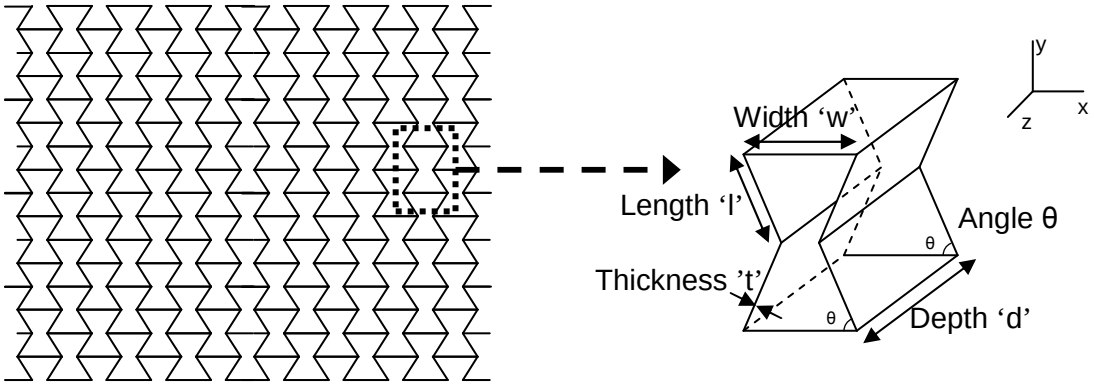

Figure 2-4. Schematic of the open hexagonal cellular solid with inverted segment cells.

2.2.3 Mechanical Behavior of Cellular Solids

The mechanical behavior found in a two-dimensional honeycomb cellular solid (Figure 2-4) depends on the plane where the mechanical loading is applied. During and *in plane* deformation (components of stress acts in the X-Y plane), the structure present the lowest mechanical stiffnesses and strength because this plane makes the cell walls to bend. On the other hand, the *out-of-plane* properties (components of stress acting in the Z direction), the stiffnesses and strengths are much larger because they require axial extension or compression of the cell walls. Mechanical loading during this investigation is focused only on the *in-plane deformation*.. Figures 2-5 shows how a cellular solid behaves under compressive stresses for three different honeycomb materials: an elastomeric honeycomb (a rubber), and elastic-plastic honeycomb (a metal) and one which elastic-brittle properties (a ceramic). All of these curves present similar behavior with a linear-elastic regime followed by a plateau region of constant stress. Finally, a steeply regime where an increase in stresses can be seen. The first “linear” region in the curves is presented due to a bending of the cell walls. However, once a critical stress in reaches, the cell begins to collapse and thus the plateau region begins. Depending on the material, the collapse could be recoverable or not. Elastomeric materials, collapse is shown by elastic buckling of the cell walls, and thus it is recoverable. Similar properties have the plastic materials, the collapse occurs by the formation of plastic hinges at the

section of maximum moments making it recoverable as well. However, in brittle materials (e.g. ceramics), the cell walls go under brittle fractures and thus the collapse is not recoverable. The last region in the graph shows that at high strains, the cells collapse sufficiently that opposing cell walls touch or broken fragments pack together giving a steeply rising portion of the stress-strain curve known as densification.

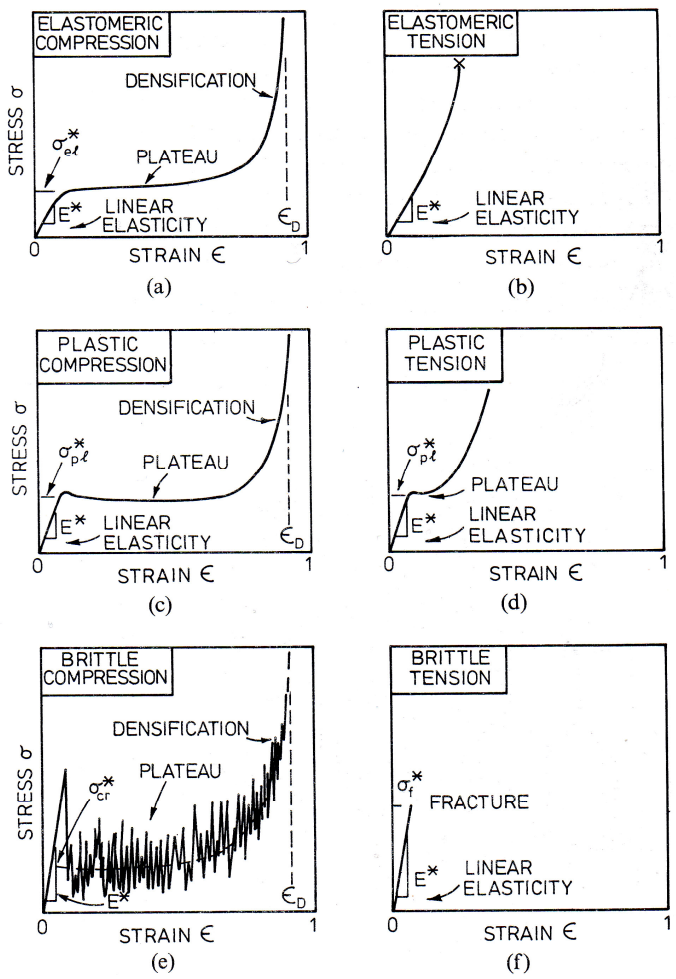

Figure 2-5. Compressive and tensile stress-strain curves for honeycombs: (a) and (b) present an elastomeric honeycomb (rubber); (c) and (d) an elastic-plastic honeycomb (metal); (e) and (f) an elastic-brittle honeycomb (ceramic) [2].

While the relative density of the structures increases, the relative thickness of the cell walls also increases. This will give a higher resistance for the cell walls to bend and cell collapse goes up, giving a higher modulus of elasticity and plateau stress. Also, since the thickness of the cell walls is higher, the densification region will occur sooner, giving a rise in the curve at a sooner time. Figure 2-6 shows how the stress-strain curve varies with loading in compression in the x plane, showing the linear-elastic, collapse and densification regimes, and the way the stress-strain curve changes with t/l ratios or relative densities. During this investigation, we will mainly focus our attention into the first linear region at small strain values. Mechanical properties found by Jaumard [7] from similar structures with similar relative densities provided safe strain values where the structured analyzed are maintained in the "linear" region.

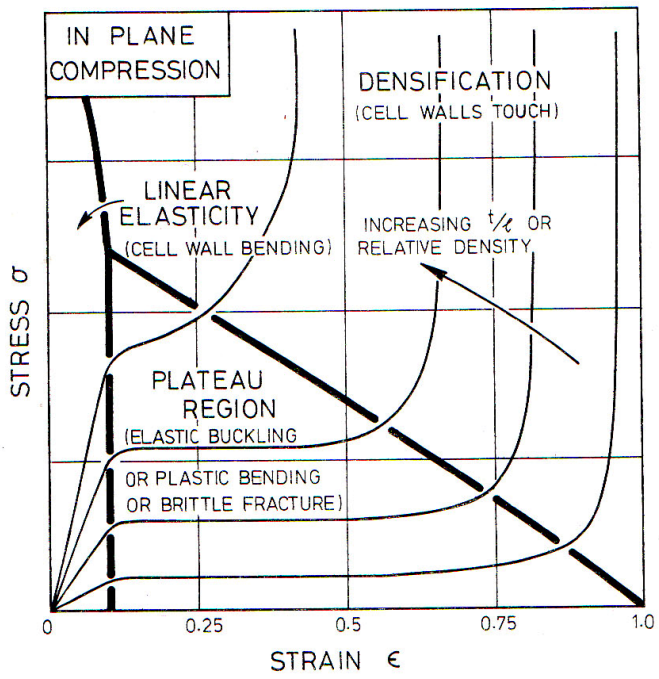

Figure 2-6. Linear-elastic collapse, densification regimes, and the way stress-strain curve changes with t/l when loaded in compression in the x plane [2].

Non-linear Behavior Re-entrant Cellular Solids and Comparison to Bone

The findings of previous study by [71, 73] showed that mechanical properties of open foam cell with re-entrant behavior reported nonlinear stress-strain relationship at small strains for re-entrant copper. The cellular solids were obtained via sequenced tri-axial compression of standard foam followed by annealing. Thus, no control of the pores was provided and thus they remained randomized. Due to the hypothesized made by Jaumard [7] and worked done by Gibson and Ashby [2] a more controllable solids will yield to a more controllable nonlinear mechanical behavior. Mimicking the investigations where bone behave non-linear at small strains [10-12, 37, 61] and a controllable non-linear cellular solid will lead to a better mechanical behavior similarity between the implant and the area where it will be implanted.

This investigation will present the validation of non-linear mechanical behavior of previous manufactured structures [7] at small strains. Previous manufacturing process was improved and new 2D dimensional bowtie structures were subjected to similar axial compression within the elastic region. Comparison with previous structures were discussed and additional finite element analysis with commercial computer software was utilized to validated whether the mechanical results were acceptable or whether other conditions could lead to incorrect conclusions

2.3 Piezoelectricity

Piezoelectric is the ability of crystalline materials to develop an electrical charge proportional to its mechanical stress and vice versa [74]. When a piezoelectric material is squeezed, an electric charge is generated on its surface. Conversely, when a piezoelectric material is subjected to a voltage, it mechanically deforms. The brothers Pierre and Jacques Curie discovered the piezoelectricity effect in 1880. The name comes from the Greek definition "*piezien*" which means to press or squeeze.

There exist over a thousand piezo electrical materials, each one with different mechanical and electrical characteristics. The materials are cataloged according to its use and functionality. Piezomaterials have been used in the last century as the key components of sensors, transducers and actuators due to its peculiar electro-mechanical characteristics. Piezoelectric materials are divided in four categories: piezoelectric crystals, piezoelectric fibers, piezoelectric ceramics and piezoelectric polymers. Two of the last categories are more frequently used [75] . Piezo electric ceramics are very well developed and its use is not expensive while providing fair strength, stiffness and excellent piezoelectricity. A common piezo-electric ceramic is the Lead Zirconate Titanate (PZT), which is the main candidate for smart materials and structures. This material was currently used in this investigation

According to Jaffe [76], there were three basic steps in the discovery and understanding of piezoelectricity. The first of these steps is the discovery of a high dielectric constant or relative permittivity. The second step was to realize that the main cause of the high dielectric constant was ferroelectricity. Ferroelectricity is the appearance of a spontaneous electric moment in a crystal that changes its orientation when subjected to an electrical field. This discovery occurred at the Laboratory for Insulation Research at MIT [77]. The third step was the discovery of the poling process. Poling refers to the application of a high voltage sufficient to reverse electric moments of spontaneously polarized regions in the ceramics (Figure 2-7). As mentioned before, these ceramics present spontaneous electric moments. Once these electric moments are subject

to an electric field (Figure 2-7b), these spontaneous moments are rearranged in the direction of the electric field at an adequate temperature where its ferromagnetic properties will not be lost. The limit temperature where it starts losing its ferromagnetism properties is known as the Curie temperature. After the polarization treatment, most domains or electric moments are nearly aligned with the previous electric field and are maintained after the removal of the electric field. The material now presents permanent polarization closely similar to where the electric field was present **(Figure 2-7c)**.

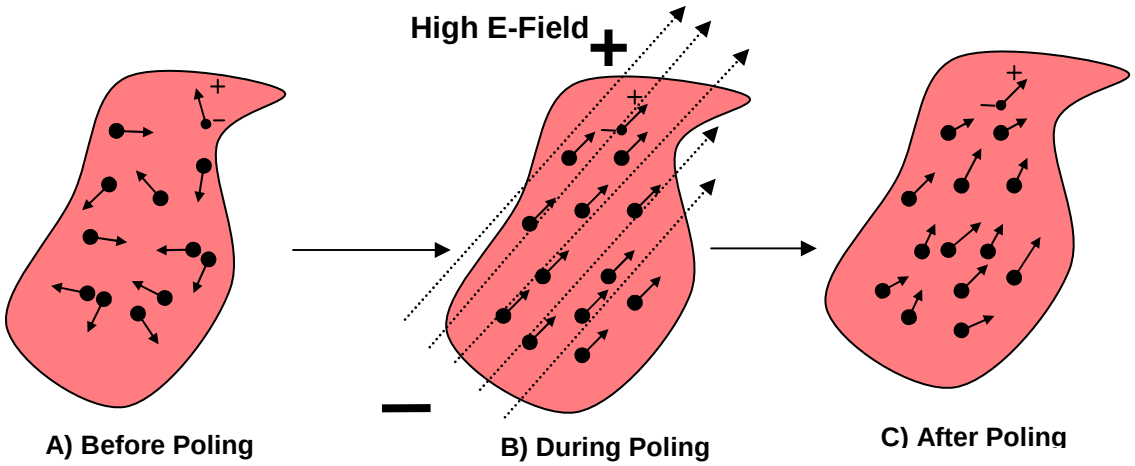

Figure 2-7. Electronic arrangement of dipole moments before poling (a), while being poled with and electric field (b), and arranged in one single direction after poling (c).

2.3.1 Constitutive Equations

The dimensions of piezoelectric ceramics change if a voltage stresses the ceramic electrically. Conversely, when a force stresses it mechanically, it generates an electric charge. If the electrode of the two polarities is not short-circuited, a voltage associated with the charge appears [78]. Thus, the effect of piezoelectricity is a combination of electrical behavior equations where electric displacement **q** equals the permittivity of the material **K** times the electric field strength **E** and Hooke's law equation for ordinary solids where the stress **σ** equals the elastic stiffness **Y** and the strain tensor **ε**. Three

directly related form of equations have been introduced to couple its behavior and form the constitutive equations of piezoelectric materials. The three forms are: [4, 78, and 79]

d-form:

$$\varepsilon_{ij} = S^{E}_{ijkl} \cdot \sigma_{kl} + d^{\varphi}_{mij} \cdot E_{m} \qquad \text{[Eq. 2.3.1]}$$

$$q_{i} = d^{\varphi}_{ijk} \cdot \sigma_{jk} + K^{a(\sigma)}_{ij} \cdot E_{j} \qquad \text{[Eq. 2.3.2]}$$

g-form:

$$\varepsilon_{ij} = S^{q}_{ijkl} \cdot \sigma_{kl} + g^{\varphi}_{mij} \cdot q_{m} \qquad \text{[Eq. 2.3.3]}$$

$$E_{i} = -g^{\varphi}_{ijk} \cdot \sigma_{jk} + (K^{\varphi(\sigma)})^{-1}_{ij} \cdot q_{j} \qquad \text{[Eq. 2.3.4]}$$

e-form:

$$\sigma_{ij} = Y^{E}_{ijkl} \cdot \varepsilon_{mij} - e^{\varphi}_{mij} \cdot E_{m} \qquad \text{[Eq. 2.3.5]}$$

$$q_{i} = e^{\varphi}_{ijk} \cdot \varepsilon_{jk} + K^{\varphi(\varepsilon)}_{ij} \cdot E_{j} \qquad \text{[Eq. 2.3.6]}$$

Where

ε = strain

S^{E} = elastic compliance at zero electric field [m^2 / N]

σ = stress [N/m^2]

d^{φ} = piezoelectric strain coefficient [m/V or C/N]

E = electric field [V/m]

q = electric displacement or electric charge density [C/m^2]

$K^{\varphi(\sigma)}$ = relative dielectric constant [F/m]

Y^{E} = material's elastic stiffness (short circuit condition) [N/m^2]

g^a = piezoelectric voltage coefficient at zero electric field [m^2/C or V-m/N]

e^a = piezoelectric stress coefficient [C/m^2 or N/ V-m]

In these equations, the superscripts E or a, q, ε, σ, φ(ε) and φ(σ) indicate that the property is defined at zero electrical field, at zero electrical displacement, at zero strain, and at zero stress, constant strain, and constant stress respectively.

In an infinite ideal parallel plate, the voltage generated is equal to the electric field divided by the thickness of the piezoplate [80]. Since the length of the piezoplate is relative larger than the thickness (t << l), the behavior can be modeled as an ideal parallel plate yielding to a direct relation between voltage and stress (Figure 2-8):

$$\frac{V}{t} = -g^{\varphi} \cdot \sigma + (\mathrm{K}^{\varphi(\sigma)})^{-1} \cdot q \qquad \text{[Eq. 2.3.7]}$$

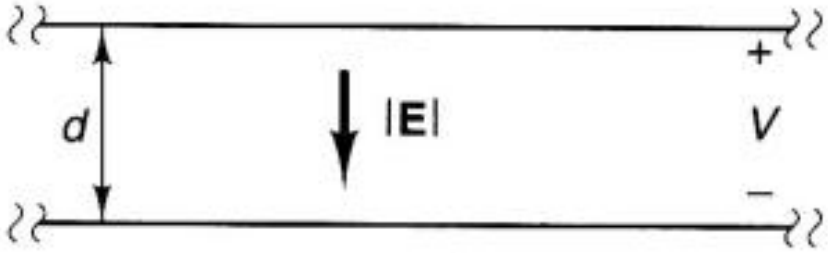

Figure 2-8. Infinite ideal parallel plate. Behavior modeled with the piezoelectric ceramics due to t << l.

2.3.2 The piezoelectric constants

The “d” piezoelectric strain constant is relating the mechanical strain produced by an applied electric field in an unconstrained material.

$$d = \frac{strain\ developed}{applied\ electric\ \ field} \qquad \text{[Eq. 2.3.8]}$$

, yielding the above units of m/V. Conversely, it can be defined as the electrical displacement D caused by the stress σ at zero electrical potential gradient.

$$d = \frac{short\ circuit\ charge\ density}{applied\ mechanical\ stress} \qquad \text{[Eq. 2.3.9].}$$

The units in this case would be expressed in C/N. The “*g*” coefficient is called the voltage coefficient which can be interpreted the electric field E caused by the stress σ at zero electrical displacement *q* (open circuit electric field) [4, 78].

$$g = \frac{open\ circuit\ electric\ \ field}{applied\ mechanical\ stress} \qquad \text{[Eq. 2.3.10]}$$

,yielding the units of V-m/N. Conversely, it can be defined as the ratio of strain ε caused by the electrical displacement q or applied charge density in an unconstrained material yielding to the units of m^2/C

$$g = \frac{strain\ developed}{applied\ charge\ density} \qquad \text{[Eq. 2.3.11]}$$

Finally, the e coefficient is called the stress coefficient because it defines the stress σ caused by the electric field *E* in a fully constrained material yielding units of N/ V-m.

$$e = \frac{strain\ developed}{electric\ \ field} \qquad \text{[Eq. 2.3.12]}$$

Alternatively, it relates the electrical displacement *q* or charge density caused by the applied strain ε at a zero electrical potential gradient yielding units of C/m^2.

$$e = \frac{electric\ charge\ density}{strain\ developed} \qquad \text{[Eq. 2.3.13]}$$

The use of "e constants" is replaced very often by "d constants" since it has a direct relationship through its material's elastic stiffness Y^E.

$$e = Y^E \qquad \text{[Eq. 2.3.14]}$$

,while the relationship between g and d constants can be derived yielding [7]:

$$d = g \cdot K_r \cdot K_0 \qquad \text{[Eq. 2.3.15]}$$

Where

K_r = relative permittivity or dielectric constant (ratio of the amount of stored electrical energy when a potential is applied, relative to the permittivity of free space)

K_0 = permittivity of free space = 8.85×10^{-12} [F/m]

Coupling Coefficients

It is also important to define the coupling coefficients. Coupling coefficient k determines the conversion of mechanical energy to electrical energy of vice versa in piezoelectric materials. It is defined as the square of the coupling coefficient.

$$k = \sqrt{\frac{\text{mechanical energy stored}}{\text{electrical energy applied}}}$$ [Eq. 2.3.16]

or

$$k = \sqrt{\frac{\text{electrical energy stored}}{\text{mechanical energy applied}}}$$ [Eq. 2.3.17]

Numerical Subscripts and Superscripts

The orientation in direction of piezoelectric elements is defined in three axes classified with the numbers 1, 2, and 3 respectively analogous to x, y, and z dimensional set of axes. Two subscripts denote the properties of each piezoelectric material. The first subscript denotes the poling (or applied field) direction. Usually the poling axis is taken as the axis 3. Thus, the first subscripts could be arranged in only three numbers: 1,2, and 3 depending on the polarization direction. The second subscript denotes the direction of the applied stress or induced strain. Subscripts 1, 2, and 3 denote the different parallel direction of each axis while numbers 4,5,6 represent the shear values about these axes respectively (Figure 2-9).

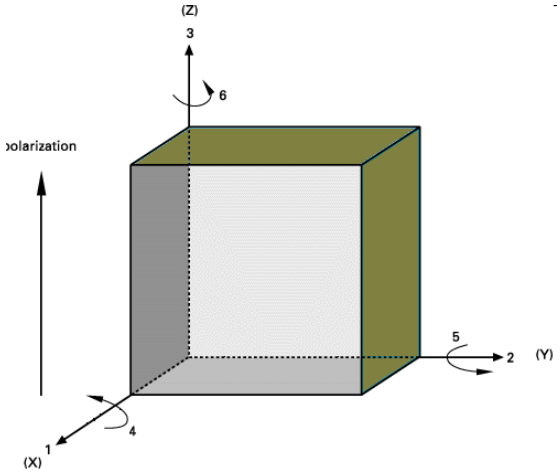

Figure 2-9. Numerical subscripts and orientation in the xyz plane for piezoelectric constants.

As an example, Figure 2-10 shows the same piezoelectric material with two different subscripts used due to variation on the force direction. In figure 2-10a the coefficient subscript used should be denoted as $_{33}$ because polarization is given in the z axis (first subscripts equals $_{3}$) and force is applied in the z axis while Figure 2-10b should use the subscripts $_{32}$.

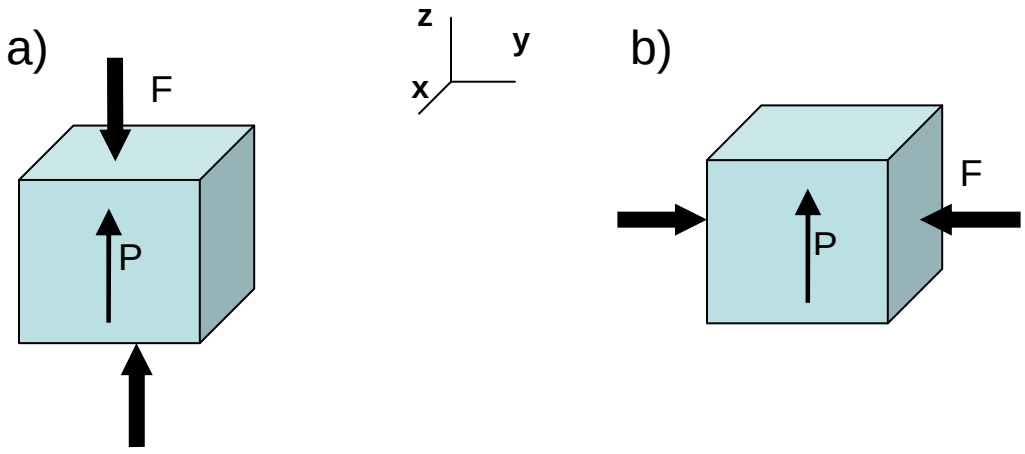

Figure 2-10. Different examples of piezoelectric coefficient notations. a) shows how the force is applied parallel to the z-direction similar to the polarized direction (d_{33}, $g_{33,}$ or e_{33}), while b) shows the force in the y-direction and polarization in the z-direction (d_{32}, $g_{32,}$ or e_{33}).

In addition, some piezoelectric constants may also contain a “superscript” such as the dielectric constant ($\epsilon^{a(\varepsilon)}$) which specifies either the mechanical or electrical condition of the constitutive equations[78]. As an example, the dielectric constant K can be denoted as K^{σ}_{3}, meaning that it is measured in the polar direction ($_3$) with no mechanical clamped. Usually the variables used to defines these subscripts are the following [78]:

T = constant stress = mechanically free

E = constant field = short circuit

D = constant electrical displacement = open circuit

S = constant strain = mechanically clamped

2.4 Finite Element Modeling

2.4.1 Introduction

Partial differential equations (PDEs) can be used to solve many phenomena related in many engineering fields. However, solving these complex equations analytically will be almost impossible due to the arbitrary shapes of the objects and complexity of the equations. The finite element method (FEM) aids engineers to solve these equations by computing these complex equations using computer simulation. Finite element analysis (FEA) commercial software use numerical techniques to model and analyze complex structures by solving boundary value problems. This numerical approach method is used to approximate the solution of PDEs by breaking a continuum solid into discrete couple components that approximate into an overall solution. This method has been evolved in the past decades and it is currently used in many engineering fields. At the beginning this method was originally done with personally written computer programs to carry out the analysis needed. However, currently there exist several commercially available computer programs that eliminate the need to write your own programs such as ANSYS, Abaqus, Nastran, etc. In this project, the use of Abaqus 6.8.2 (Simulia, Providence, RI) was used to analyze the different structures. The finite element method is been used to solve engineering problems such as stress analysis, heat transfer, fluid flow and electromagnetics by computer simulation among others [81].

The finite element method consists on breaking the arbitrary geometrical body into *finite elements* called elements, connected by *nodes*. These elements are represented by linear combinations of polynomial functions with undetermined coefficients. The nodes will represent the undetermined coefficients and will approximate the solution by using the polynomial functions and prescribed boundary conditions. The number of elements and nodes will vary according to its complexity, geometric form, accuracy, etc. The basic of the finite element analysis is to break up the region of interest into small sub regions, the elements. This geometrical body could be either 2D, or 3D. Usually with a 2D region, triangular or rectangular (the most common) elements are used. In some cases,

triangular or rectangular elements with curves sides are also employed. In 3-D geometries they may be pyramids or brick elements [82]. These groups of elements with the connected nodes are called mesh and the process of making the selection is called *mesh generation*.

To obtain a fairly accurate solution small elements are needed, breaking the continuum object in very small discrete objects. Thousands of nodes are required which created thousands more matrices to solve and approximate a valid solution. Thus, computers are use to solve these matrices of equations and determine the approximate solution. The smaller the elements are the most accurate the solution will be. However, computational time will increase with the number of elements and/or nodes selected. Though, larger number of elements will increase the numbers of equations making the solution more accurate. Equilibrium between the number of elements and the computer efficiency should be studied and a decision should be made to successfully model a solution

.

2.4.2 Element Characterization

The geometrical body is broken into elements which are characterized by:

- Element Family
- Degrees of Freedom
- Number of nodes
- Formulation and
- Integration

Element Families

When creating a model, one of the first things to consider is which type of element you will be using. Five element families are commonly used: continuum, shell,

beam, truss, and rigid elements. Figure 2-11 shows the most common element families used in a stress analysis. As by looking at the figure, one of the major distinctions between the element families is the geometry type of each family. Two types of elements were used during this investigation: continuum 2D plane strain elements and rigid bodies. Thus brief explanation on these two kinds of elements will be shown.

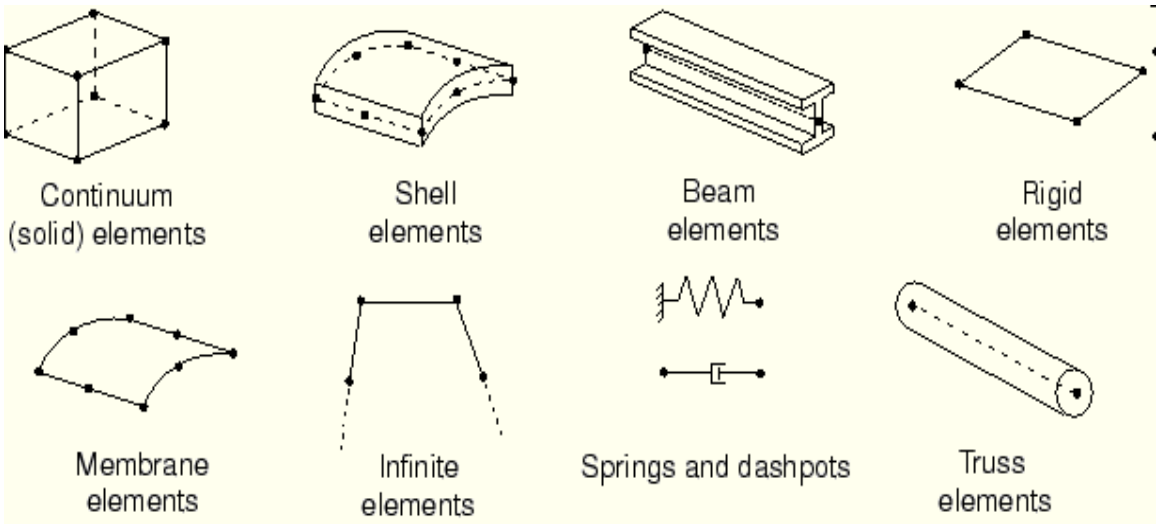

Figure 2-11. Common element families used in mechanical stress analysis [4].

"Reprinted from [4] with permission from Abaqus online documentation"

Continuum (solid) elements

Continuum elements are the most used elements to model a widest variety of structures. These elements model small blocks of material making its configuration easier. These elements can model bricks, mosaic or tiles generating any shape subjected to nearly any loading. Three-dimensional (3D) continuum elements and two – dimensional (2D) continuum elements could be used to evaluate different geometries. 3D continuum elements can be hexahedra (bricks), wedges or tetrahedral. 2D continuum elements can be quadrilateral or triangular. In the case of 2D elements (used for this

project), most commercial software differentiates between their classes by their out-of-plane behavior. According to their out-of-plane behavior, three main classes are used with 2D continuum elements: axisymmetric, plane strain, and plane stress. Axisymmetric elements can model 360-degree rings and are suitable for modeling structures with axisymmetric geometry subject to axisymmetric loading. Plane stress elements assume that the out-of-plane stress σ_{33} is relatively very small with a value close to zero. These elements are suitable to model thin structures. In the case of plane strain elements, it is assumed that the out-of-plane strain ε_{33} is small (close to zero) and thus suitable for structures with large thicknesses. In either of the cases, a value of thickness/plane has to be input for the matrix calculations and polynomial functions to be solved. The use of plane-strain 2D elements was chosen due to the thickness of the structures. No need for 3D-elements was needed because relatively very small strain deformations ($\varepsilon_{33} \approx 0$) were found when loading in the y-direction was applied. Repetition of the same face would not vary the results while structures analyzed were indeed 2-dimensional face structure.

Rigid Elements

Rigid bodies are the collection of nodes and elements whose motion is governed by the motion of a single node, known as *the rigid body reference node*. The shape of a rigid body can be defined as an analytical surface, obtained by revolving or extruding a 2-dimensional geometric profile or as discrete rigid body obtained by meshing the body with nodes and elements. Rigid bodies are useful to model parts in the model that present very high stiffnesses compare to other parts during simulation. A rigid body can undergo large rigid body motion while maintaining a constant shape. Motion of the rigid bodies can be prescribed by applying boundary conditions at the rigid body reference node. Rigid bodies interact with the rest of the models through nodal connection to deformable elements and through contact with deformable elements.

The principal advantage on using these elements instead of full deformable finite elements is computational efficiency since no element-level calculations are performed

for rigid elements. As mentioned before, the motion of rigid bodies are controlled by the motion of a single node. These node contains both translational and rotational degrees of freedom. During this investigation, rigid elements (or rigid bodies) were used to model the top and bottom platens that interact with every structure to be modeled.

Degrees of Freedom

The fundamental variables calculated during the analysis are called *degrees of freedom*. For example, in a stress/displacement simulation the degrees of freedom are the translations at each node. Other families, such as the beam and shell elements will contain translation and rotational degrees of freedom as well. Other analysis will have different degrees of freedom. As an example, an electrical or a heat transfer simulation will have electrical potential or temperature degrees of freedom respectively. In Abaqus, the degrees of freedom have numbering conversion:

1 Translation in direction 1

2 Translation in direction 2

3 Translation in direction 3

4 Rotation about the 1-axis

5 Rotation about the 2-axis

6 Rotation about the 3-axis

7 Warping in open-section beam elements

8 Acoustic pressure, pore pressure, or hydrostatic fluid pressure

9 Electric potential

11 Temperature (or normalized concentration in mass diffusion analysis) for continuum elements or temperature at the first point through the thickness of beams and shells

12+ Temperature at other points through the thickness of beams and shells.

Directions 1, 2, and 3 correspond to the global x, y, and z directions, respectively, unless a local coordinate system has been defined at the nodes [83].

Interpolation

The degrees of freedom (such as displacements, electric potentials, rotations, and other) in the families are calculated only at the nodes of the elements. Interpolation from the nodal displacement is used to calculate the degrees of freedom at any point in the element. The interpolation methods are chosen by the number of nodes is in the elements. For example, elements that have nodes only at the corners (Figure 2-12a) use linear interpolation in each direction. These elements are often called linear elements. Elements containing nodes at the corner and at the middle regions (Figure 2-12b), are called quadratic elements or second order elements. These kinds of elements use quadratic interpolation. Other type of elements that contain modified triangular or tetrahedral elements with midside nodes (Figure 2-12c) use a modified second-order interpolation and are called modified elements or modified second-order elements.

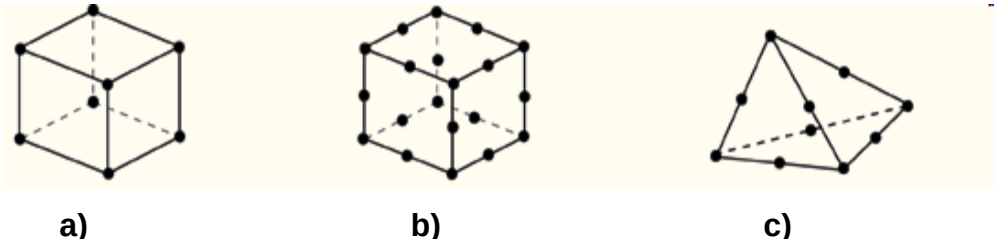

Figure 2-12. Elements with different number of nodes. Elements with nodes at the corner (a) use linear interpolation in each direction. Quadratic elements (b) with elements at the corner and mid section use quadratic interpolation. Modified second order interpolation are used in elements with triangular or tetrahedral [4]

"Reprinted from [4] with permission from Abaqus online documentation"

Formulation

Formulation describes the mathematical theory that defines the elements behavior. *Lagrangian* or *material* description is associated with elements to define its element behavior in all of the stress/displacement elements. As a consequence, the materials associated with the element remains associated throughout the analysis and thus the material description will not be able to flow across the element boundaries. On the other hand, *Eularian* or *spatial* description is used when elements are fixed in space and the material flow through the elements. Fluid mechanics simulations are very common when Eularian or spatial description is used.

Integration

Numerical techniques are use to integrate various quantities over the volume or area of each element. The most common technique used in Abaqus is *Gaussian quadrature,* which evaluates the material response at each integration point in each element. In Abaqus two kind of integration are possible: full integration and reduced integration. Full integration refers to the number of Gauss points required to integrate the polynomial terms in an element's stiffness matrix. These elements commonly have a regular shape edge, are straight and meet at right angles in case of hexahedral and quadrilateral elements. For example in hexahedral and quadrilateral elements, fully integrated, linear elements use two integration points in each direction while reduced integration elements used a single integration point located at the element's centroid.

a) Full Integration

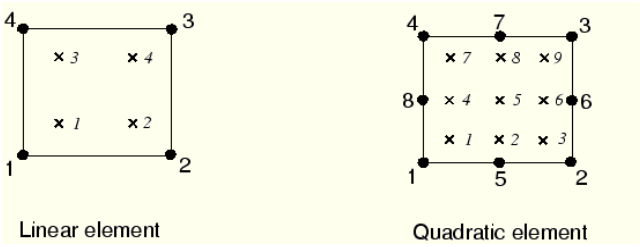

b) Reduced Integration

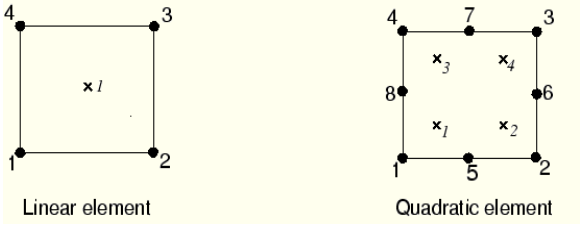

Figure 2-13. Integration procedure in linear and quadratic elements. Full integration (a) and reduced integration [4].

"Reprinted from [4] with permission from Abaqus online documentation"

2-5 Previous Work

Previous mechanical and electro-mechanical characterization [7] of hexagonal honeycomb structures with inverted segments similar to structures manufactured in this investigation were characterized. Important mechanical and electrical data was considered to improve the testing protocol and manufacturing more accurately the following structures. Limitations such as the number of specimens, the manufacturing process, and the electrical testing protocol were found during previous investigations. During this investigation, the limitations were avoided while additional finite element analysis was implemented during this second stage of the investigation. There was an increase in the number of mechanical structures (n=3) and electromechanical structures (with piezoelectric ceramics, n=5) created in three different sizes (L, XL, and XXL) increasing statistical significance.

2.5.1 Previous mechanical analysis

A total of five one-dimensional porous bowtie structures were manufactured via Electronic-Based Robotic Deposition (EBRD) process. Smaller structures (small, medium) were manufactured using the EBRD process. L, XL, and XXL structures were manufactured by hand, using the same protocol specified in this thesis (Chapter 3). Measurements of mechanical behavior such as the relative Young's modulus, plastic collapse, yield stress, yield strain, and resilience was permitted during a quasi-static test where specimens were slowly compressed at a rate of 1 inch/min to failure. Cyclic compression tests at a rate of 0.04mm/sec showed results of the structures at small strain and apparent Poisson's ratio, or compressive strain ratio (CSR). CSR values were calculated at four different strain values: 0.5%, 0.6%, 0.75% and 1.0% using a non-contacting method for measuring transverse deformation using MTI fiber optic probes (MTI Instruments, Albany, NY). Quadratic polynomial and power function fitting were compared to the experimental non-linear stress strain curves described as a function of the relative density. Table 2-1 shows the results from previous study with the standard

mean values in parenthesis for small and large specimens. The results of smaller structures (S and M) showed a very brittle behavior due to the presence of micro-pores probably caused by air bubble trapped during it manufacturing. Thus the plastic collapse was not calculated for these structures. For the larger specimens, the difference in modulus and plastic deformation explained to be linked to the relative densities or aspect ratio of the unit cells. It was also shown that due to the aspect ratio, the specimens can be tailored by increasing or decreasing the /thickness to get an expected mechanical behavior. Non-linear behavior was found for L and XXL structure.

Specimen Type	**S**	**M**	**L**	**XL**	**XXL**
# of specimens	7	5	3	3	3
Elastic Modulus (MPa)			9.70 (1.15)	0.63(0.06)	6.70 (0.26)
Maximum Stress (MPa)	14.7 (2.42)	1.2 (0.97)	0.54 (0.03)	0.08 (0.01)	0.05 (0.04)
Yield Strength(MPa)	-	-	0.40 (0.04)	005 (0.01)	0.35 (0.01)
Yield Strain	-	-	0.06 (0.01)	0.08 (0.01)	0.07 (0.01)
Maximum Stress (MPa)	14.7 (2.42)	1.2 (0.97)	0.54 (0.03)	0.08 (0.01)	0.05 (0.04)
Relative Density	0.551	0.274	0.06	0.03	0.06

Table 2-1. Previous mechanical results found in previous work done by Jaumard [7].

More testing are needed to provide statistical significant to the equations derived from actual data. Results were not verified with FEA and non-linear behavior was only found on certain structures when small strains were applied.

2.5.2 Previous electro-mechanical analysis

Previous investigations hypothesized that the metallic re-entrant bowtie structure will present similar mechanical characteristics as the structure with no piezoelectric material embedded on it with additional electrical stimulus. It was also thought that electric current were generated when the structures are subjected to mechanical stress when the connection was completed or closed in a circuit. By using piezoelectric theory, it was hypothesized and verified how theoretical currents can match experimental currents. Three piezoelectric structures with different relative densities were manufactured and subjected to cyclic compression at different levels of strain. An indirect measured was calculated by placing a 1MΩ resistor in series with the output of the charge generated by the piezoelectric structure. Five different test with different strain levels were performed in 11 cycles (0.5%, 0.6%, 0.75%, 1.0% and 1.5%) at a frequency of 1Hz with a triangular wave. Data was collected at 100Hz. The theoretical electrical current was measured by the change of force relates to change of charge generated. The change of force over time dF/dt was approximated as the change in force over the change in time: $\Delta F/\Delta t$. Theoretical current was defined as the change in charges over time $\Delta Q/\Delta t$ being equal to $d_{33} * dF/dt$. Ohm's law (Eq. 2.5.1) and the voltage drop in the resistor in series calculated the experimental electrical current. Ohm's law states that the current throw a conductor (in this case 1 MΩ resistor) between two points is directly proportional to the voltage and inversely proportional to the resistance of the material (Eq. 2.5.1).

$$I = \frac{V}{R} \qquad \text{[Eq. 2.5.1]}$$

The change in voltage was measured using the MTS machine. Results answered some hypothesis and they also brought some mismatches. Theoretical current compared to experimental current have a mismatch in its calculations. The author explained that the problem could be due to the manufacturing of the structures, the use in inadequate materials to conduct electrical charges from the piezoceramics to the metallic structure, or the application of the bonding material (conductive epoxy). Some results showed that by increasing the strain ratio, more mechanical energy needed to be transferred into

electrical energy and thus generate more current. Results inclined to this hypothesis but there were some results that mismatched, probably for same reasons explained. Structures featuring the highest and lowest relative density also yielded the highest and lowest current ratio. However, there was a mismatch with experimental and theoretical value. Relative density values implied that less mechanical energy was used to deform the structure but instead, it was used to transfer this energy to electrical energy and show it as current varying with time.

Data found in this investigation dealt with electrical alternated signals, which has a different behavior than those direct electrical methods, found in previous investigations [15, 16, 56, 57, 84, and 85] and thus can't be directly compared. In addition, the electrical current values recorded experimentally and theoretically varied in the nano amperes (nA) , which could yield to unsuccessful measurement with the equipment used and the resolution at very small voltages. Small voltages, would indeed lead to small currents. Alternated signals need to be rectified to directly compare them to previous reported documents. During this investigation, rectification of the signal and piezoceramics with higher coefficients were used to provide measurable signals above data acquisition limits.

Overview for Chapters 3-5

The following investigation focused on the characterization of electro-mechanical cellular solids that can be tailored to use as novel implants to enhance bone osteogenesis. It is hypothesized that these feasible new implants will provide similar electrical signals enhancing the mechano-transduction process of bone healing while withstanding the mechanical loading where its implanted (in this case the loading of spine). Chapter 3 presents in extend the methodology used to manufacture, simulate, and evaluate the different structures tested. It also presents the testing protocols used for each part in this study. Chapter 4 and Chapter 5 present the studies of the electro-mechanical evaluation divided into research paper formats for presentation. These two chapters include their own reference and reference numbers. Chapter 4 presents the mechanical characterization of a novel cellular metallic solid. In this chapter, it was hypothesized that by changing the dimensions/aspect ratio or relative density of potential cellular solid structures, the mechanical characteristics will change drastically and thus they can be tailored to mimic the characteristics of the replaced tissue. It will introduce the reader the main characteristics towards the end goal of this investigation, which encompasses the electro-mechanical evaluation of these cellular solids. Chapter 5 characterized and evaluated the feasibility to reproduce electrical signals due to the piezoelectric ceramics embedded in the structures and compared its results with existing electrical stimulators that have found to enhance bone osteogenesis. The feasibility of producing electrical signals and withstanding mechanical loading is discussed in this chapter.

Chapter 3: Methodology

During this investigation, two types of metallic cellular solids prototypes were manufactured: mechanical structures (no piezo-plates) and electro-mechanical structures (with piezoelectric ceramics embedded into them). In the first type of structures, mechanical behavior such as apparent stress and strain, apparent relative Young modulus and its relation with its relative densities were evaluated in three different dimensions. In addition, the transverse deformation was evaluated to verify its negative compressive strain ratio (CSR) as expected for re-entrant structures. The other electromechanical structures were manufactured to evaluate the electro-mechanical properties such as electrical voltages and electrical currents. The manufacturing process for mechanical and electro-mechanical structures was similar since structures presented similar dimensions with differences such as cellular matrix repetition and the presence of piezoelectric ceramics in the case of electro-mechanical structures. After data was collected and analyzed, it was compared to computational models in FEA analysis.

3.1 Experimental

3.1.2 Preparation of specimens

Bowtie-like specific hexagonal metallic cellular solid prototypes with inverted cells were manufactured. Three mechanical structures (L, XL, and XXL) with different dimensions and relative densities were manufactured. Three structures with the same dimension of each type were created (n=3). Two additional types of electromechanical structures (pXL and pXXL) with same dimensions as the mechanical structures but with less cell repetitions were also manufactured (n=5 for each type). Figure 3-1 is a representation of all the mechanical and electromechanical structures manufactured. Electromechanical structures had embedded one-millimeter thick lead zirconate titanate piezo ceramics type 5A (PZT-5A). PZT-5A was chosen due to its availability, cost

efficiency, and high piezoelectric coefficient. Since L and XXL structures posed very similar relative densities and thus similar mechanical behavior (as shown in previous investigation), they were not characterized electro-mechanically. It was hypothesized that due to similar mechanical behavior, a similar electrical response between pL and pXXL structures would be recorded.

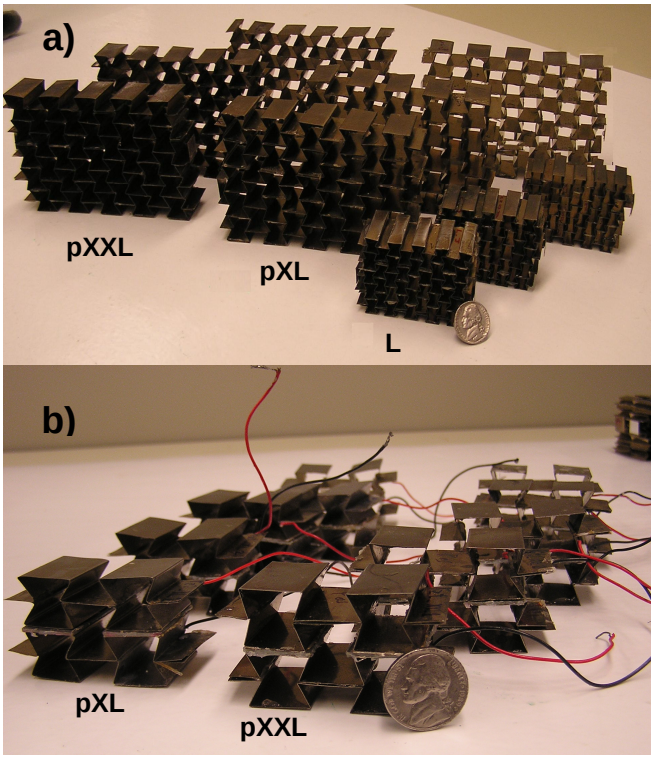

Figure 3-1. Representation of all manufactured structures: mechanical structure (a) and electromechanical structures (b)

Mechanical properties for the materials were known such as modulus of elasticity for SS-302 (200 GPa) and PZT-5A (52GPa), Poisson ratio (0.3 for steel and 0.25 for PZT) and density (7860 kg/m^3 for steel and 7800 kg/m^3 for PZT). Also electric properties such as the electrical conductivity for stainless steel was 1.39E6 (S·m^{-1},where "S" stands for Siemens or the inverse of electrical resistivity in ohms). PZT-5A was classified as a non-conductive media with a resistivity of 1E6 (Ω-m) while the piezoelectric g_{33} constant

of PZT-5A was 2.40E-02 (m/V) [86, 87]. Table 3-1 and Figure 3-2 show the geometry and dimension of the structures manufactured. A 10x5 cell matrix was created for mechanical bowtie structures while 2x2 cell matrices for the electromechanical structures.

Specimen Type	L	XL	XXL	pXL	pXXL
Number of Structures (n)	3	3	3	5	5
Width (mm)	7.5	16.5	16.5	16.5	16.5
Length (mm)	4	8	8	8	8
Thickness (mm)	0.102	0.102	0.204	0.102	0.204
Angle (degrees)	60	60	60	60	60
Depth (mm)	25.4	25.4	25.4	25.4	25.4
PZT thickness (mm)	-	-	-	1.02	1.02
PZT length (mm)	-	-	-	16.5	16.5

Table 3-1. Dimensions of the mechanical and electro-mechanical cellular solid structures.

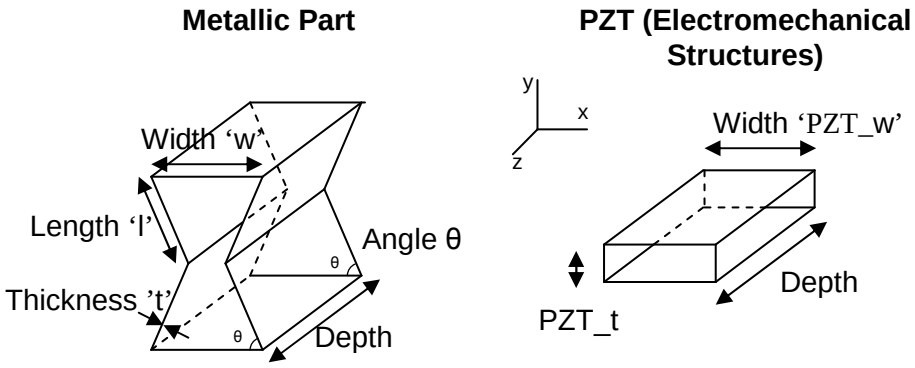

Figure 3-2. Geometric dimensions for metallic cellular solids structures (left) with additional dimension for the piezoelectric ceramics in the electromechanical structures (right)

Stainless steel 302 series shim rolls (Precision Brand, Downer Grove, IL) were purchased and cut into strips (1 inch in depth) using a precise shear machine. The length of the strips depended on the cell repetitions and dimensions of the specimens. After strips were cut (10 for each mechanical structure and 4 for each electro-mechanical structure), they were placed into a conventional oven at 650-700 degrees Fahrenheit for

two hours to anneal and relief residual stresses caused by cutting the strips [88]. The strips were allowed to cool down for a day at room temperature. Once strips were stress-relieved, they were bent to 90 degrees with a bending braking machine (MicroMark, Berkeley Heights, NJ). A perfect square tool was attached to the bending braking machine improved the bending of the strips from previous methodology for better alignment. Following 90-degree bending, they were manually bent to 60 degrees with aluminum templates. At this point, strips were subjected to a second stress relief annealing process while attaching the strips uniformly with bulldog clips and metallic templates to maintain an adequate position. After the second annealing process, the surfaces were sandpapered with 220-A grit paper and finally cleaned with acetone for assembling. Strips were glued and assembled together using two part curing epoxy. Bulldog clips and wood templates were used to attach each strip. After assembling, the structures were left overnight for the epoxy to cure.

For electro-mechanical structures, similar procedure was utilized to manufacture the metallic cellular part of the structures. Though, the assembling process was quite different since extra piezoceramics were included into the middle section of the structures. After the metallic strips were manufactured and top or bottom sections were assembled, piezoelectric ceramics were prepared and embedded together in the middle section of the metallic strips. Piezoelectric ceramics were cut at specific dimensions with a precision diamond low speed saw (Buehler Ltd, Lake Bluff, IL). Once cut, silicone was applied to the edges to avoid circuit shortening and let to dry. Conductive silver epoxy with 65% silver (Stan Rubinstein Assoc., Foxboro, MA) was used to assemble and secure conductivity between metallic strips and piezoelectric plates. Bonding was left to cure for one night. Previous to bonding, external wires were also soldered to the metallic strips using a soldering iron and “all-purpose” flux to act as signal electrodes. Figure 3-3 shows a step-by-step diagram of the procedure.

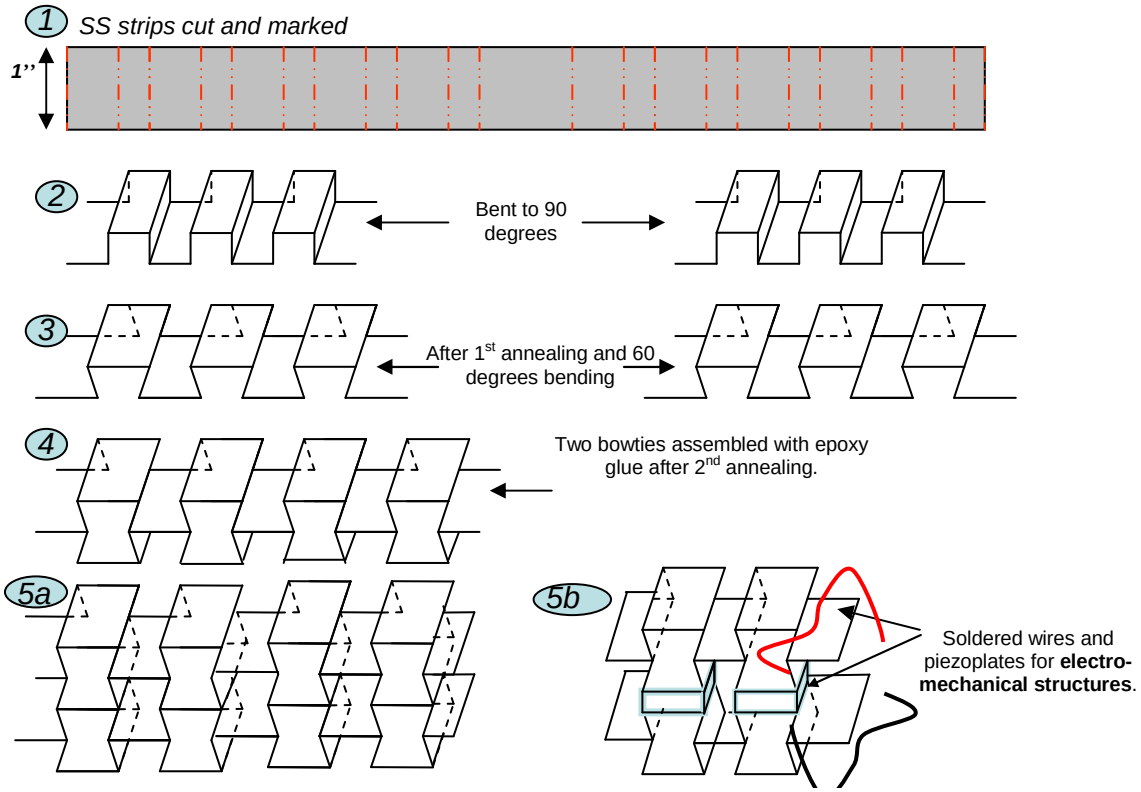

Figure 3-3. Step by step manufacturing representation for mechanical (1-5a) and electromechanical structures (1-5b).

Improvements in manufacturing

A better shearing break machine was used to cut the strips more uniformly. A perfect square device was used to align uniformly to bend them into 90-degree angles. Due to a higher uniformly 90-degree angle, the 60 degree bending let the bends to have sharper angles with small variations in the radii of curvatures. A more efficient epoxy and a better quality conductive epoxy from SRA Rubenstein associates with 65% silver to increase conductivity was used to assemble the strips and piezo-ceramics respectively. Silicone sealant was also applied in the piezoelectric surfaces at the edges to avoid electrical short circuiting. In additional electro-mechanical testing protocols was modified

and piezo-ceramics with higher piezoelectric response was replaced to avoid exceeding testing machine recorded limits.

3.1.2 Testing Protocol

Once the thickness, height, width, and weight were recorded in all the specimens (Appendix A), they were subjected to axial cyclic compression using a servo hydraulic machine (Mini Bionix 858, MTS, Eden Praire, MN). Relative densities were calculated as the density of the material "ρ^*" divided by the apparent density of the cellular solid "ρ_s". Structures were placed in an extended self-alignment platen (bottom) and compressed with a fixed platen (top). Petroleum jelly lubricant was used to decrease the friction between the platens and the structures. Structures were preconditioned cyclically at a compressive force control from 1N to 10N to let the lubricant set between the platens and the structures. After preconditioning, the displacement control was zeroed at a compressive force of 10N. At this point, most of the top surfaces were touching the platens but due to manufacturing limitations, there were some uneven surfaces that were still untouched (Figure 3-4). This is the reason why the zero displacement was started at the highest compressive preconditioning value.

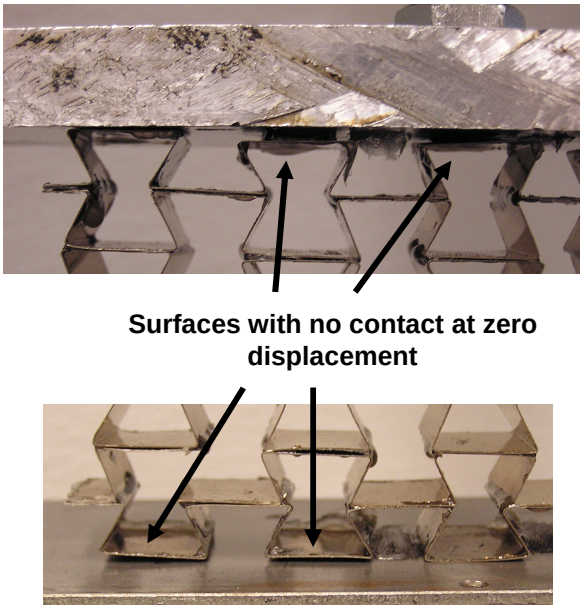

Figure 3-4. Representation of non-contacting surface regions at top and bottom when displacement is zeroed at –10N.

Mechanical Testing Protocol

Mechanical structures were subjected to ten axial compressive ramp cycles from 0 to 0.01 strain and 0 to 0.04 strain at a displacement rate of 0.423 mm/sec (1 inch/min). Five runs were repeated for each structure. During each different run, the structures were removed and replaced between the platens to avoid errors caused by similar repetitions of test set up. Preconditioning was repeated for each run with adequate zero displacement and an initial compressive force of 10 N. Force and axial displacements were collected using a 2.5kN load cell sensor connected to the servo-hydraulic machine (Mini Bionic 858, MTS, Eden Prairie, MN). Reflective targets made out of reflective tape were placed on the transverse edges of the structures to measure the transverse displacement. Transverse displacements were collected using a non-contacting sensor for small displacements (MTI –2100 Photonic Sensor, MTI Instruments Inc, Albany, NY). Due to displacement equipment limitation (±300 μm), transverse displacements were only measured up to 0.01 strain (Figure 3-5).

Data was collected using a data acquisition system (TestStar II, MTS, Eden Prairie, MN) every 100 Hz and developed with Matlab programs (Mathworks Inc, Natick, MA). In previous study [7], yield strain ranges varied for each structure due to different relative densities. It was found that structures with similar densities presented similar linear regions thus similar yield strain values. The range of this yield strains varied from 0.05 to 0.09. Thus, to analyze our structure within the linear region, the structures were subjected to axial mechanical compressive loading up to 0.04 strain values. Mechanical properties such as relative Young's modulus (E^*/E_s, which the same index definition as relative density), and compressive strain ratios (CSR) were calculated. Compressive strain ratios were calculated on the compressive loading up to 0.01 strains. Relative Young modulus was calculated when structures were subjected to 0.04 strain**.** All graphs are listed in Appendix B. Displacements and reaction forces collected from this mechanical testing were compared to finite element analysis discussed later in this chapter.

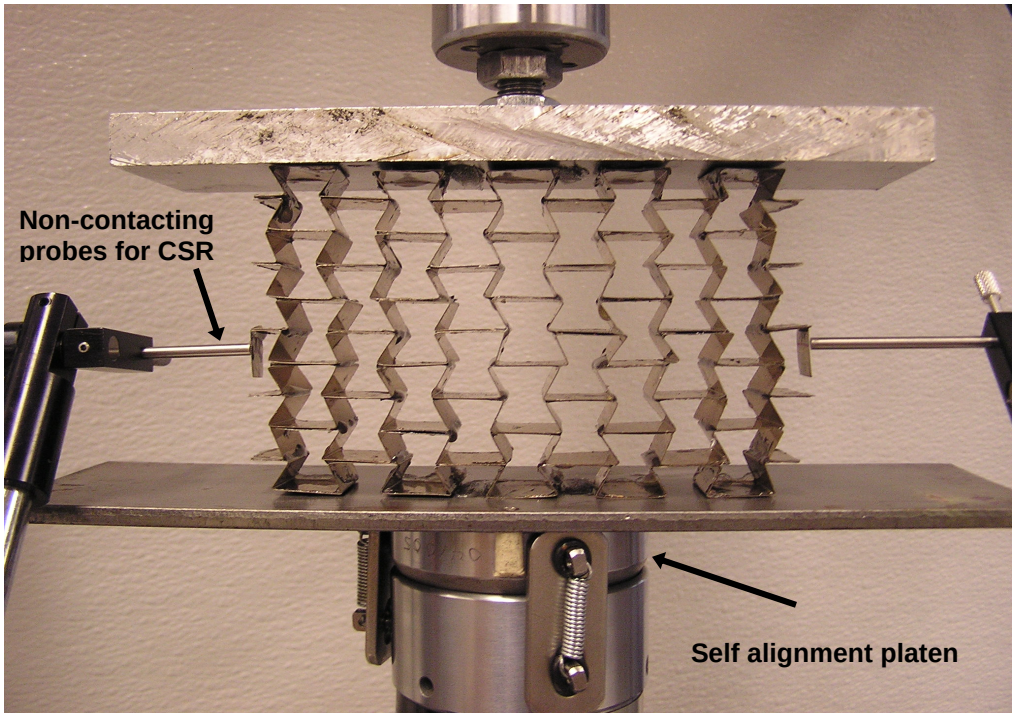

Figure 3-5. Test set up for every structure at small strains (0.01). Similar test set-up was applied for strain up to 0.04 without reflecting the reflecting targets due to MTI limitations.

Electromechanical Testing Protocol

Electromechanical structures (pXL, and pXXL) with embedded piezoelectric materials were placed in similar platens used for mechanical testing protocol and preconditioned as before. However, an additional insulating surface made out of polymethyl methacrylate (Plexiglas®) was added in between the platens and the structures to avoid electrical charge dissipation and/or shortening. Plexiglas® with an adequate thickness was selected rather than stiffer materials such as ceramics because of the brittleness of ceramics during previous unsuccessful tests [7]. The piezoelectric composites were subjected to 10 sinusoidal wave cycles of axial compression at two different frequencies (1 Hz and 2 Hz) up to 0.01 and 0.02 strains. In the case of pXL structures that demonstrated more flexible behavior, an additional test up to 0.04 strain was applied due to unsuccessful recorded electrical data when compressed to lower strain values (0.01 and 0.02 strain). The frequencies selected were comparable to the walking cycle frequencies found in different studies [30, 57, 89]. Three runs were repeated for each structure. During each different run, the structures were placed away and back into the platens to avoid errors cause by similar repetitions of test set up. Axial forces and axial displacements were collected every 100 Hz for mechanical data. Additional electrical data was collected in these structures. Alternated voltages coming directly from the piezoelectric structure were also collected using the TestStar II data acquisition system.

Electronic Rectified Circuitry

In addition to alternated signals, a rectified electronic circuit was designed to convert the alternated voltage into direct voltage. A simple full wave rectifier was created to modify the raw electrical signal and convert alternated voltage (V_{AC}) coming from the electro-mechanical piezoceramics to direct rectified voltage (V_{DC}). Once the rectified voltages are processed, direct electrical currents were calculated using Ohm's law

(Current = Voltage / Resistance) and a known resistor value (475 kΩ). Electrical current were compared to existing methodologies that have proven to enhance bone [11, 12, 22, 24, 58, 59].

The full wave rectifier was made out of a four-diode bridge as shown in Figure 3-6. The IN signal in this diode bridge works in pairs as the alternated voltage flips back and forth to keep the current flowing in the positive cycle.

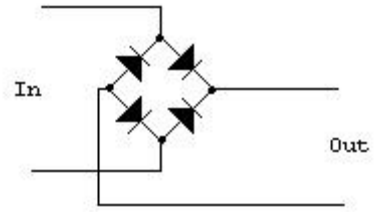

Figure 3-6. Schematic of a four diode bridge use for the rectifier signal [3].

"Reprinted from [3] with permission from author (publisher does not own the rights, see Appendix E)."

During a positive half cycle two diodes connected in series supply current into the voltage. The other two diodes are in reversed mode and thus there is no current flow around them. The next stage, when the signal is ready to transmit negative half cycles, the direction of the other two diodes transmit the electrical signals in the opposite direction. The active diodes during the positive cycle will now be in reversed mode and no flow of opposite direction will be transmitted. The signal as it alternates is shown below in Figure 3-7.

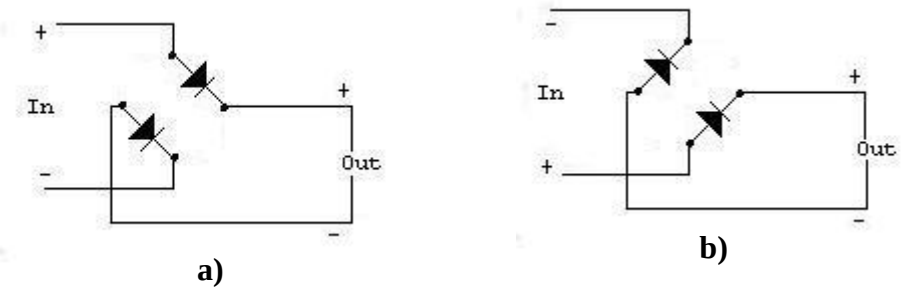

Figure 3-7. Alternated direction and use diodes to provide full positive alternated signals. Diodes work in pairs, transmitting positive forward electric signals (a) and positive reversed electrical signals (b) [3].

The signal output from the piezoelectric structures that generate positive and negative half cycles was rectified into only positive half cycles. It is important to highlight that there will be a forward voltage drop on each diode. Thus, Schottky diodes that posse low forward voltage drops are used for this analysis since they present lower voltage drops. Alternated signal will be converted into full positive sine wave cycles as shown in Figure 3-8.

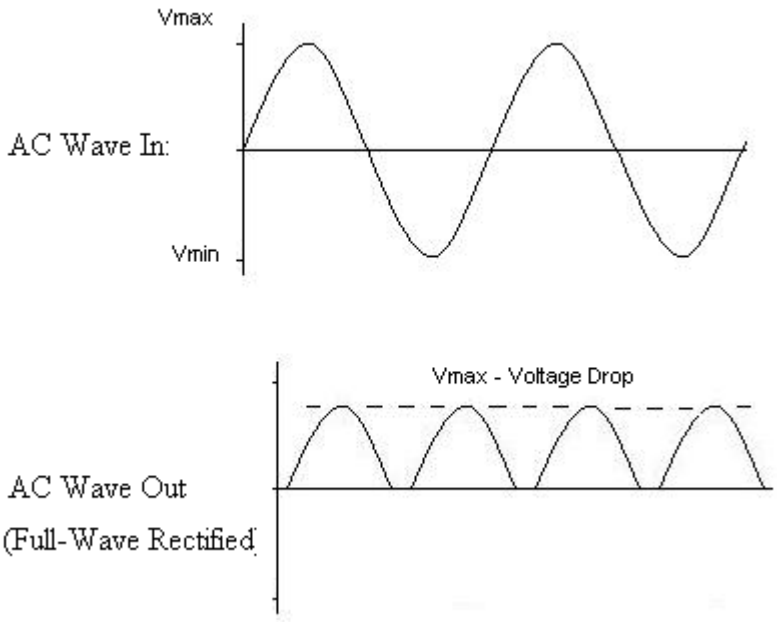

Figure 3-8. Negative and positive alternated cycles were processed into only positive cycles.

After the full wave cycles were converted into only positive cycles by placing a large capacitor in parallel with the output voltages, the electrical voltages were essentially behaving as direct voltages (V_{DC}). The time the capacitor discharges are smaller than for the next sine wave and thus the output voltage ripples and becomes essentially direct voltage (Figure 3-9).

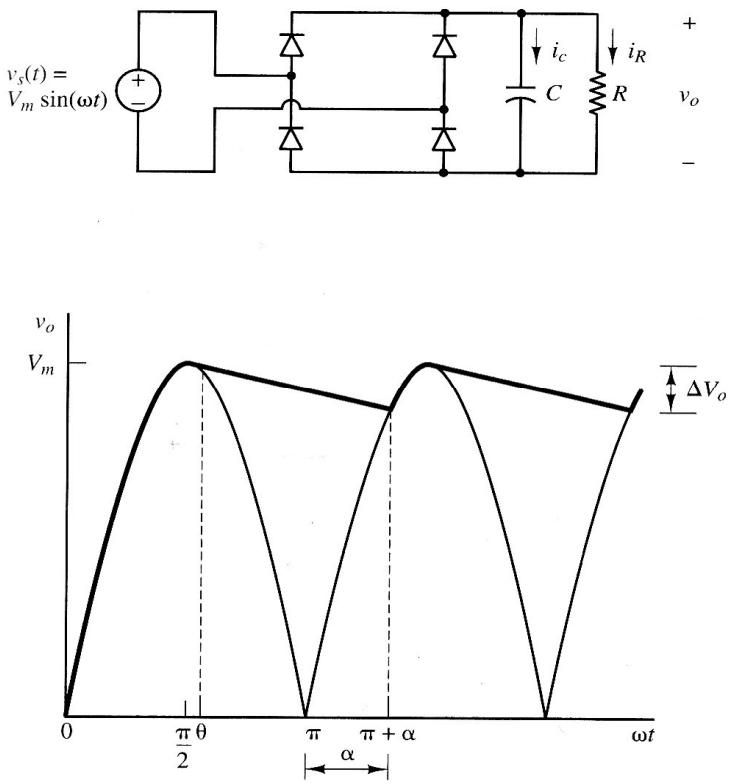

Figure 3-9. Input and output voltages for a full wave rectifier with capacitance filter. Bold line shows the essentially direct electrical voltage V_{DC}) [1].

"Reprinted from [1] with permission from author."

Figure 3-9 also shows the simple electronic circuit used to rectify the signal and collect the electrical current by a known resistor inserted in parallel with the capacitor. .

3.2 Finite Element Analysis

Most complete finite elements analysis (FEA) simulations consist of three distinct stages: preprocessing, simulation, and post processing. Preprocessing consists on defining the physical problem and then creating an input file. During this investigation Abaqus/CAE, a computer aided engineering environment from Simulia, Inc was used to create the structures that resemble the handcrafted structures. First, three mechanical models were created with same mechanical properties, dimensions, and geometries similar to the mechanical manufactured (L, XL, XXL). Secondly, the electromechanical structures (pXL, and pXXL) were modeled. For every model, only mechanical linear behavior was modeled and thus mechanical properties such as modulus of elasticity and Poisson ratios were input. Piezo-electric properties were not modeled with this FEA software because of the inherent program limitations that assume linear electromechanical behavior in simulating piezoelectric response when models are subjected to mechanical stresses; this assumption is only true for very low applied stresses and was not be appropriate in the present application. After many attemps to simulate the applied voltage being generated, it was concluded that Abaqus did not have the capability to transform mechanical energy to electrical energy. It is designed to simulation small deformations when an electrical energy is inputted. A total of five models were created, assembled, analyzed using Abaqus 6.8.2 computer software (Simulia Inc, Providence, RI). In addition, rigid analytical bodies were created to model the platens where the boundary conditions and loads were also applied.

Finite element packages such as Abaqus require the user to go over a number of steps in one form or another to find the solution using the finite element method [90]. An explanation of the steps employed is covered in this section.

3.2.1 Defining the geometry

Since the structures were meant to have only one dimensional reentrant behavior as cellular solids, the structures were modeled with 2D plane strain elements. The geometric dimensions of the models were created using the values shown in Table 3-1. The main purpose of creating these models is to compare and validate optimal manufacturing which was inevitable with the current handcrafted manufactured prototypes. One important difference between the strips manufactured and models simulated are the corners of the cells**.** Due to limitations in handcraft manufacturing and variation between the radii of curvature at each corner, it was difficult to approximate the radius of curvature due to highly variations between each other. Measureable techniques to provide accurate raddi of curvatures were beyond this investigation. Also, optimal manufacturing simulations were needed. The corners were modeled with sharp instead of rounded radius of curvatures with a 60-degree angle as handcrafted structures (Figure 3-10). Rounded corners were also evaluated but sharp corners were chosen to validate accurate manufacturing processes and its results.

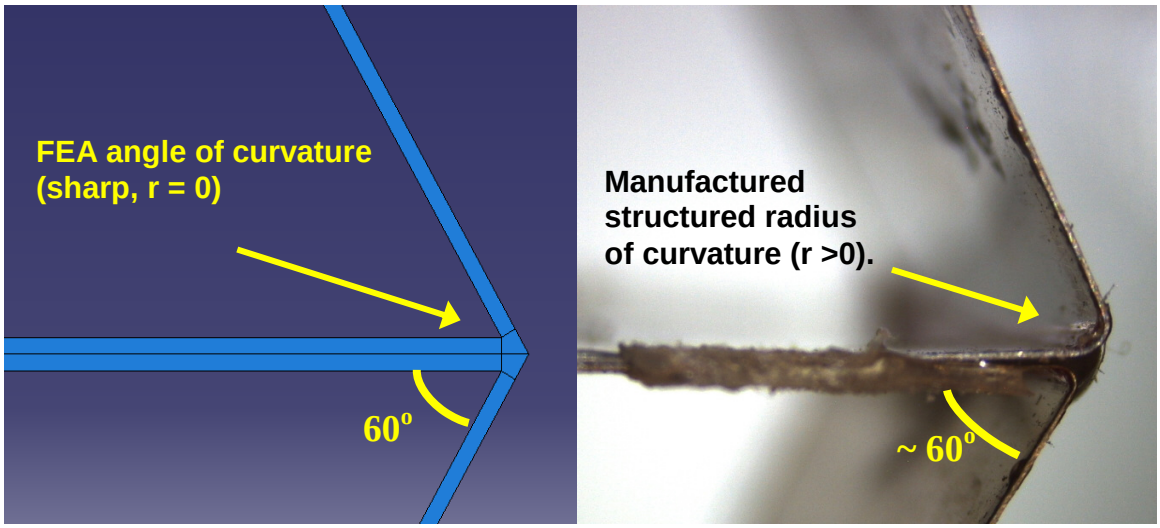

Figure 3-10. Difference in modeling in the radius of curvature for the cell corners. Sharp radius of curvature for FEA model (in left) and manufactured structure (in right).

Two parts were created in the mechanical simulation while three parts were created in the electro-mechanical simulation to assemble the models. For mechanical models, each strip was created as a part. Also rigid analytical parts were created representing the platens at the top and bottom surfaces of the structure. As mentioned in the background section, rigid bodies are ideal to model very stiff materials where stress distribution is not important. Rigid analytical parts also increase computer efficiency. An additional part representing the piezo-electric plate was created for the electro-mechanical structures. Once every part was created using adequate geometries and dimensions, the parts were assembled together to form the desired models. For the mechanical models, metallic strips were assembled with tied contact interactions to form the structural mechanical model. Electro-mechanical models were also assembled in similar way but with additional piezo-electric plates in between the metallic strips models (Figure 3-11).

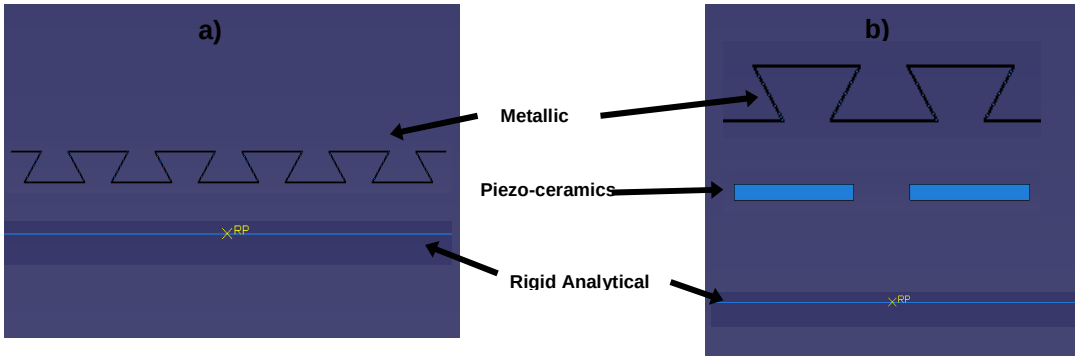

Figure 3-11. Representation of the different parts created for each model: mechanical structures (a) and electro-mechanical structures (b).

Two types of surface contact properties were applied to assemble the models: tied constraint interaction and friction interaction. Tie constrains interactions were used to combine two surfaces together where no motion is present. Since structures were

assumed to glue correctly together with normal epoxy, motionless interactions were expected between each stainless steel strip. On the other hand, frictional behavior defines the force resisting the relative tangential motion of the surface in a mechanical contact analysis. If this contact property is modeled with very low friction at the interface, then it is assumed that the surfaces in contact may slide without much restriction, similar to the physical situation of the contacts between the platens (analytical rigid parts) and the extremes of the cellular metallic solid.

After the models were assembled, final rigid bodies were added to act as boundary extremes in the models. These rigid models resembled the platens where the boundary conditions were applied. During experimental testing, the structures were free to move around the x-axis since only lubrication was applied on top and bottom. Thus a tangential frictionless interaction between the rigid bodies and structure was defined at these surfaces. The final models are presented in Figure 3-12.

a) **b)**

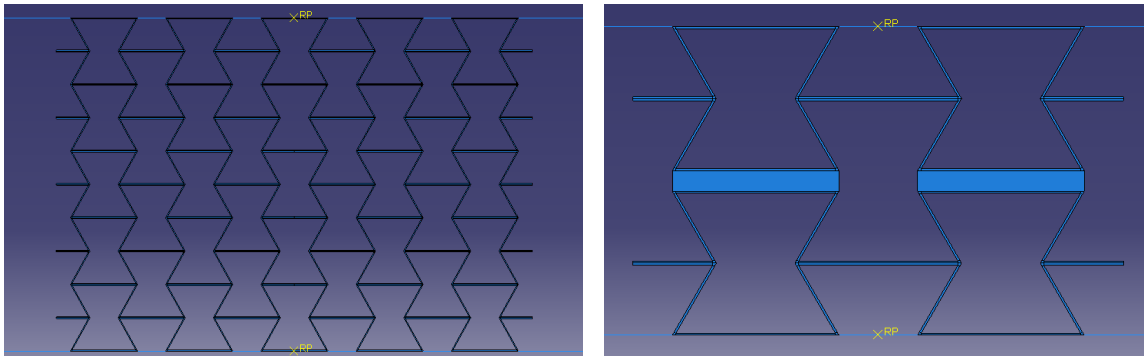

Figure 3-12. Final representation of mechanical (a) and electro-mechanical models (b).

3.2.2 Element type and material properties

Plane-strain 2D quadrilateral elements were chosen due to the thickness of the structures and relatively small out of plane deformation ($\varepsilon_{33} \approx 0$) presented when mechanically loaded during experimentation. Repetition of the two dimensional face to become three dimensional would not vary extensively the results due to unnoticeable out of plane deformations ($\varepsilon_{33} \approx 0$) but will increase computer efficiency. This will avoid unnecessary calculation throughout the thickness and thus make our model more efficient by augmenting the number of elements in a 2D plane, eliminating computer modeling time and increasing computer efficiency.

Mechanical properties such as modulus of elasticity and Poisson ratio were specified since models were mechanically simulated under the linear elastic region. In electro-mechanical models, no piezoelectric simulation was done due to limitation in the software for the intended results. Also, very small deformations were attributed to the piezoelectric ceramics that could be neglected in this model. A relation between axial stress σ and g_{33} coefficient in the piezoelectric structures were compared for its direct relationship as presented in Equation 2.3.7.

3.2.3 Mesh the model

Once the models were created and material properties were defined, the model was discretized into elements that will compose the mesh of the structure. Meshing the models can be done by user input or automatically with computer programs or both. Based on the geometry of the structure and the easiness provided by Abaqus 6.8.2 the mesh was defined using quadrilateral elements and an automatic structured meshing technique. Structured meshing technique generated meshes using simple predefined mesh topologies. Abaqus/CAE transforms the mesh of a regularly shaped region, such as square, triangle, circle onto the geometries of the region wanted to be meshed. Since the

piezo-plates resemble a square topology, no singularities were found. However, while meshing the stainless strip parts, there were singularities on the meshes found at the corners where highly strain values appeared. To overcome this problem, the strips were partitioned into smaller and more regular shapes. Defined rectangular shapes were partitioned along the strips with partitioned regions at each corner. Figure 3-13 shows the different partitions created and the parts already meshed.

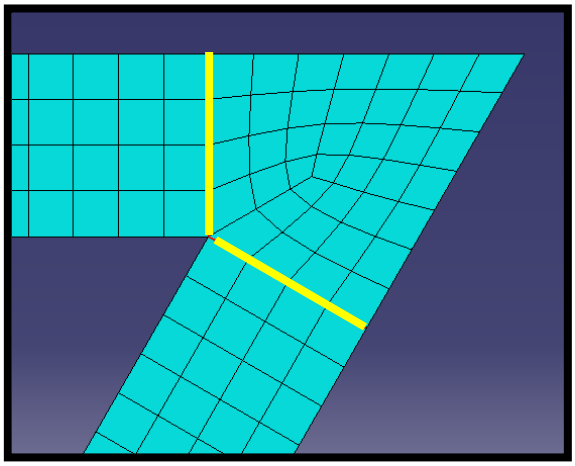

Figure 3-13. Final partitions for metallic strips (in bold). Automatic partitions were used with quadrilateral elements. At the edges, quadrilateral elements were slightly deformed in the metallic strip parts.

3.2.4 Boundary conditions and external loads

Three boundary conditions were specified for every model: one displacement condition and two fixed boundary conditions. Axial compressive displacement was applied to the top analytical rigid body up to 0.04 axial strain. Since interactions with the rest of the model are obtained through nodal connections, the axial displacement will be transferred through the entire model by the nodal tie constraint contact interactions. However, the model needed to be fixed at a certain node in the x and y direction otherwise it will start floating on space. The reference point in the bottom rigid body was fixed in avoiding the models to slide infinitely as it is not connected to the rigid bodies.

Furthermore, a middle symmetric node was chosen to fix the model transversely. Figure 3-14 shows the different models with their different boundary conditions.

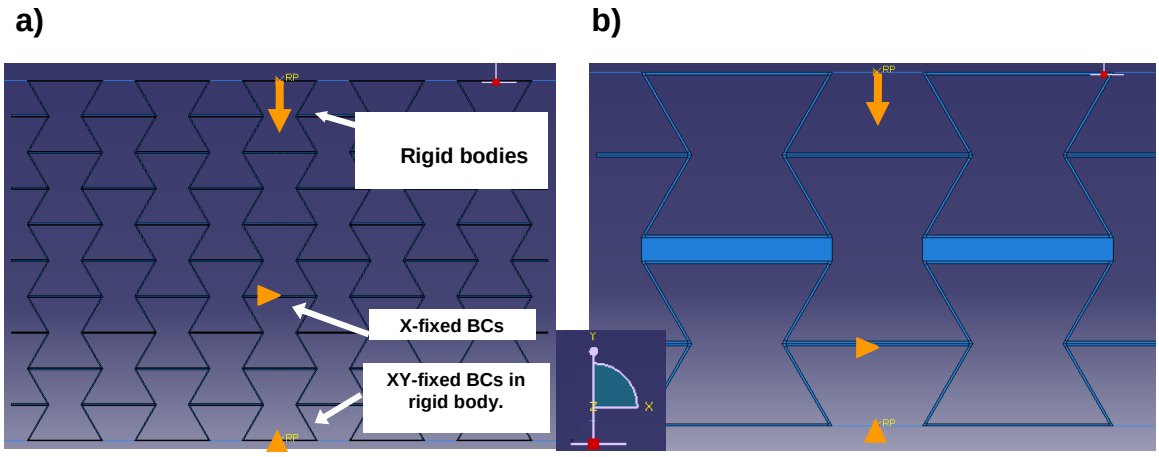

Figure 3-14. Mechanical (a) and electro-mechanical (b) models with their specific boundary conditions.

3.2.5 Steps and field outputs

Within a model you define a sequence of one or more analysis steps. These steps provide a convenient way to capture changes in the loading and boundary conditions in the model. Also, field outputs were requested for the specified needed data. Field outputs are generated data that are spatially distributed over the entire model or over a portion of it. Many field output requests are available in Abaqus such as displacements/ velocity/ acceleration, forces, contact, energy, thermal, electric, volume, fluids, etc. As in this model, the only values specified were mechanical parameters of the models in the linear region such as forces, stresses, strains, and displacements. The increment (in distance) for the solution to converge was given at every 0.001 of the total displacement and data was collected every 0.01 increment.

3.2.6 Generating the solution

Once the structures were assembled and meshed with specific boundary conditions in place, the model was ready for the simulation to start. This simulation is normally run as a background process where computer programs (in this case Abaqus 6.8.2) solve the numerical problem defined in the model. Depending on the complexity of the problem being analyzed and the power of the computer being used, it may take anywhere from seconds to days to complete an analysis run. During the simulation, if the solution finally converged, it took an average time of 30 to 1 hour was for the simulation to terminate.

3.2.7 Post-processing.

Once the simulation is terminated, data is returned as an output field. These output files contain the field output requested in section 3.2.5. At this point, the user is ready to analyze the data and interpret the results. During this step the evaluation and interpretation is generally done interactively using a graphical user interfaces provided by most computer commercial software or other computer programs. In this investigation the Visualization module of Abaqus/CAE and Matlab were used. The Abaqus/CAE Visualization module has a variety of options for displaying the results, including color contour plots, animations, deformed shape plots, and X-Y plots. In this case, it was used to plot models shown in the following chapter. Matlab programs were used to manipulate the data on each increment and plot the desired stress strain curves or the desired compressive strain ratios as deformation increases.

3.2.8 Redefine the mesh

The accuracy of the model increases with the increase of number in elements. The models were redefined with a higher number of elements until a convergence and efficiency of the results are shown. A convergence test was done and the numbers of elements were chosen.

Convergence test

A convergence study was done to provide convergence accuracy in the models by changing the number of mesh elements and/or length. Values for convergence in the XXL model were tested with 3, 4, 6, 9, and 12 quadrilateral elements across the thickness of the structure. The presence of few deformed elements were presented at the corners of the structure (Figure 3-15) but did not presented any limitation due to small deformations. Reaction forces generated on the top analytical rigid body and maximum plane strain across the entire structure were used as convergence criteria.

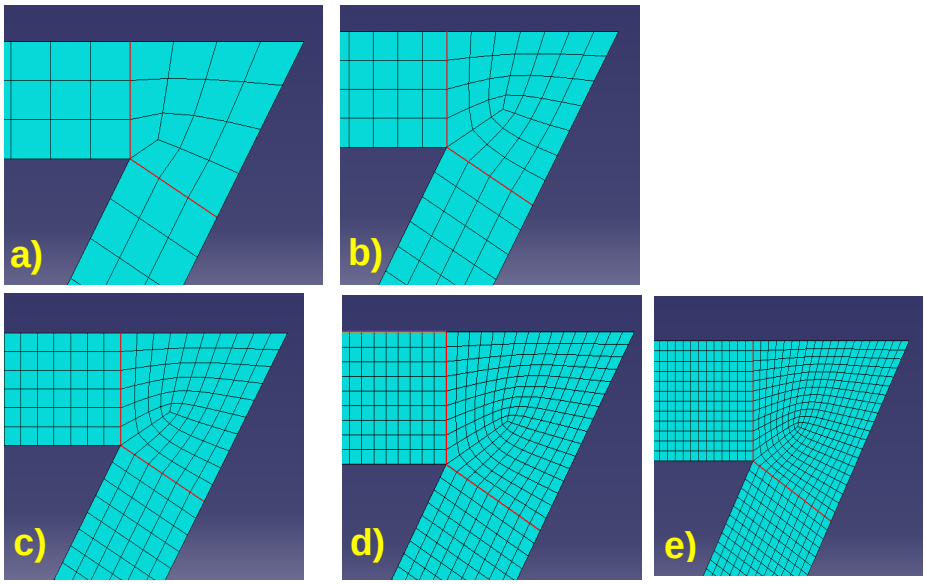

Figure 3-15. Representation for different number of elements: 3 (a), 4 (b), 6 (c), 9 (d), and 12 (e) elements across thickness for convergence test.

As shown by Table 3-2, convergence was shown by an increase in the total reaction forces as the number of elements increased across the thickness of the structure.

A percentage accuracy of ~1.5% reaction force was found from the model analyzed having 6 elements across the vertical and diagonal thicknesses of strips. It was decided to use 6 elements across the thickness of each part during the analysis of L and XXL models, which have similar length to thickness relation (or relative density).

Element Length :	# Elements across	Total Reaction Forces Top Surface			Maximun In Plane Strain		
		Value (N)	% Accuracy (9x9)	% (Most accurate 12x12)	Value	% (9x9)	% (12x12)
8.00E-05	3x3 quad (91,082)	723.90	9.40	9.86	3.58E-03	22.33	24.69
5.00E-05	4x4 quad (195,602)	760.20	4.86	5.34	3.90E-03	15.59	18.16
3.50E-05	**6x6 quad (419,162)**	**786.90**	**1.51**	**2.02**	**4.32E-03**	**6.33**	**9.18**
2.25E-05	9x9 quad (979,202)	799.00	0.00	0.51	4.61E-03	0.00	3.04
1.75E-05	12x12 quad (1,674,482)	803.10	Does not Apply	0.00	4.76E-03	Does not Apply	0.00

Table 3-2. Convergence test data shown for a XXL mechanical model at 4% strain. Two parameters were used for convergence: total reaction forces at top rigid bodies and maximum in plane strains.

Chapter 4:
Mechanical characterization of novel re-entrant cellular solids spine implants.

Introduction:

A cellular solid such as cancellous bone is a structure made up of an interconnected network of solid struts or plates called cells. Whole bones look mostly solid; however it encloses a core of porous cellular bone tissue called cancellous bone. The presence of this type of bone reduces weight while still meeting its primary mechanical function, support of the body [1]. In some instances (as at joints between vertebrae or at the ends of the long bones) this configuration minimizes the weight of bone while still providing a large bearing area, a design which reduces the bearing stresses at the joints. Many bone fractures or abnormalities in vertebrae, hips and wrists occur due to abnormally high bone porosity even under normal mechanical loading. Implants to overcome these abnormalities are used extensively in all these areas. Biomedical applications need to understand the behavior of cancellous bone since it is replaced and/or interfaced with numerous orthopedic implants. For example, in artificial hips most of the bone tissue removed to accommodate the implants is cancellous tissue.

The mechanical behavior of cancellous bone is typical of that of a cellular solid, and can be analyzed by similar principles. Gibson and Ashby [1] mentioned that the single most important feature of any cellular solid is its relative density defined as the relative density ratio "ρ^*/ρ_s", which is defined as the apparent density of the cellular solid divided by the density of the solid material that makes up the structure.

Additionally, it is highly important to mention the current studies of bone at small strain levels due to the different discrepancies on what is actually occurring at these strains (below 1.2% strain). Morgan et. al [2, 3] studied 155 cylindrical cores from human vertebrae, proximal tibiae, proximal femora, and bovine proximal tibiae to characterize the subtle stress-strain non-linearity. Tension and compression axial testing up to 0.4%

strain was performed. Nonlinearity in the initial stress-strain curve was found for all anatomic sites in both compression and tension. Earlier investigators [4] concluded that the pre-yield behavior for every specimen was fully linear indicating that the non-linear 'toe region' is due to an experimental artifact.

Two main characteristics of cancellous bone were used and compare with mechanical cellular solids prototypes handcrafted in this investigation: the modulus of elasticity in the linear elastic region and the potential non-linearity at small strains. Based on a previous experimental study [5], re-entrant metallic open cell foams present non-linearity at small strains within linear elastic region which can be compared to those found in cancellous bone [2]. However, this process did not provide a control over the pores or cells during manufacturing. It is hypothesized that if more controllable re-entrant cellular solids can be manufactured, its mechanical behavior can be tailored to provide similar mechanical behavior of cancellous bone.

Two-dimensional re-entrant metallic cellular solids with controllable parameters were manufactured during this investigation. These cellular solids had hexagonal cells with inverted segments in bowtie shapes. Three structures with different shapes were manufactured [6], and mechanically tested over the linear elastic region for evaluation and characterization. The structures manufactured were also simulated with commercial finite element analysis (FEA) software (Abaqus 6.8, Simulia, Providence, RI) [9]. The relationships between relative modulus of elasticity (E^*/E_s), relative density (ρ^*/ρ_s), where the superscript "*" defines the apparent modulus of elasticity or apparent density and the subscript "s" represents the modulus of elasticity or density of the solid material used. In addition, compressive strain ratio (CSR) was also evaluated using a non-contacting method and optical reflective targets over small strains to verify the existence of a re-entrant behavior in the structures [10]. Compressive strain ratio was used to represent the structures' Poisson ratio. CSR represents the ratio between axial and transverse deformation in compressive testing (CSR) while Poisson's ratio is defined in tensile testing.

Materials and methods

Preparation of specimens:

Large (L), extra-large (XL) and double extra large (XXL) bowtie structures (n=3) with different dimensions were manufactured using 302 grade stainless steel series (SS-302). Mechanical properties such as modulus of elasticity (200 GPa), Poisson ratio (0.3) and density (7860 kg/m^3) were recorded as the materials properties. Table 4-1 and Figure 4-1 show the geometrical dimensions of the structures manufactured.

Specimen Type	L	XL	XXL
Number of Structures	3.0	3.0	3.0
Width (mm)	7.5	16.5	16.5
Length (mm)	4.0	8.0	8.0
Thickness (mm)	0.102	0.102	0.204
Depth (mm)	24.5	24.5	24.5
Angle θ (degrees)	60	60	60
Relative Density	0.041	0.024	0.044

Table 4-1. Dimensions of all the bowtie mechanical structures.

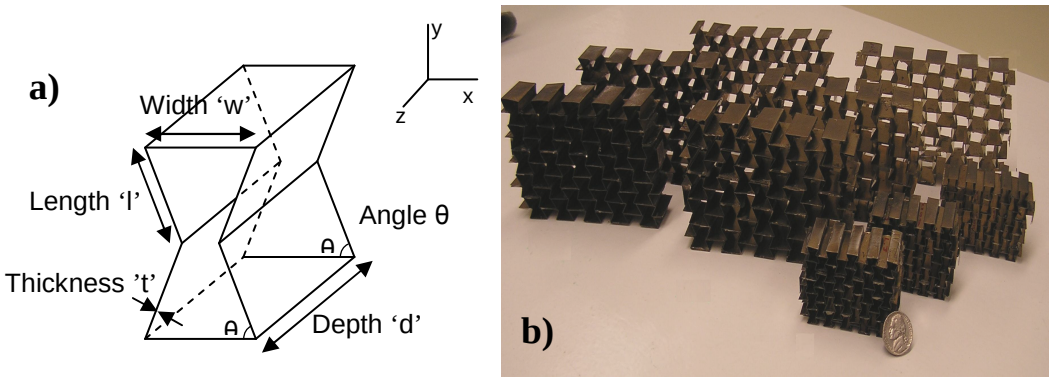

Figure 4-1. Geometric dimensions of a bowtie structure (a). All mechanical structures manufactured (b).

Stainless steel 302 series shim rolls (Precision Brand, Downer Grove, IL) were purchased and cut into 1 inch wide strips using a precise shear machine. After adequate

quantity of strips were cut, they were placed into a conventional oven at 650-700 degrees Fahrenheit for two hours to anneal and relieve residual stresses caused by cutting the strips [7]. The strips were allowed to cool down for a day at room temperature. Once strips were stress-relieved, they were bent to 90 degrees with a bending braking machine (MicroMark, Berkely Heights, NJ). Following 90-degree bending, they were manually bent to 60 degrees with aluminum templates. At this point, strips were subjected to a second stress relief annealing process while attaching the strips to each other uniformly with bulldog clips and metallic templates to maintain an adequate position. After the second annealing process, the surfaces were sandpapered with 220-A grit paper and finally cleaned with acetone for assembling. Strips were glued and assembled together using two part curing epoxy. Bulldog clips and wood templates were used to attach each strip. After assembling, the structures were left overnight for the epoxy to fully cure [8].

Testing Protocol:

Once the thickness, height, width, and weight were recorded in all the specimens, they were subjected to axial cyclic compression using a servo hydraulic machine (Mini Bionix 858, MTS, Eden Praire, MN) at two strain levels. Structures were placed in an extended self-alignment platen (bottom) and compressed with a fixed platen (top). Petroleum jelly lubricant was used to decrease the friction between the platens. Structures were preconditioned cyclically with a compressive force control from 1N to 10N to let the lubricant set between the platens and the structures. After preconditioning, the displacement control was zeroed at a compressive for of 10N. At this point, most of the top/bottom structure surfaces were touching the platens but due to manufacturing limitations, there were some misaligned surfaces that were still not touching the platens. This is why the zero displacement was started at the highest compressive preconditioning value. Ten axially compressive ramp cycles up to 0.01 at a frequency of 0.423 mm/sec (1 inch/min) were applied to each structure. The process was repeated for maximum strain of 0.04 strain. Five runs were

repeated for each structure at each strain level. During each different run, the structures were moved away and back into the platens to account for variability of placement within the platens.

Preconditioning was repeated for each run. Force was collected from a 2.5kN load cell and axial displacement was taken from an LVDT sensor connected to the servo-hydraulic machine MTS Bionix II (MTS, Inc). For the transverse displacement, optical targets were made out of reflective tape and placed on the transverse edges of the structures. Transverse displacements were collected using an optical non-contacting sensor for small displacements (MTI –2100 Photonic Sensor, MTI Instruments Inc, Albany, NY). Due to displacement equipment limitation (±300 μm), transverse displacements were only measured up to 0.01 strain. All data was collected using the MTS acquisition system (TestStar II, MTS) every 100 Hz. Figure 4-2 shows the test up for a typical structure.

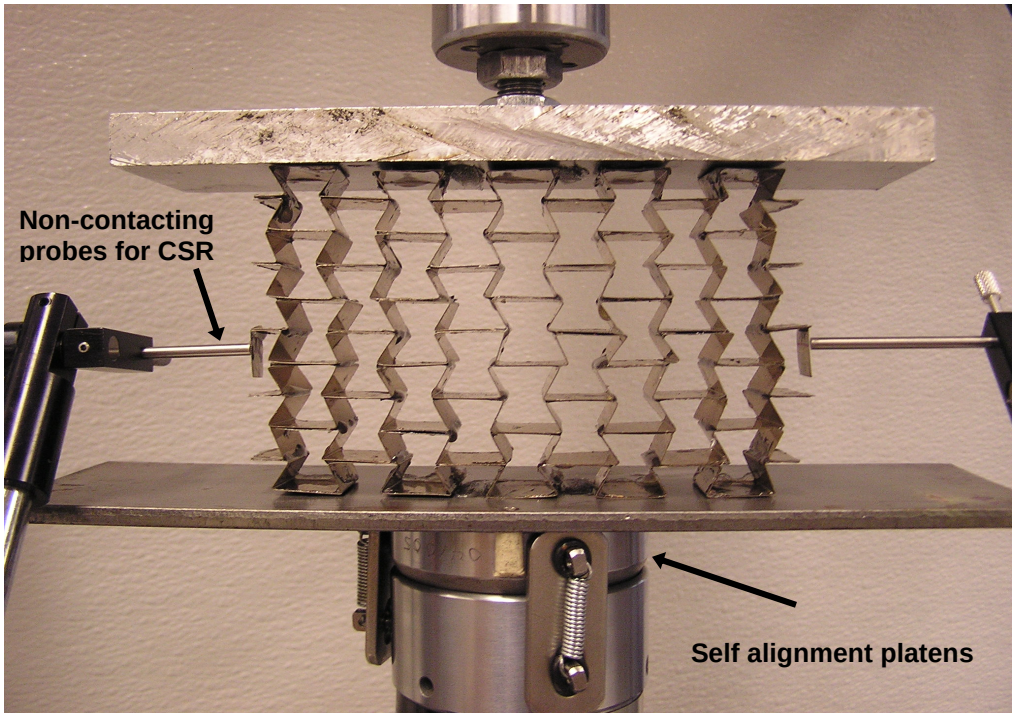

Figure 4-2. Test set up for a typical structure at small strains (0.01). Similar test set-up was applied for strain up to 0.04 without reflecting the reflecting targets due to MTI limitations.

Finite Element Modeling:

Experimental results were compared to FEA mechanical simulations for three different models created in commercial computer software (Abaqus 6.8.2). The structures were modeled with the characteristics found in Table 4-1 and the mechanical properties presented in previous section. A convergence study was performed to appropriately assign the number and size of elements used in the model. Stress analysis quadrilateral 2D plane–strain elements (six elements across thickness) were chosen to model the structure and two analytical rigid bodies to model the self-alignment platens where boundary conditions were applied. Static displacement up to 0.04 strain in the y-direction was applied to the top rigid body while keeping the bottom analytical rigid body fixed in the x and y direction. A middle node representing symmetry in the x and y planesplanes on each model was fixed transversely for the structure not to slide horizontally. Frictionless interaction was applied between the analytical rigid bodies and the structure to model lubrication and contact between the platens and structure. Compressive forces and displacements were collected at every 1/100 increment of top surface displacement. An apparent structural stress strain curve was drawn from these results and compared to experimental results.

Results

Elastic Modulus and Relative Density:

Stress strain curves were plotted when the structures were subjected to axial cyclic compression up to 0.04 strain using Matlab programs (Math Works Inc, MA). The averages of the five loading and unloading cycles in each structure were calculated (Appendix B). A linear fit was applied to a selected linear region in the loading cycle as shown in Figure 4-3. From this linear fit, the slope of the apparent stress strain curve was treated as the average apparent modulus of elasticity of the structure (E*). Hysteresis was small in all the structures at every run and overlapping of loading and unloading cycles show that structures were loaded in the linear region.

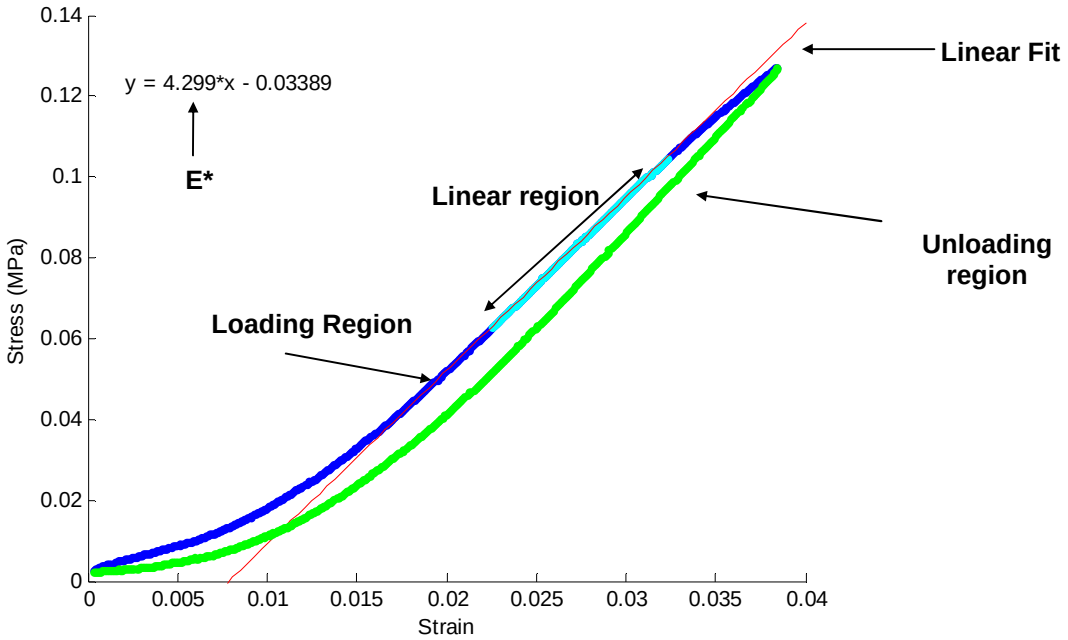

Figure 4-3. Linear fit for L-2 structure to calculate modulus of elasticity in the structure.

Similar procedure was applied to the values collected from the finite element analysis. Total reaction forces and y-displacements applied to the rigid body was collected every 1/100 step increment during the static analysis and converted into apparent stress-strain curves.

The apparent modulus found from each structure is presented in Figure 4-4**.** Large specimens with smaller dimensions presented the largest variability due to more demanding manufacturing process. It was more difficult to assemble and prepare each strip with the adequate 60 degree bending template thus giving a higher variation in the results. XXL and XL specimens present similar values for each type in all the three specimens manufactured. However, there is a difference between the FEA and the manufactured structures. FEA models presented higher elastic modulus for every structure

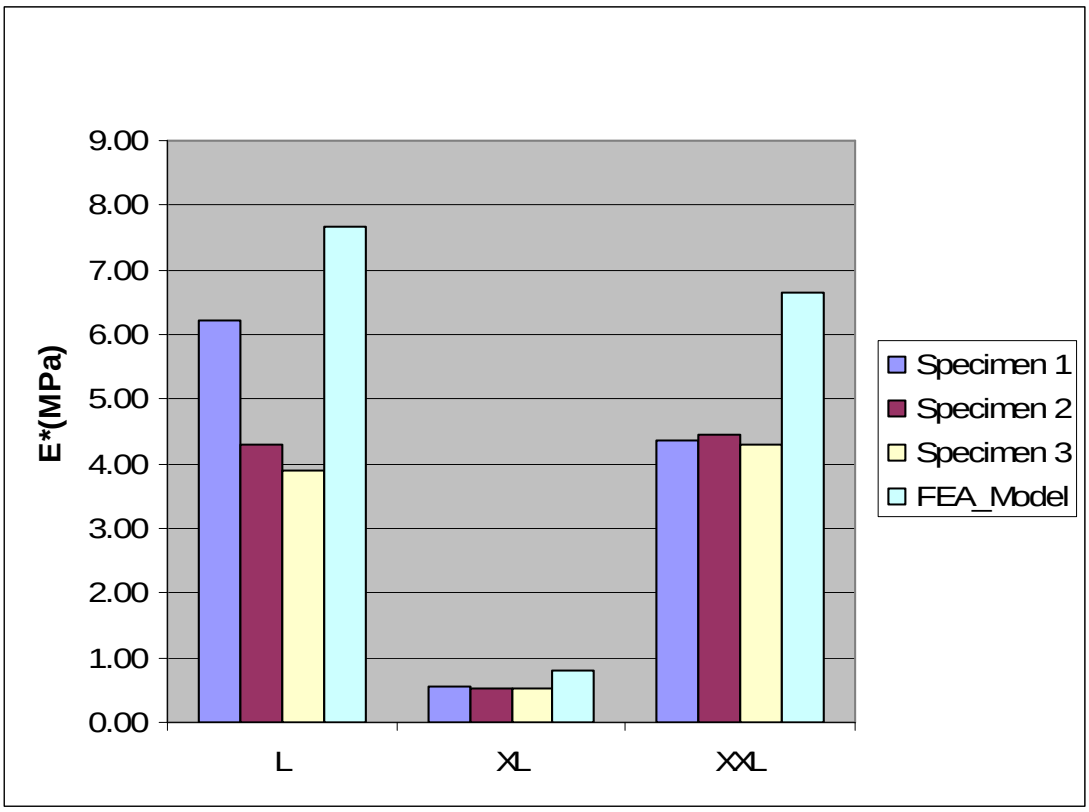

Figure 4-4. Apparent elastic Modulus (E*) for every structure (experimental and

FEA models presented higher apparent modulus of elasticity due to simulation of optimal manufacturing structures with even surfaces and sharp radii of curvatures. Uneven surfaces due to slight differences in bending angles or thickness could cause

the variation of the results in handcrafted structures. Also, the radius of curvature in each angle could yield lower stiffness values during experimental testing. Figure 4-5 shows the difference between the simulated angle and the radius of curvature for an experimental structure.

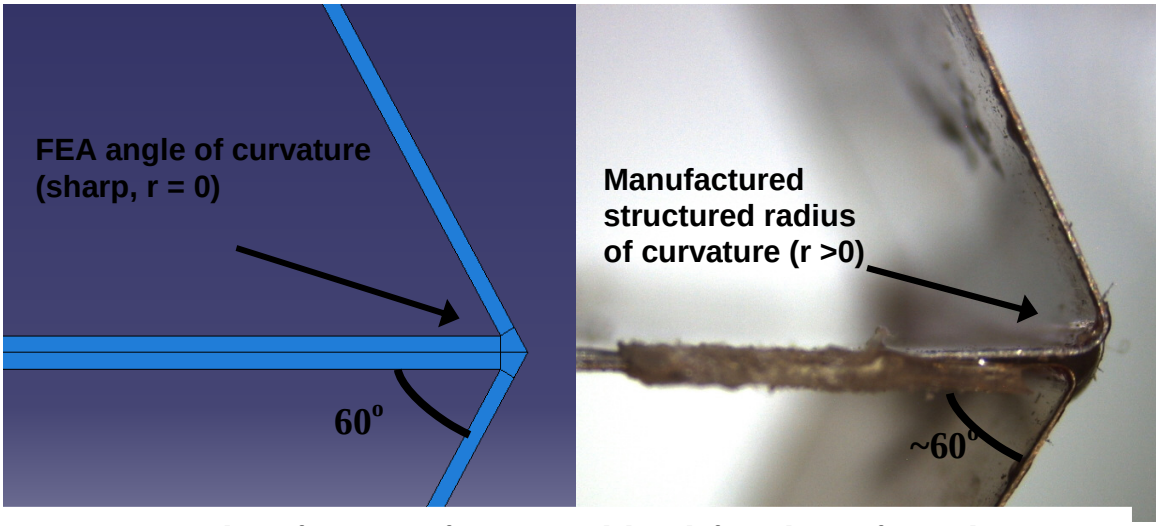

Figure 4-5. Radius of curvature for FEA model (in left) and manufactured structure (in right).

The ratios between experimental and FEA apparent moduli for each structure were consistent, indicating a good approximation but with FEA models giving consistently high values (Table 4-2). Similar behavior was also found between the three structures during mechanical testing and during FEA analysis. As shown, there is a direct linear correlation between relative density and apparent elastic modulus from the structures from both experimental and finite modeling data.

	L	XL	XXL
Apparent Modulus (MPa)			
Experimental	4.80 (1.23)	0.52(0.02)	4.22 (0.07)
FEA	7.68	0.80	6.64
Ratio Exp. To FEA	0.63	0.64	0.64
Relative Density (ρ^*/ρ_s)	**0.041 (0.001)**	**0.024 (0.001)**	**0.043 (0.002)**

Table 4-2. Average elastic modulus (E*), ratio experimental testing to FEA, and relative density (ρ*) for the three type of structures. Standard deviations are presented in parenthesis for mechanical tested structures.

Structures with higher relative densities (L and XXL) present similar apparent modulus of elasticity due to their similar relative densities (0.041 and 0.043) while XL structure present a much more flexible behavior for both: experimental and FEA. The XL structures with almost 50% smaller density present a smaller magnitude for modulus of elasticity of about eight to nine times smaller than L and XXL structures.

Theory from Gibson and Ashby show that during the linear region of the apparent stress strain curve, the apparent modulus of elasticity is proportional to second power of its relative density ($E^*/E_s = C_1 . (\rho^*/\rho_s)^2$). Figure 4-6 shows the experimental linear correlation between relative modulus and relative density of every structure. Jaumard showed in previous study [6] that the theoretical C_1 coefficient chosen was equal to 0.016. It was found that the overall best fit value for the coefficient C_1 with respect to all the structures was equal to 0.012. The best fit coefficient for each structure is presented in Table 4-3.

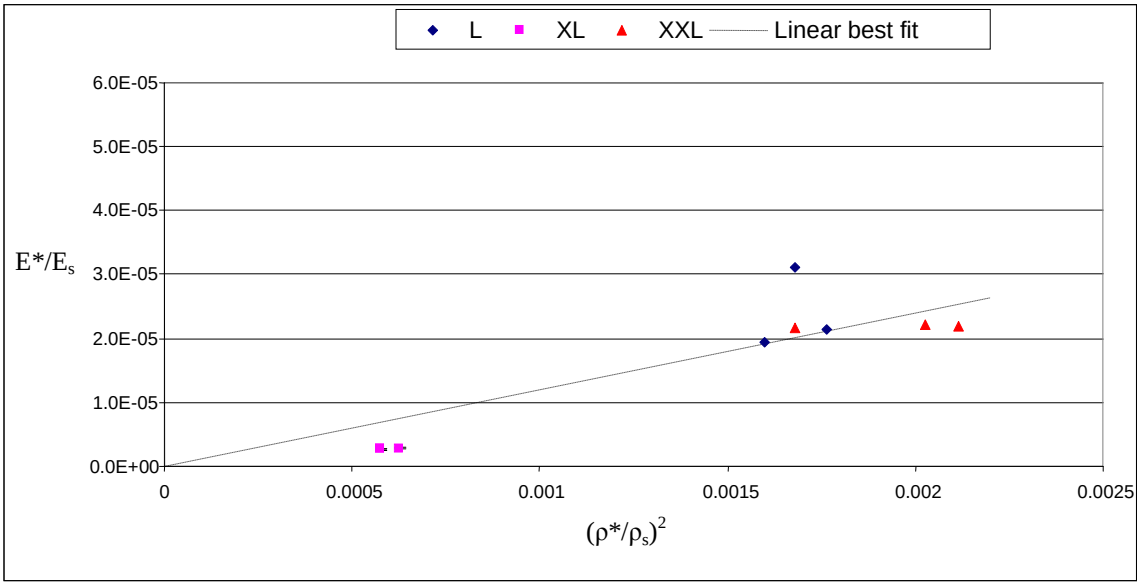

Figure 4-6. Theoretical and experimental values of the ratio between relative modulus and relative densities.

Coefficient $(E^*/E_{s)} = C_1(\rho^*/\rho_s)^2$		L	XL	XXL
C1	Specimen 1	0.019	0.005	0.010
	Specimen 2	0.012	0.005	0.011
	Specimen 3	0.012	0.005	0.013

Table 4-3. Coefficient C_1 that relates relative modulus to the second power of relative density as shown by Gibson and Ashby.

Non-linear behavior at apparent stress/strain:

Apparent strain and stress curves of every structure are plotted in Figure 4-7. Non-linear behavior was found as expected in L and XXL specimens that present higher relative densities than XL specimens. For L and XXL structures, at strains smaller than 0.015 there exists a concave upward region in the apparent stress-strain curve and then stress increases linearly. The apparent stress strain behavior of L and XXL structures was very due to their similar relative densities (0.041 and 0.043). The three XL specimens have a comparable behavior but without the presence of non-linearity. Similar results were found in previous study [6] for the behavior of each structure.

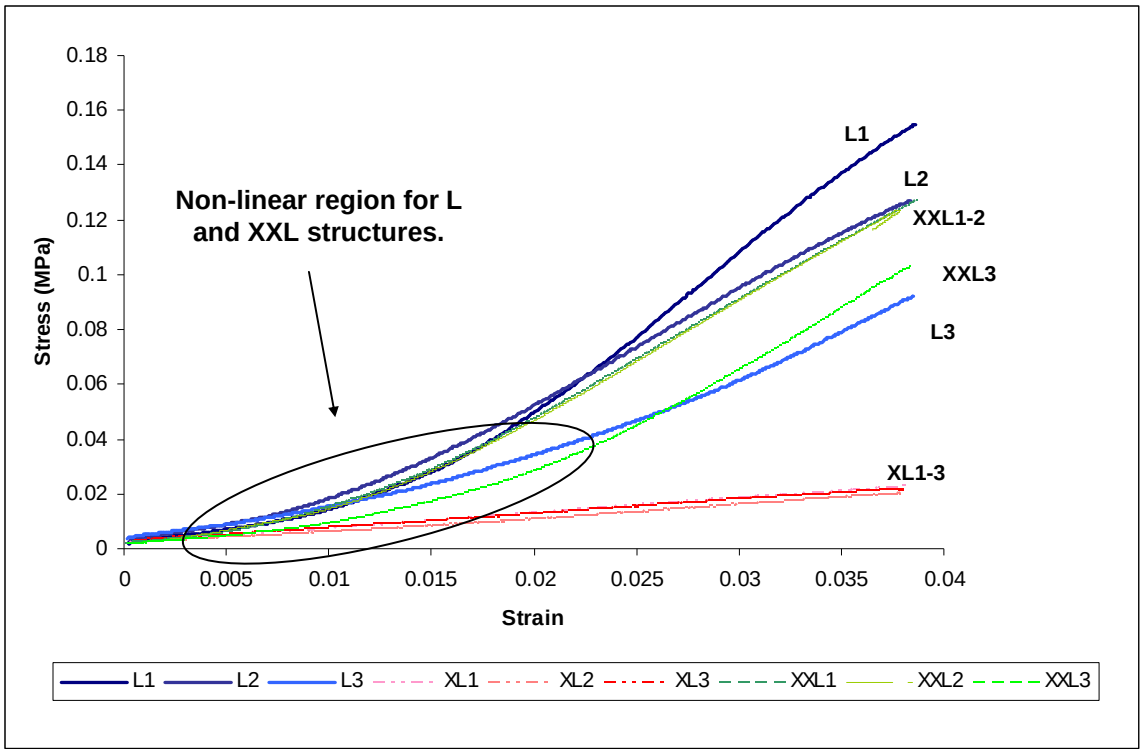

Figure 4-7. Apparent stress strain curves up to 0.04 strains for every structure. Non-linear region was found in L and XXL structures with higher and similar relative densities. Linear behavior was found in all XL structures.

On the contrary, FEA results do not present any non-linear region in any structure. Figure 4-8 shows the mechanical behavior of each model simulated in FEA. As mentioned before, this predicts optimal manufacturing methods while avoiding error in testing and symmetry between each surface. The concave upward curve could be related to the period when the uneven flattened surfaces become in contact with the compressive platen. Once all the surfaces are in full contact, the linear region of the elastic curve begins.

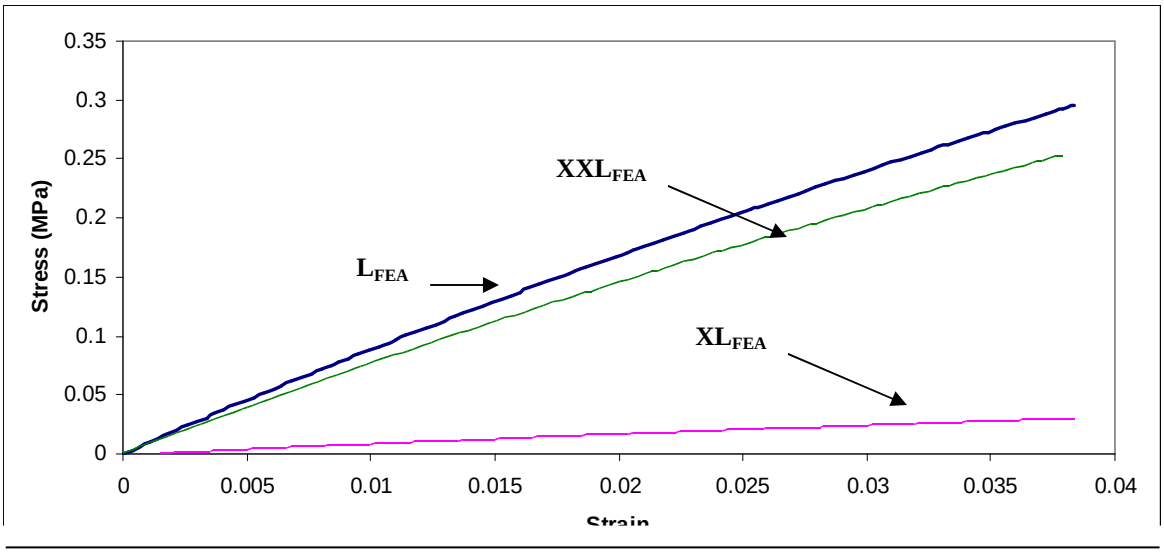

Figure 4-8. Stress strain curve for finite element analysis models for every structure. No presence of non-linearity was found for L and XXL models which contradict experimental results.

Compressive Stain Ratio:

The compressive strain ratio was evaluated for every structure and also modeled using FEA. During experimental testing, strain values up to 0.01 strains were evaluated due to limitation in the non-reflecting measuring method which has a displacement limit of ±300μm. All values for every specimen (experimental and FEA) were negative and confirmed the re-entrant behavior of the structures. Large and XXL structures demonstrated similar CSR while a higher magnitude value was found in the XL structures. As shown in previous studies [6], the values of XL structures presented the largest negative compressive strain ratios up to 2 to 4 times greater in magnitude than the L and XXL structures. Figure 4-9 illustrates the values of each structure at three typical strain levels: 0.005, 0.0075 and 0.01. The y lines represent the FEA results while the bar graph represents the experimental results. The average CSR values had no tendency to decrease as strain levels increase. As showed in the figure below, the CSR values kept a constant value at each different strain level.

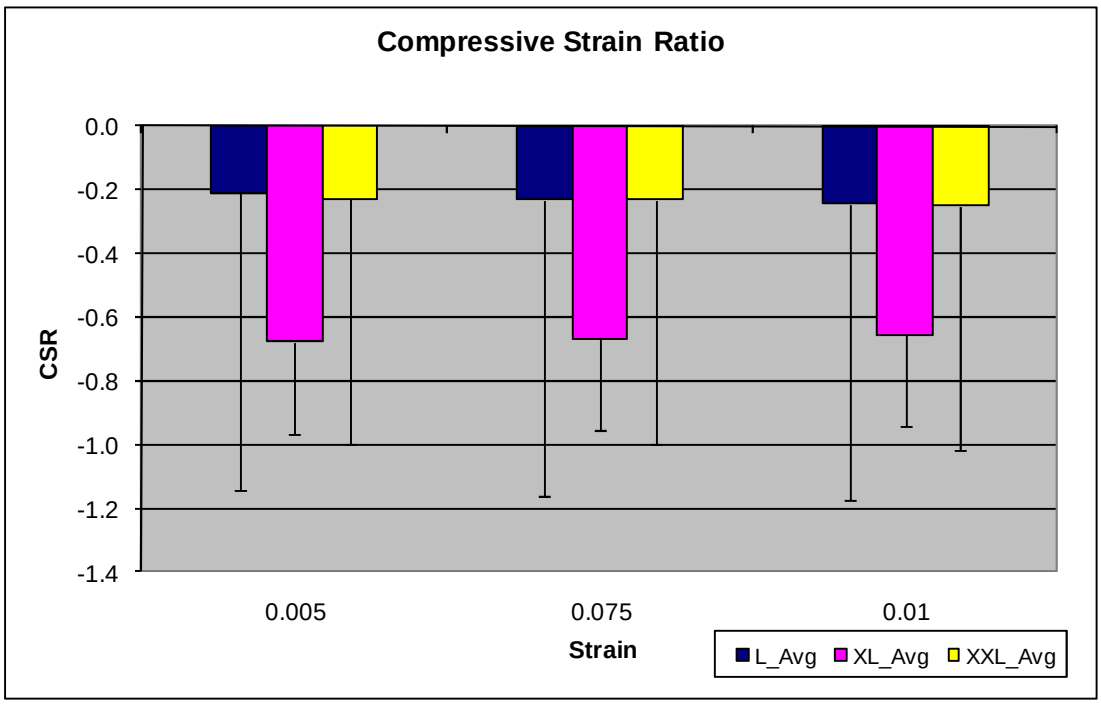

Figure 4-9. Average compressive strain ratio (CSR) values for the structures at three different strain levels: 0.005, 0.0075 and 0.01. FEA model comparative values are shown by the bracket lines.

Finite element results for compressive strain ratios were greater in magnitude than mechanical testing results. The results were also negative in sign, demonstrating a re-entrant behavior in all three models. Large (L_FEA) models presented the highest CSR value while similar magnitude values were presented between XL_FEA and XXL_FEA models. The precise geometry of the FEA model as compared to the laboratory manufactured specimens could explain the higher CSR values. In addition, frictionless interactions between the rigid bodies and models could be another cause of higher CSR magnitudes. CSR values for L_FEA and XXL_FEA models were approximately 5 times greater than manufactured structures while XL_FEA model was around 1.5 times greater than XL structures.

Discussion

As expected from previous study [6], the relative modulus of elasticity can be linked to the relative density of the unit cells. Decreasing the length and/or increasing the thickness will make the structures stiffer which was shown with L and XXL structures while XL structure with a higher ratio between length and thickness were more flexible and thus with lower relative density values. By controlling the aspect ratio (thickness over length) or relative density, the structures have controllable mechanical properties. This study validates the hypothesis that apparent structural mechanical behavior can be tailored (by changing the relative densities) to mimic the characteristics of the replaced or interfaced tissue. Aspect ratio is related to the relative density of the structure as shown by Jaumard [6]. In the case of the cellular metallic bowtie-like structure, the relation between relative density and aspect ratio is presented in Equation 4.1 with dimensions presented in Figure 4-1. Structures with similar relative densities tend to have similar mechanical behavior. In this investigation L and XXL structures have similar apparent modulus of elasticity values, which was expected due to their similar relative densities. Even though there was an improved methodology to manufacture the structures, there was a great variation in L specimens due to its more challenging manufacturing process with smaller dimensions. However, the mechanical behavior of L structures coincided with the values in the XXL structures due to their similar relative densities. Stiffness in the XL and XXL structures had much less variability in all three structures.

$$\frac{\rho^*}{\rho_s} = \frac{Occupied\ Area}{Total\ Area} = \frac{\left(\frac{width}{length}+1\right)\cdot\frac{thickness}{length}}{\left(\frac{width}{length}-\sin(\theta)\right)\cdot\cos(\theta)} \approx \frac{4}{\sqrt{3}}\cdot\left(\frac{thickness}{length}\right)$$

[Eq. 4.1]

In addition, there exist a similar mechanical behavior when structures were modeled using FEA but higher stiffnesses were found. There was a constant relationship between the apparent modulus of elasticity found in experimental data

and that from FEA of about 0.6 times higher (Table 4-2). The higher stiffness in FEA could be due to optimal dimensions modeled and constant sharp radius of curvature (Figure 4-4). Since the radii of curvature varied for every angle at each specimen, there was no adequate approach to model the exact radius of curvature of every angle. In both cases (FEA and manufactured structures), similar apparent elastic modulus behavior was found for L and XXL structures while lower modulus was found for XL structures. The coefficient C_1 that relates the relative densities and relative modulus of elasticity was very similar in L and XXL structures with similar relative densities but half its value for XL structures. Relative densities showed a very important role when determining the mechanical behavior/characteristics of each structures since it existed a linear correlation ($C_1 = 0.012$ and a R^2 of 0.83) in the relative modulus of elasticity versus. relative density curve.

Non-linear behavior at small strains was only found in experimental data while FEA models only showed linear behavior at all strain values. This indicates the existence of experimental and manufacturing artifacts. Because of the variation in manufacturing of the experimental specimens, not all surfaces of the specimens were in contact with the compressive platens at zero displacement. Structures were zeroed at -10N of preconditioning but some surfaces were still not in contact with this preload (Figure 4-10). The initial non-linear region may be due to continued contact during compression that could not be avoided by increasing preload values if small deformation behaviors were to be investigated. When uniform contact is achieved between surfaces and compressive load platens, true linear behavior was observed. XL structures did not exhibit this shortcoming due to their lower rigidity and decreased load required to obtain full contact with the compressive platens uniformly. If a lower preload would have been used, the XL specimen may have also shown the nonlinear artifact. FEA showed that every metallic cellular solid structure with the tested geometry behaved linearly. This computational result differed from previous investigations [5, 6].

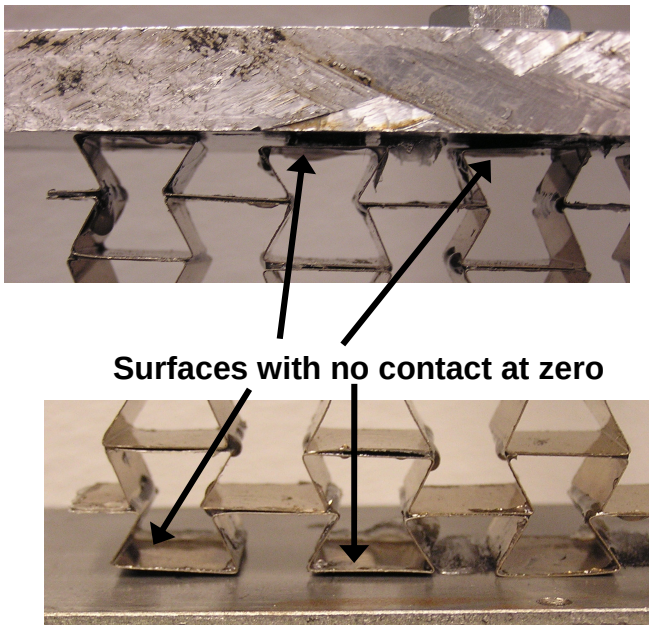

Figure 4-10. Representation of non-contacting surfaces at top and bottom when displacement is zeroed at –10N, which could explain the non-linearity in the stress-strain curve at small differing with FEA analysis.

Compressive strain values showed that every structure analyzed presented a re-entrant behavior which was expected. However, due to the non-contact method used (MTI photonic probes), the CSR were only measured at small ranges (±300 micrometers of transverse deformation). Given the small range of deformation (strain values < 0.01), considerable experimental artifact limitations were created due to the lack of full platen contact at low loads. L and XXL measurements of transverse deformation were tested over the non-linear region, which in some structures were not in full contact with the platens, and thus transverse deformation may have been decreased in this range. Higher levels of displacement were not tested so that the structures were not plastically deformed. Another considerable limitation is the alignment of the reflective probes that do not always remain orthogonal to the structure, which could cause error in the results. Even though limitations on the experimental were found, all structures presented negative compressive strain ratios showing a re-entrant behavior due to the geometry presented.

Conclusion

The actual investigation compared and validated previous results considering non-linear behavior at small strains and apparent stress strain curves [6] and extended their characterization with FEA. The long term goal of this investigation is the ability to tailor the mechanical behavior of metallic cellular solids to resemble characteristics of human bone tissues. Aspect ratio and relative density were found to control the mechanical behavior of these cellular solids. It was confirmed that by controlling the aspect ratio of each structure (or modifying the relative densities), the structures could be tailored to obtain the desired mechanical. The study also indicated that non-linear behavior for inverted segment cellular solids with one dimensional re-entrant behavior is most likely caused due to limitations from manufacturing processes and experimental set up. In this stage of investigation, stainless steel material was used to perform the mechanical evaluation of each structure. The existence of no-artifactual non-linearity is still under investigation with regard to both cellular solids and biological tissues. This study indicated that no non-linearity exists when a cellular solid has one dimensional re-entrant behavior (along the compressive axis). Future work should be investigated using geometrical structures with higher dimensional re-entrant behavior. Different geometries for cellular solids with 2D and 3D reentrant behavior should first be investigated using FEA. Once a promising geometry with non-linearity at small strains (if desired) and adequately controllable mechanical behavior is obtained, the potential cellular solids should be manufactured with improved manufacturing processes, such as rapid prototyping or solid free form fabrication, and experimentally tested for practical performance.

References

[1] Gibson, L., and Ashby, M., 1999, Cellular solids: structure and properties, Pengamon Press.

[2] Morgan, E. F., Yeh, O. C., Chang, W. C., and Keaveny, T. M., 2001, "Nonlinear behavior of trabecular bone at small strains," J Biomech Eng, 123(1), pp. 1-9.

[3] Morgan, E. F., Yeh, O. C., and Keaveny, T. M., 2005, "Damage in trabecular bone at small strains," Eur J Morphol, 42(1-2), pp. 13-21.

[4] Keaveny, T. M., Guo, X. E., Wachtel, E. F., McMahon, T. A., and Hayes, W. C., 1994, "Trabecular bone exhibits fully linear elastic behavior and yields at low strains," J Biomech, 27(9), pp. 1127-1136.

[5] Friis, E., Lakes, R., and Park, J., 1988, "Negative Poisson's ratio polymeric and metallic foams," Journal of Materials Science, 23(12), pp. 4406-4414.

[6] Jaumard, N., 2008, "Mechanical and electromechanical characterization of a novel composite cellular solid for orthopaedic applications: A feasibility study," PhD, The University of Kansas, Lawerence.

[7] Karsen, S. R. B. a. C. D. V., 1992, "Mechanical Fatigue Properties of Stress Relieved Type 302 Stainless Steel Wire," Journal of Materials Engineering and Performance, 1(3).

[8] Inc, A (2004). "Matweb: Material property data." http://www.matweb.com.

[9] Simulia, I., 2008, "Abaqus User Manual v6. 8," Electronic Version.

[10] Dana, E. (1898). A text-book of mineralogy: with an extended treatise on crystallography and physical mineralogy, John Wiley & Sons.

Chapter 5: Electro-mechanical validation of novel re-entrant composite structures for orthopedic implants.

Introduction:

According to the American Academy of Orthopedic Surgeons (AAOS), approximately one quarter-million spine fusions are performed each year [1, 2]. Even though the success rate of spine fusion is very low, the annual number of fusions continues to increase. The use of electrical stimulation has shown to improve the effectiveness of these procedures especially in people who have lower success rates due to risk factors such as obesity, diabetes, smokers, people in need of multi-level fusions, or when a second surgical procedure is needed due to failed primary procedures [3].

Several studies compared the success rates of patients who had undergone anterior and posterior lumbar fusion surgical procedures [3-6]. It was found that the average success rate for patients that went under direct current electrical stimulation was 95% compared to 75% of a non-stimulated group. Also, patients who were smokers and had undergone direct current stimulation had a much higher success rate of 93% compared to 71% for non-electrically stimulated smoker patients [7]. Another study showed a higher success rate of 91% for patients who received direct current stimulation compared to 81% who did not receive any kind of stimulation [8, 9].

Many different methods are currently used to improve spine fusion using electrical stimulation. Each different electrical stimulation method has disadvantages such as surgical insertions and removals, patient conformability, electrical power supply for stimulators, allergy reactions, etc. In this study, the feasibility of a new novel electrical stimulation incorporated within the implant itself was examined. This novel stimulation method may eliminate many of the drawbacks of current stimulators. The use of piezoelectric materials embedded into the metallic cellular structure of the implant is presented where two main advantages are desired. This new methodology will present direct electrical current stimulation in the area implanted with no need of external

electrical power supplies. Charges of opposite signs are generated in the piezoelectric ceramics when an adequate mechanical loading is transferred from the metallic structure to the piezo-ceramic embedded into it. These electrical charges will generate electric potentials, which will create charges to flow in one direction generating an electrical current if the structures are not short-circuited. This electrical current will flow throughout a conductive media (metallic structure and conductive tissue environment) and thus generate electrical stimulation into the injured site or implanted area. The use of piezoelectric materials has been studied in fracture healing and biological fixation of hip and knee replacements, but not in spine fusion implants [10-12]. To this author's knowledge, only one patent has been published on use of direct electrical stimulation without the use of electrodes by transforming vibrational energy into electrical energy [22] but no published literate explained the use of piezoelectric materials to provide this kind of stimulation.

Two types of cellular metallic solids with embedded piezoelectric ceramic plates at the middle regions were manufactured. It was hypothesized that if a compressive force is applied to each structure, the force will be transmitted to the embedded piezo-plate surfaces, generating electrical charges. Mechanical forces were applied to each structure at different frequencies while the structures were electro-mechanically characterized. Finite element analysis (FEA) was utilized to validate the results and compared them with actual experimental testing. This novel electrical stimulation with piezoelectric materials was investigated and compared to direct electrical current magnitudes found to be adequate to enhance bone osteogenesis.

Piezoelectric ceramics present a mechanical deformation when stressed electrically by an applied voltage This type of piezoelectric ceramics are known as piezoelectric actuators. Conversely, when piezo-electric ceramics are stressed mechanically by a force, and generate an electric charge and are known as piezoelectric sensors. If the opposite charges of the two polarities are not short-circuited, a voltage associated with the charges appears. This effect of piezoelectricity is a combination of electrical behavior and Hooke's law. The equations representing this behavior are usually

derived from the thermodynamic potentials, which are a necessary consequence of the principle of conservation of energy, but they can be obtained directly from this principle [30]. The g-form set of equations are the best representation of the piezoelectric sensor effect (Equation 5-1 and 5-2). While all equations are tensorial, the indices have been omitted for brevity.

$$\varepsilon = S^{q} \cdot \sigma + g_{ij}^{\phi} \cdot q \qquad \text{[Eq. 5.1]}$$

$$E = -g_{ij}^{\phi} \cdot \sigma + (K^{\phi(\sigma)})^{-1} \cdot q \qquad \text{[Eq. 5.2]}$$

Where ε is strain, S^q is the elastic compliance (m^2/N) at zero electric displacement q (C/m^2), σ is stress (N/m^2), g_{ij}^{φ} is the piezoelectric voltage coefficient (V-m/N or C/m^2) where subscript "i" denotes the direction of force being applied and subscript "j" denotes the poling direction, E is the electric field (V/m), and $K^{\varphi(\sigma)}$ is the electric permittivity (C/V-m) at zero stress. In an infinite ideal parallel plate, the electric field E generated is equal to the voltage V divided by the thickness of the piezoplate [14]. Since the length of the piezoplate embedded in the metallic structures under investigation is relative larger than the thickness (t << l), the piezoelectric behavior can be modeled as an ideal parallel plate yielding to a direct relation between voltage and stress:

$$E = \frac{V}{t} = -g_{ij}^{\phi} \cdot \sigma + (\mathrm{K}^{\phi(\sigma)})^{-1} \cdot q \qquad \text{[Eq. 5.3]}$$

Materials and methods

Preparation of specimens:

Five p-extra-large (pXL), and five p-double extra large (pXXL) metallic cellular solid prototypes with inverted segments (bowtie like geometry) were handcrafted

manufactured using 302 grade stainless steel (SS-302) series (Precision Brand Inc, Downers Grove, IL). Large dimension piezoelectric structures (pL) similar in dimension to large structures (L) made in the previous mechanical characterization were not manufactured in this part of the project as they were hypothesized to have similar electro-mechanical behavior. Table 5-1 and Figure 5-1 show the dimensions of the structures manufactured.

Specimen Type	pXL	pXXL
Number of Structures (n)	5	5
Width (mm)	16.5	16.5
Length (mm)	8	8
Thickness (mm)	0.102	0.204
Angle (degrees)	60	60
Depth (mm)	25.4	25.4
PZT thickness (mm)	1.02	1.02
PZT length (mm)	16.5	16.5

Table 5-1. Dimensions of the electro-mechanical cellular solid structures.

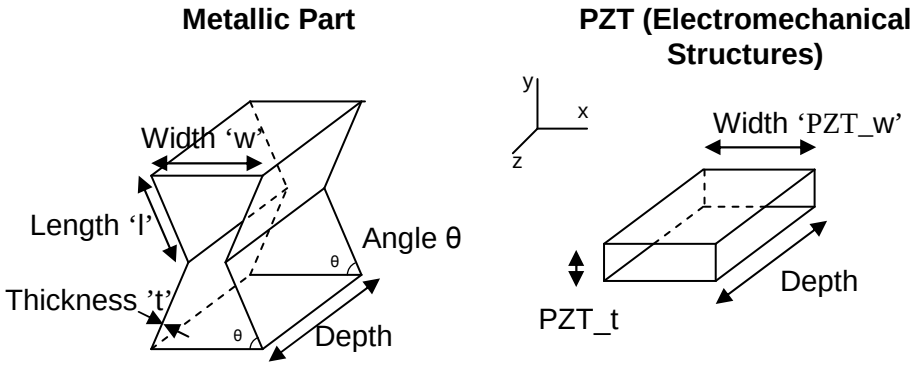

Figure 5-1. Geometric dimensions of bowtie electro-mechanical structure.

Lead zirconate titanate type A (PZT-5A) piezoplates were embedded in the middle surface of each metallic structure. The SS-302 modulus of elasticity was stiffer (200 GPa) than of the piezoelectric plates (52 GPa) while Poisson's ratio values were 0.3 for SS-302 and 0.25 for PZT-5A [15, 16]. Electrical properties of the materials such as electrical conductivity of stainless steel was around 1.39E6 ($S \cdot m^{-1}$). PZT-5A was

classified as a non-conductive media with a resistivity of 1.0E+6 (Ω-m). The piezoelectric g_{33} constant of PZT-5A was 2.40E-02 (m/V).

Stainless steel 302 series shim rolls (Precision Brand, Downer Grove, IL) were purchased and cut into strips using a precise shear machine into 1 inch wide strips. After adequately size strips were cut, they were placed into a conventional oven at 650-700 degrees Fahrenheit for two hours to anneal and relieve residual stresses caused by cutting the strips [17]. The strips were allowed to cool down for a day at room temperature. Once strips were stress-relieved, they were bent to 90 degrees with a bending braking machine (MicroMark, Berkely Heights, NJ). Following 90-degree bending, they were manually bent to 60 degrees with aluminum templates. At this point, strips were subjected to a second stress relief annealing process while attaching the strips uniformly with bulldog clips to metallic templates for maintaining an adequate position. After the second annealing process, the surfaces were sandpapered with 220-A grit paper and finally cleaned with acetone for assembling. Two strips were glued and assembled together using two part curing epoxy leaving a separate surface to assemble the PZT piezoelectric in between. Bulldog clips and wood templates were used to attach each strip. After assembling, the structures were left overnight for the epoxy to cure.

Piezoelectric PZT ceramics were cut to adequate dimensions to match the base of the middle section of the metallic bowtie strips. Silicone was applied to the corners to avoid short circuiting of the piezoelectric generated charges and after allowing the silicone to dry, conductive silver epoxy with 65% silver (Stan Rubinstein Assoc., Foxboro, MA) was used to assemble the plates into the strips and assure conductivity between metallic bowties and piezoelectric plates; the epoxy was allowed to cure for 24 hours. These piezoelectric plates were assembled in the midsection of the structure as shown in Figure 5-2. Once assembled, electrodes were soldered at each bowtie metal strip end to collect electrical voltages.

Experimental Testing Protocol:

Once the thickness, height, width, and weight were recorded in all the specimens, they were subjected to axial cyclic compression using a servo hydraulic machine (Mini Bionix 858, MTS, Eden Praire, MN). Structures were placed in an extended self-alignment platen (bottom) and compressed with a fixed platen (top). An additional insulating surface made out of methyl methacrylate (plexiglas) was added in between the platens and the structures to avoid electrical charge dissipation and/or shortening (Figure 5-2). Structures were preconditioned cyclically with a compressive force control from 1N to 10N to let the lubricant set between the platens and the structures. After preconditioning, the displacement control was zeroed at a compressive force of 10N.

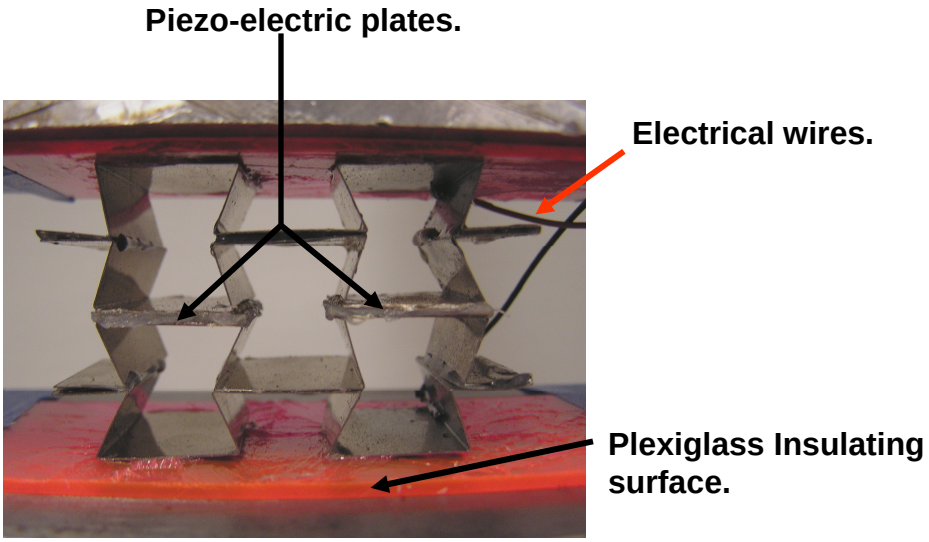

Figure 5-2. Test set up for every structure. Piezoelectric plates were embedded in the middle section of the structure while a non-conducting methyl methacrylate surface was added in the top and bottom surfaces to avoid shortening. Electrical wires soldered into the metallic structures conduct the

Piezoelectric structures were subjected to 10 sine wave cycles of axial compression at different frequencies (1Hz and 2Hz) up to 0.01 strain. Additional testing was repeated for 0.02 strains. The frequencies selected were comparable to the walking cycle frequencies found in different studies [18-20]. The recorded strain values emulate

the small deformations desired in the implantable spine fusion devices. However, due to unsuccessful recorded electrical data collected in pXL structures, an additional compressive test up to 0.04 strain was applied to this type of structure. Three runs were repeated for each structure to avoid experimental error. During each different run, the structures were taken out and remounted to account for variability due to specimen placement. Axial force and axial displacement were collected every 0.01 of a second for mechanical data. Alternating voltage coming directly from the piezoelectric structure was also collected using the data acquisition system (TestStar II MTS, Eden Prairie, MN). In addition to the sinusoidal voltage measurement, a simple rectified electronic circuit made out of Scottky diodes with small electrical voltage drops and a 0.97uF capacitor were used to convert the alternating voltage into direct voltage. Direct current was then calculated by Ohm's law in a known electrical resistor value (475 kΩ) and thus compare to results of previous investigators [5, 9, 18, 19, 21-27]. It was first suggested to use a resistance value similar to the body fluid found in the human body, but a higher resistance value was applied so that current values would be within the measurement range of the data collection system.

Figure 5-3 shows the simple electronic circuit used to rectify the signal. Four diodes are present in this circuit, which conducts voltage in pairs. Diodes D_1 and D_2 conduct together, and D_3 and D_4 conduct together. The voltage across the load is positive when D_1 and D_2 are on. The voltage across the load is negative when D_3 and D_4 are on [28] thus converting all the negative phases of the sine wave into positive phases. The alternating voltages will charge a large capacitor placed in parallel with the circuit at each sine wave. The time the capacitor discharges will ripple back with the next sine wave thus converting the alternating voltage in slightly oscillating direct voltage (V_{DC}). The time the capacitor discharges is smaller than for the next sine wave and thus the output voltage ripples and becomes essentially direct voltage. The voltage difference across the resistor (V_R) divided by the known resistance gave a direct electrical current value.

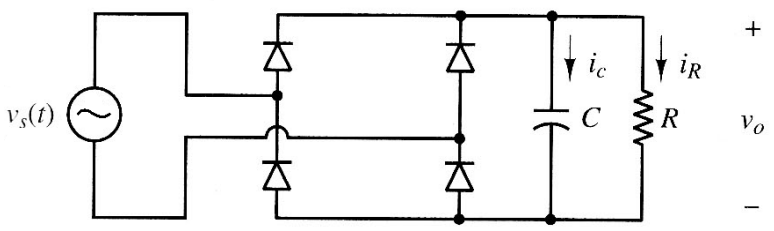

Figure 5-3. Electronic circuit to rectified the signal coming from the piezoelectric (Vs) into an essential dc voltage (Vout).

Finite Element Analysis:

Plane strain finite element analysis (FEA) was utilized to verify axial stress distributed at interaction points between the piezoelectric plates and the metallic structures at different assembling and bonding stages. The structures were geometrically modeled with dimensions found in Table 5-1 and mechanical properties specified in previous section. Stress analysis quadrilateral 2D plane–strain elements (six across the thickness) were used. In addition, two analytical rigid bodies were created to apply the difference boundary conditions (Figure 5-4). Static displacement up to 0.02 strain in the y-direction was applied to the top rigid body while keeping the bottom analytical rigid body fixed in the x and y direction. A middle node representing symmetry in the x and y planes on each model was fixed transversely for the structure not to slide horizontally while the simulation runs. Additionally, four different bonding states with different contact interaction between the piezo-plates and stainless steel were modeled to verify the difference in accurate bonding. First, fully fixed contact interaction along the entire interface simulated optimal conductive epoxy bonding. Subsequently, 0.1, 0.2, and 2.0 mm of separation length (where compressive, but not shear or tensile load transfer were allowed) and incorrect bondings at the corners were simulated.

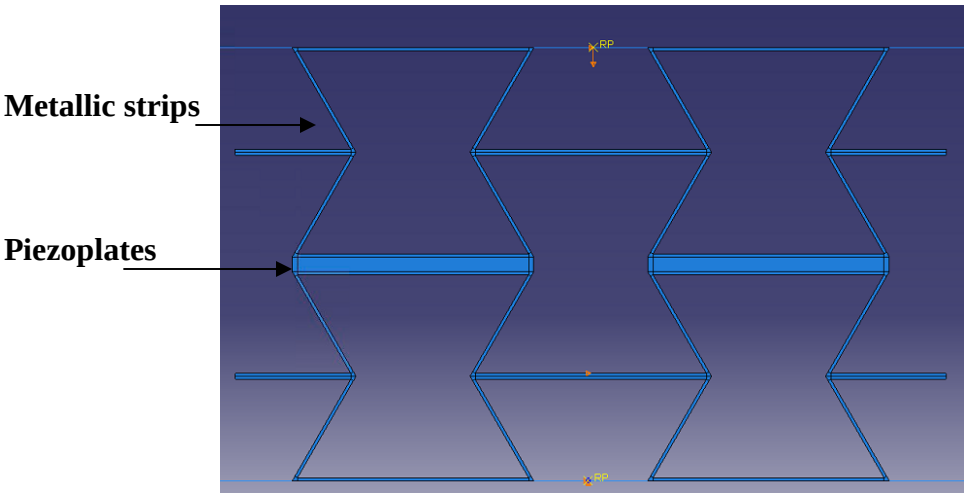

Figure 5-4. Electromechanical structures modeled in FEA with piezo-plates embedded in the middle section of the metallic structure. Boundary conditions are shown in orange: displacement in the top rigid body, x- fixed in the bottom symmetrical section of the bowtie and x-y-fixed in the bottom rigid body.

Results:

Electro-mechanical testing:

The following results present the average data of 24 cycles: eight cycles at three different runs. The first and last cycles were eliminated from the data to avoid placement artifacts. For the rectified electrical data, two more subsequent cycles were eliminated to avoid instability while waiting for the capacitor to charge during signal rectification in the electronic circuit (EC). Figure 5-5a shows the voltage generated with each cycle at each different frequency. Further figures for all the other structures are provided in Appendix D. As shown by Figures 5-5a, the alternating voltages (V_{AC}) increase with an increase in frequency making the structures frequency dependant. In addition to alternating voltages, rectified voltages are also presented as a smooth line with small values close to zero. This line represents the direct electrical voltage (V_{DC}) and direct electrical current (I_{DC}).

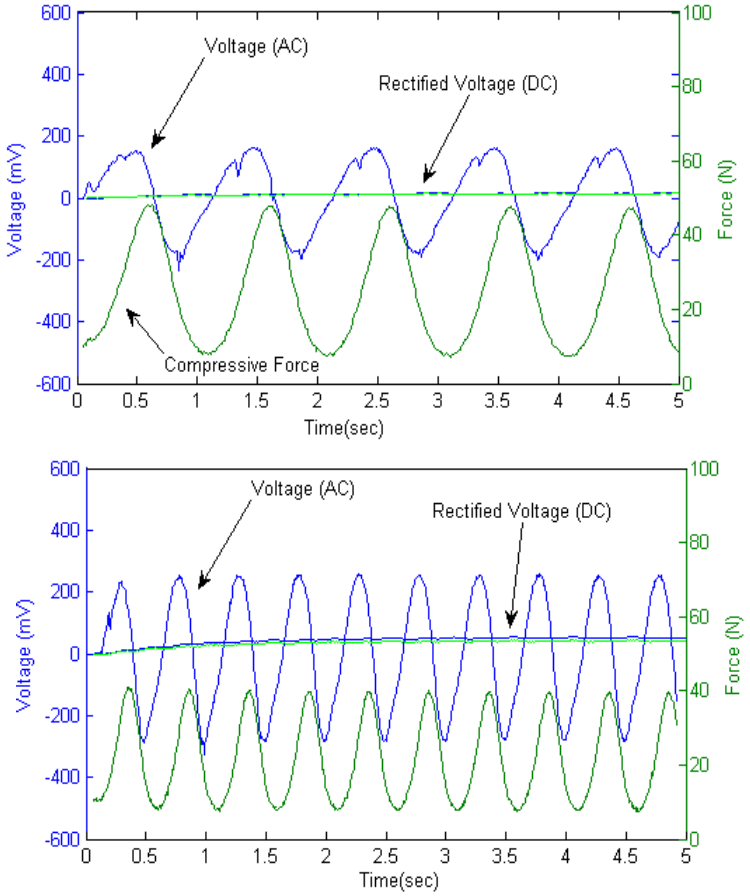

Figure 5-5a. pXXL1 structure voltage (AC and rectified) when subjected to sine wave compressive cycles up to 0.01 strain at two different frequencies 1Hz (top) and 2Hz (bottom).

A zoomed figure of the rectified electrical signals is presented in Figure 5-5b**.** Rectified electrical current (I_{DC}) and voltages (V_{DC}) are presented. Due to sensitivity of the data acdquisition sytem, the V_{DC} of the resistor had to be calculated implicity. The direct voltages (V_{out} piezoplate) and the direct voltage with an added resistor ($V_{Resistor}$) passing in series were measured. The difference in voltage was shown as the voltage of the resistor. Electrical current was then calculated by dividing the voltage difference with the resistor value and presented in the figure. The figure shows how the voltage ripples due to the charge and discharge effect in the capacitor and the sinusoidal alternating

voltages. A small rise is observed at the beginning which shows the region where the capacitor is charging. Even though Schottky diodes were used due to their low forward voltage drops, the electrical magnitudes found in this current investigation showed a very high voltage drop between the alternating voltage and the direct rectified voltage. Electrical current at 2Hz in the figure structure was found to be ~0.02 μA. Due to

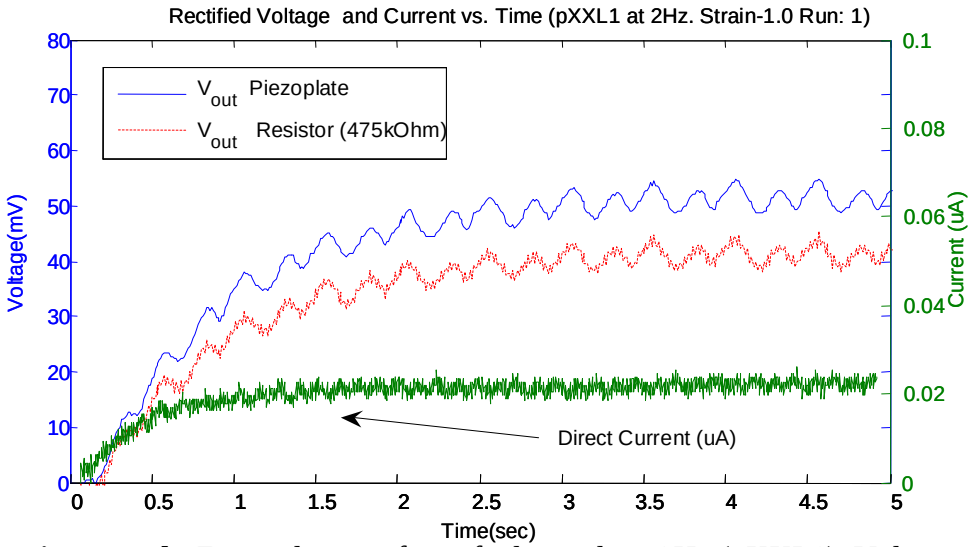

Figure 5-5b. Zoomed view of rectified signals at 2Hz (pXXL1). Voltage ripples are shown due to the charging and discharging of the capacitor at the different alternated sine waves.

Compressive forces were also recorded for every structure. Stiffer structures (pXXL) presented higher compressive forces for the different strain levels. Figure 5-6 shows the change in compressive forces for every structure at different strain levels with different frequencies. Standard deviations are presented as y-error lines. A greater magnitude of compressive force was found in pXXL structures due to their higher stiffness while pXL structures presented lower magnitudes. Even though the alternating voltage presented significant different with change in frequency, the compressive forces did not (Figure 5-7).

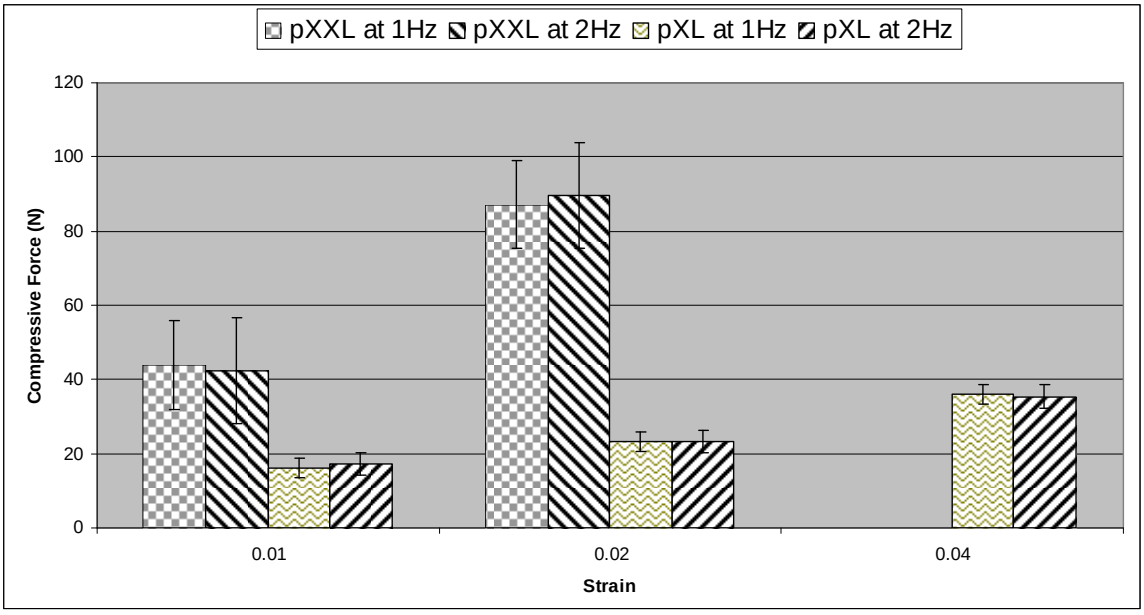

Figure 5-6. Average strain vs. compressive forces for all the structures at two difference frequencies. There was a small compressive force variation with different frequencies shown by small standard deviations.

It was hypothesized that if similar compressive forces were applied to each structure of the same type with similar dimensions, the forces transmitted to the piezo-plate surfaces would create similar electrical voltages due to the similar dimensions and materials used in each type of structures for pXL (n=5) and pXXL (n=5) structures. However, the results showed a great difference between electrical voltages in structures of the same type with similar dimensions. The electrical output is directly related to the forces (Eq. 5-3) applied so if similar forces are applied, similar electrical voltages should be recorded. However, the recorded compressive forces were similar in each structure (mostly in pXL structures) but the electrical voltages had higher variations, which shows an inconsistent transmission of compressive forces to electrical outputs. The forces could be lost in the rotational moments at the edges or not transmitted equally through the structure due to manufacturing limitations. Figure 5-7 shows the different peak to peak voltages coming directly from each type of structure at 1Hz and 2Hz respectively. The lowest voltage peak to peak (V_{ppk}) recorded in the pXXL structures was around 107 mV at a strain value of 0.02 with a frequency of 2 Hz while the highest V_{ppk} for the pXXL

structures at similar strain and frequency was 1600 mV, almost one order of magnitude greater than the lowest value found in a structure with same dimensions. The V_{ppk} in pXL showed even higher variability having a highest value of 905 mV at 0.04 strain at 2Hz while the lowest value was around 70 mV more than 12 times smaller. The standard deviations shown in Figure 5-7 confirmed this variability in sometimes even higher than the actual values.

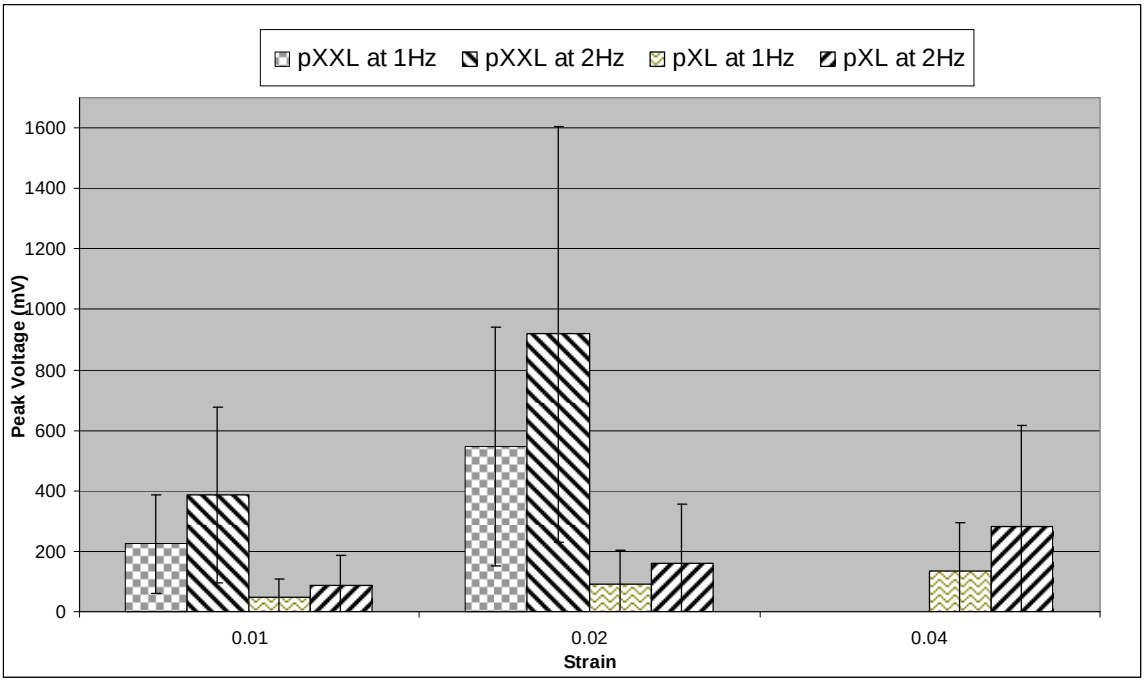

Figure 5-7. Average peak to peak voltage output of the structures at the different strain level when subjected to axial strain deformation at a frequency of 1Hz and 2Hz. Standard deviations shown as y-error bars show a great variability in the results.

Rectified signals:

The different variations in the output voltages lead to a high variation in rectified direct voltage outputs and thus in direct electrical currents. Table 5-2 shows the different direct electrical currents for all the structures at different strain levels. Standard deviation values are shown in parenthesis. The smaller the rectified voltage the smaller the direct

electrical current. Due to very high voltage drops in the electronic components used to build the rectifier; the direct electrical values (voltage and current) were very small compared to the peak voltage values. In some cases, the values were so small that were not detectable with the specific data acquisition system. This mostly occurred on the more flexible structures (pXL) when subjected to 0.01 and 0.02 strain. Thus, the pXL structures were subjected to a higher deformation up to 0.04 strain. There was only one pXL structure that presented significant electrical values around 0.01 and 0.02 strains (pXL5). The maximum direct current found from this investigation belongs to the stiffer pXXL structures at a higher frequency and deformation. pXXL2 at 0.02 strain with a frequency of 2 Hz presented a direct electrical current of 0.05 μA or 47 nA. Table 5-2 presents the different rectified voltages and rectified electrical currents at the three different strains: 0.01, 0.02, and 0.04. The highest pXL direct current was around 0.025μA or 25 nA when deformed up to a 0.04 strain value. A statistical difference between different structures could not be found due to the high variations in the results.

Strain: 0.01	**1Hz**		**2Hz**	
	V_{DC} (mV)	**I_{DC} (nA)**	**V_{DC} (mV)**	**I_{DC} (nA)**
pXL5	3.41 (0.51)	-	15.13 (2.40)	8
pXXL1	14.12 (0.86)	5	52.28 (2.42)	20
pXXL2	51.71 (1.42)	15	124.32 (3.66)	47
pXXL3	5.80 (0.50)	3	13.41 (0.96)	7
pXXL4	17.97 (1.33)	3	57.71 (2.04)	18
pXXL5	**-**	**-**	**-**	**-**

Table 5-2a. Rectified voltages and current for every structure when 0.01 strain was applied at 1Hz and 2Hz frequencies. Structures with immeasurable very small electrical values were not presented in this table.

Strain: 0.02	1Hz		2Hz	
	V_{DC} (mV)	I_{DC} (nA)	V_{DC} (mV)	I_{DC} (nA)
pXL5	22.44 (1.88)	8	45.38 (7.00)	12
pXXL1	15.27(1.23)	32	92.39 (7.34)	53
pXXL2	102.82 (4.54)	35	200.12 (3.00)	69
pXXL3	24.45 (0.75)	11	49.86 (2.65)	19
pXXL4	69.34 (8.2)	22	133.81 (4.70)	47
pXXL5	-	-	-	-

Table 5-2b. Rectified voltages and current for every structure when 0.02 strain was applied at 1Hz and 2Hz frequencies. Structures with immeasurable very small electrical values were not presented in this table.

Strain: 0.04	1Hz		2Hz	
	V_{DC} (mV)	I_{DC} (nA)	V_{DC} (mV)	I_{DC} (nA)
pXL1	5.73 (0.91)	-	16.45 (1.64)	4
pXL2	-	-	2.00 (0.81)	-
pXL3	4.25 (0.60)	-	13.61 (1.91)	6
pXL4	-	-	-	-
pXL5	42.17 (6.25)	17	83.20 (9.77)	25

Table 5-2c. Rectified voltages and current for pXL structures when 0.04 strain was applied at 1Hz and 2Hz frequencies. Structures with immeasurable very small electrical values were not presented in this table.

Finite Element Analysis:

For perfect surface bonding in pXL and pXXL structures, stress distribution was simulated in the y-direction, and the results presented in Figure 5-8**.** Unexpected results were found in the axial stress distribution around the piezoelectric-plates. Axial compressive and axial tensional stresses were found only in a small region around the corners of each model. The middle region of the structure modeled did not present any significant axial stress concentration showing an inefficient use of the piezoelectric material and geometry. The pXL model presented similar behavior to the pXXL model when fully bonded interaction was modeled but with lower stress magnitudes due to a more flexible structure (Figure 5-9). Magnitude scale presented in each graph is fixed to

±10MPa (±1*10^7 Pa). However, the higher and lower values outside the standard range are also presented in the scale with the brightest grey and darkest black color, respectively.

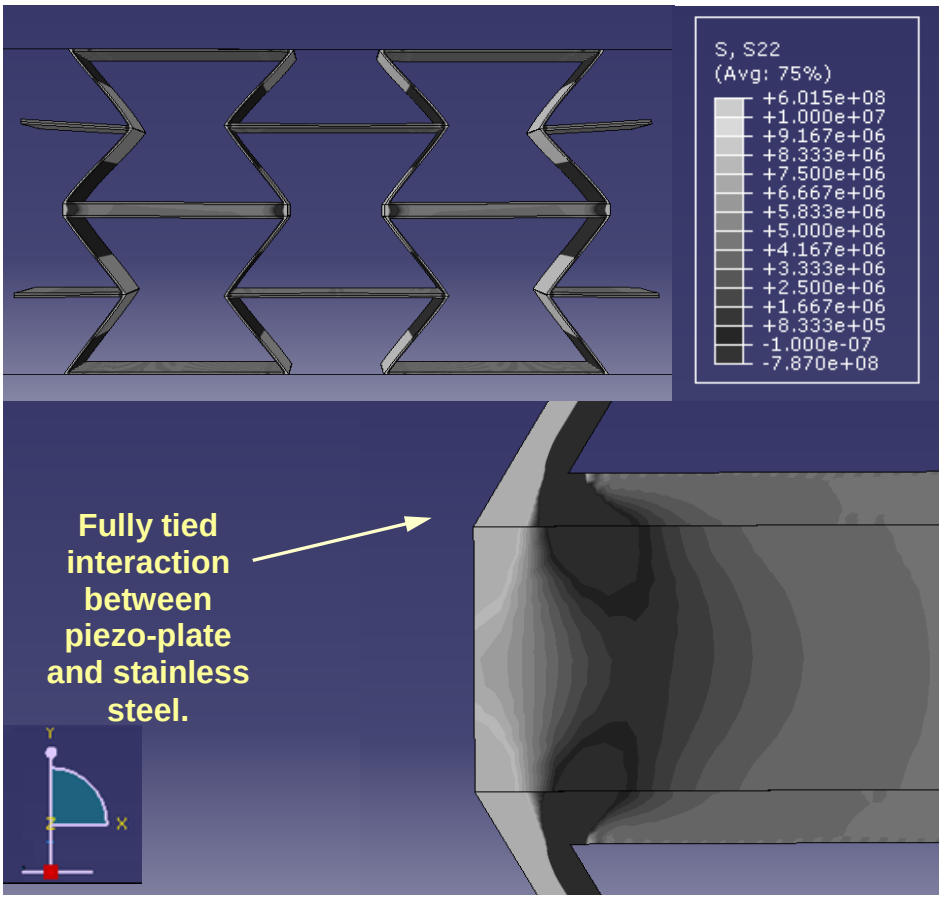

Figure 5-8. pXXL stress distribution in the y-direction (S_{22}) when fully bonded. Model presents compressive and tensional stresses at the corners of each structure. Very small stresses were presented at the middle surface of the piezoelectric plates.

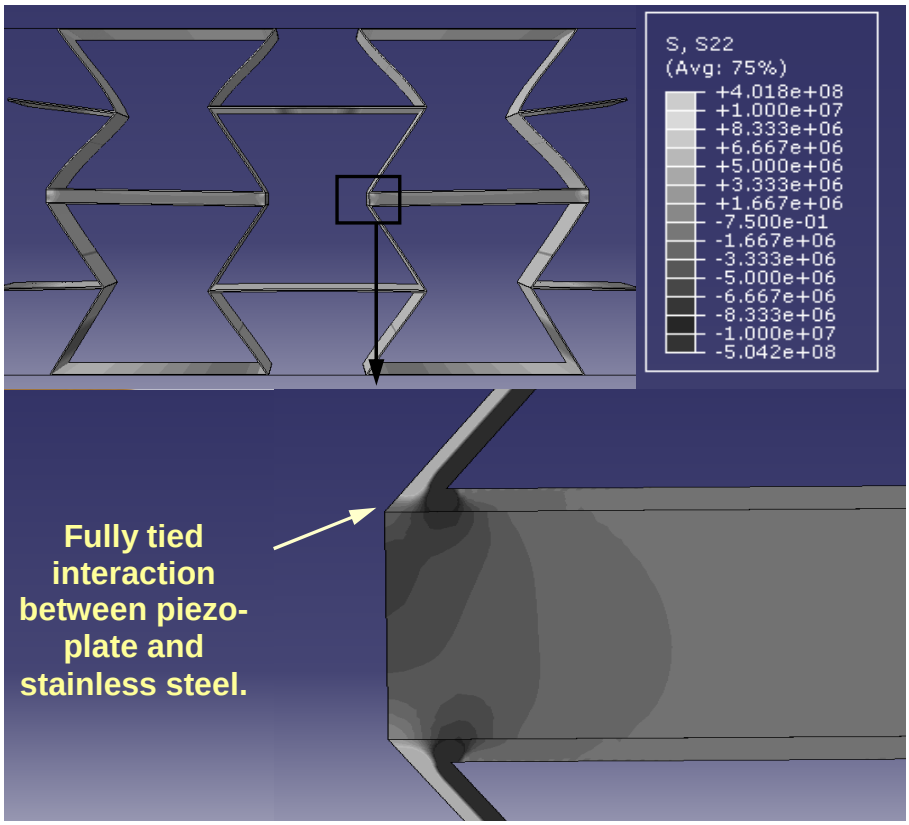

Figure 5-9. Stress distribution in the y-direction of the pXL model fully bonded.

Three additional models with separated contact interactions at the corners were modeled in each structure (pXL and pXXL). The separation length at the corners were 0.2, 1.0 and 2.0 mm. Figure 5-10 shows the different results in the pXXL models with different separation values. A great variation in the stress distribution was found which could explain the output voltage differences between structures with same dimension during experimental testing.

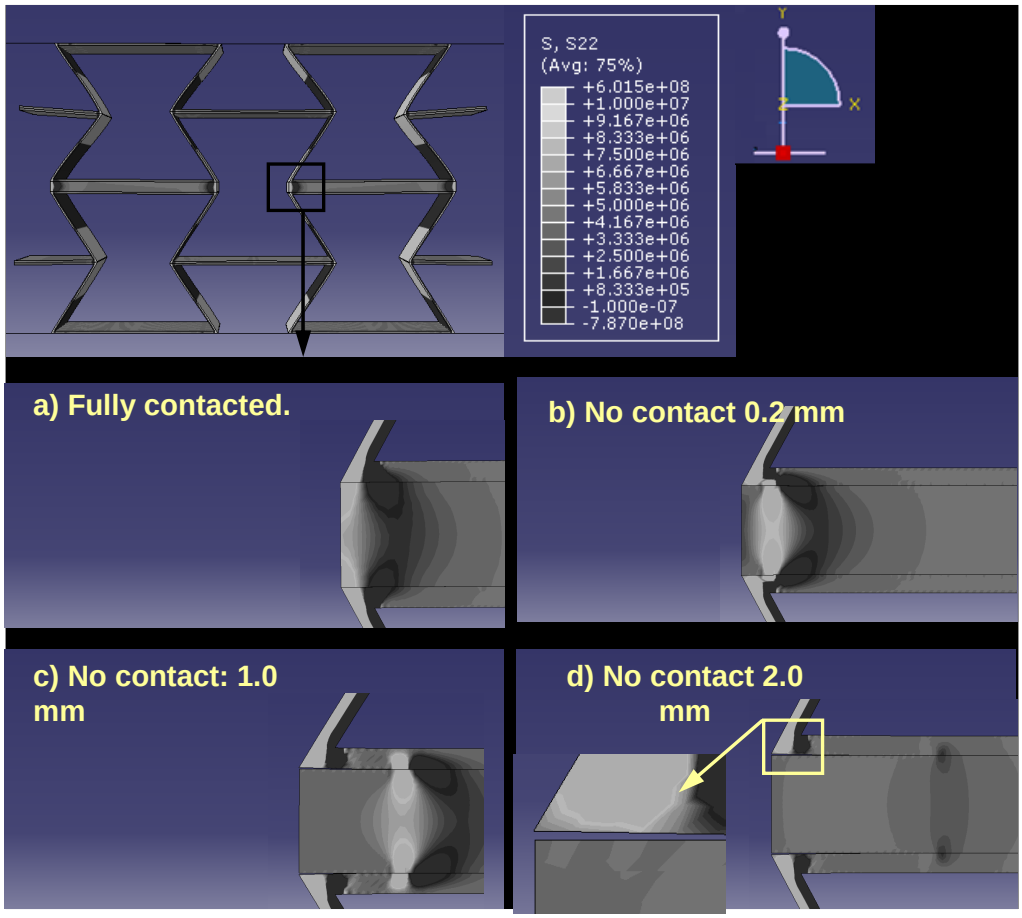

Figure 5-10. Stress distribution in the y-direction of the pXXL models. a) Shows fully contact interaction while b), c) and d) show no contact length interaction of 0.2, 1.0 and 2.0 mm respectively.

Due to the tensional stresses found in the perfectly bonded model, the metallic edges of the structure tended to lift up in the axial plane. With allowed separation, the tension stresses shifts to where the tie interaction begins and has a lower magnitude. The effect becomes greater when the non-bonded length increases. In the case of 2.0 mm non bonded region, no occurrence of tension was found in the stress distribution. Additionally, the piezoelectric plates had the lowest compressive stresses. As shown in Figure 5-10, there is a great variation between stresses in structures with different bonding that could explain the variation of the output voltage recorded during experimental testing for structures with similar dimensions

In the case of pXL structures, Figure 5-11 also presents great variations in the stress distributions for every bonding condition but with smaller magnitudes. Small

variability was shown around the fully contacted interaction and the 0.2 mm of separated length at the corners. Though, a great difference in the axial stresses was found around 1.0 mm where two areas of compressive stresses appear rather than lifting of the edges as shown in the pXXL . This behavior shows that the corners of the metallic structure tend to deform downwards and buckle creating two regions of compressive stresses.

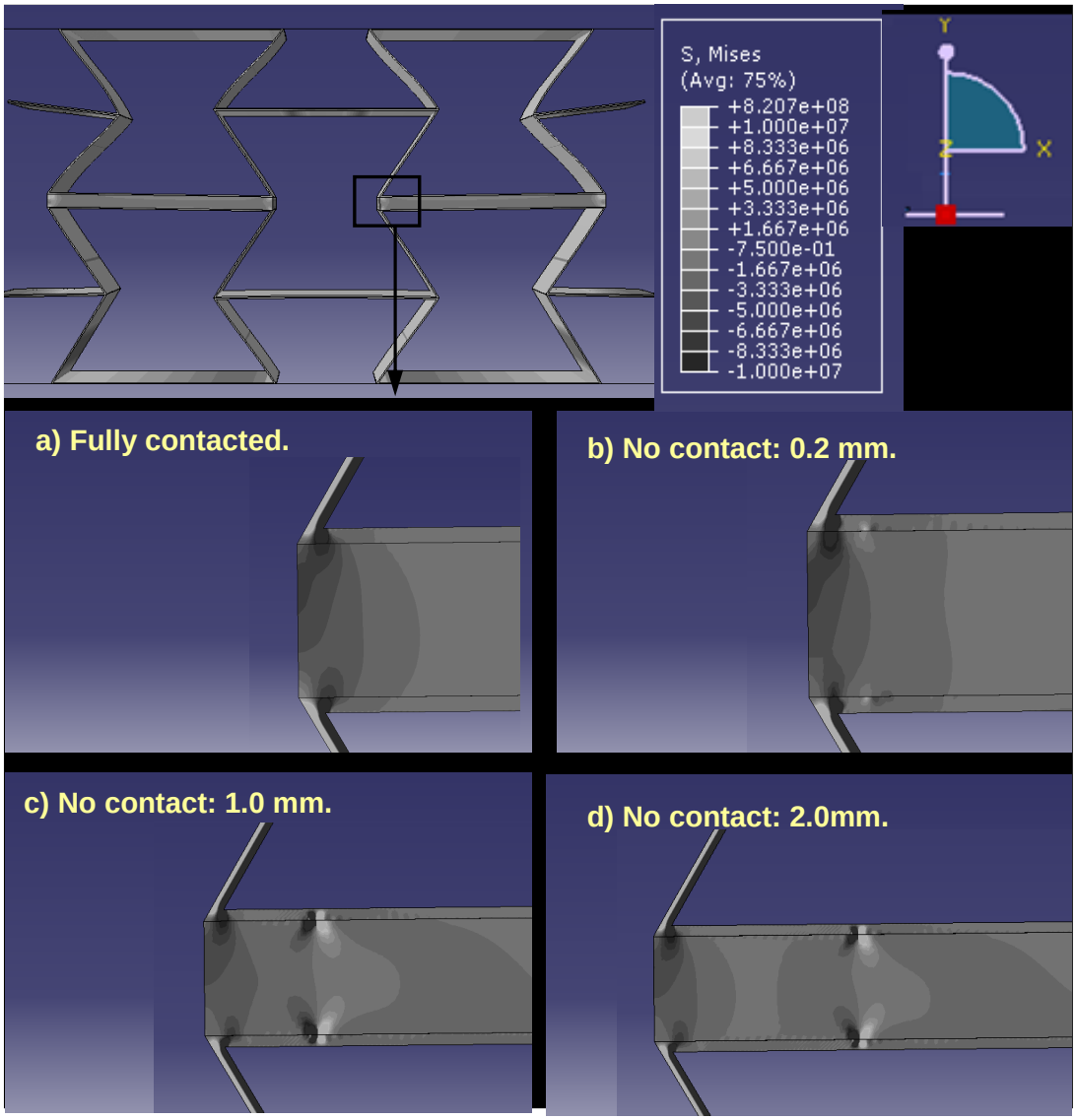

Figure 5-11. Stress distribution in the y-direction of the pXL models after separated contact interactions between piezo-plates and metallic structures at the corners.

Discussion:

Experimental:

The results showed that the cyclic compressive forces appeared to be unrelated to the frequency applied. Similar forces were found in equal dimension structures with changing frequencies at all strain levels. Small standard deviations support these results. On the other hand rectified alternating voltages were frequency dependant due to the piezoelectric instability at small frequencies (1Hz and 2Hz). Sufficient data on every structures proved that electrical signals can be generated from this type of structure when a compressive force is. Yet, recorded electrical voltages from similar type of structures showed great variability.

It was believed that voltage variation in similar dimension structures was due to variation on the compressive forces distributed around the piezoelectric ceramics as a result of poor manufacturing techniques and/or inadequate bonding between surfaces. This belief was supported by the results of finite element analysis (FEA) and close-up pictures. Microscope pictures (Figure 5-12) showed there was an inaccurate electrical bonding between the piezoelectric plates and the metallic structures. The most common unsuccessful bonding interaction was present around the corners of the structure but it was also present at the middle region of some piezoelectric surfaces providing sufficient evidence on why the results had a great variability.

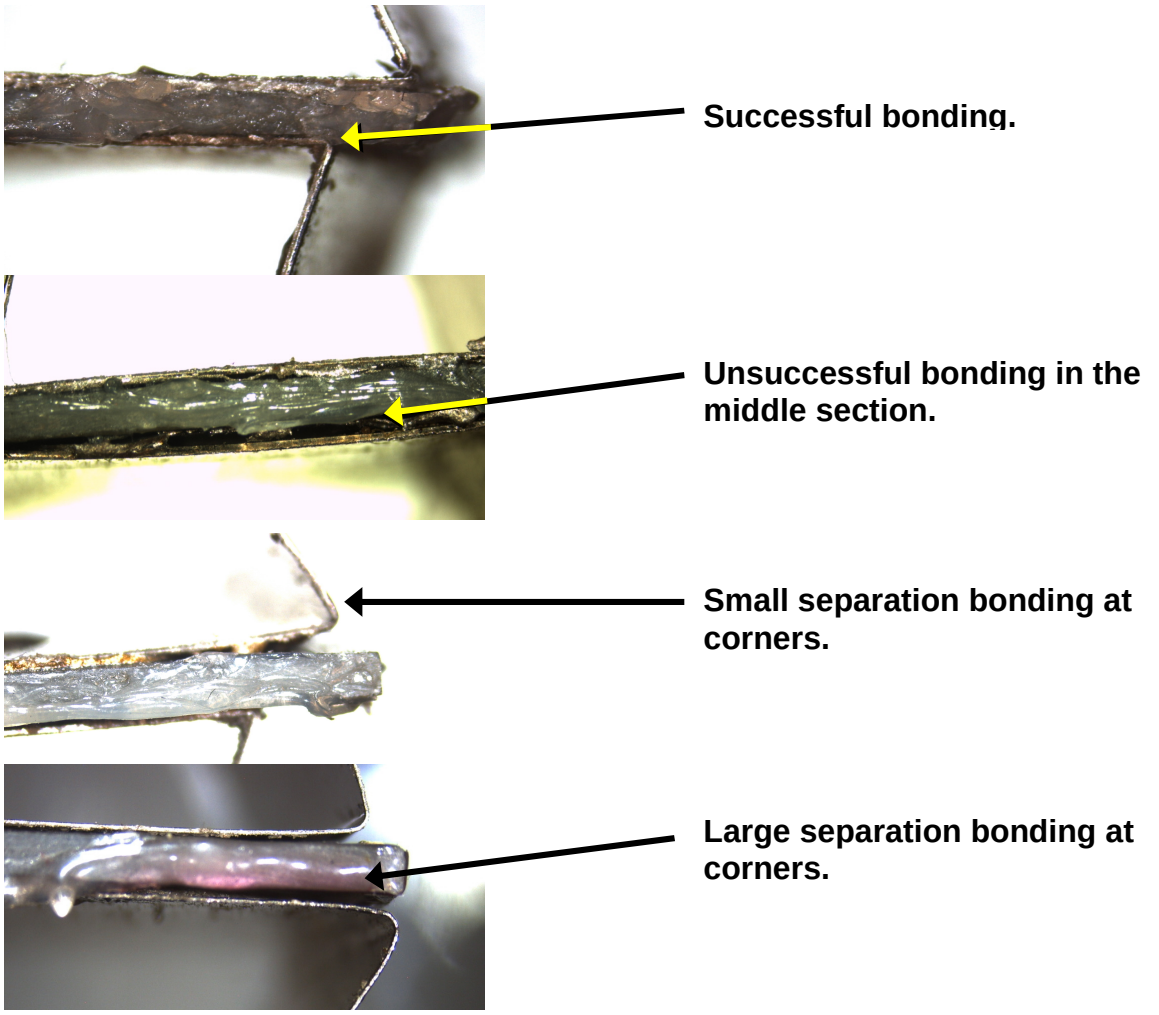

Figure 5-12. Piezoelectric structures showing the different manufacturing limitations where the piezo-plates were bonded into the metallic structures.

Finite Element Analysis:

For fully bonded models, it was expected that most all of the top and bottom surfaces were subjected to axial compressive stresses but instead axial compressive and tensional stresses were found only in a small region around the corners of each model. Due to the geometry of the structure, while deformation increases, the corners of the metallic material tend to bend creating tension at the corners and thus unexpected tension stresses, which will generate charges in the opposite direction. On the interior of the structure, near the areas of tension stresses, compressive stresses were transferred to the piezoelectric plate. pXL models with more flexibility, due to the thin metallic structures, presented similar behavior but smaller magnitudes when compared to the pXXL model when a fully contact interaction was applied (Figure 5-9). As expected, the magnitudes of the stresses were smaller due to the flexibility of the material but still tension and compressive stress regions were found. The appearance of tension stresses in these models generates electrical charges of opposite sign. These electrical charges would decrease the overall voltage magnitude, but since a greater area of compressive stresses is presented in both models, more charge in the desired direction overcomes the tension charges. This could explain the very low electrical signals found during experimental testing. The middle regions in the models (pXL and pXXL) did not carry any significant stress which showed an inefficient use of the piezoelectric material. Tension and compressive forces were only presented at the corners showing that the most influenced region for the variability of the results is located in the edges of each structure. Thus, three additional models with non-bonded contact interactions at the corners were modeled in each structure (pXL and pXXL).

A great variation in the stress distribution between models with different bonding simulation was found for each type of structure (pXL and pXXL). This could explained the great variability in voltage outputted from equal structures during experimental testing. There is a direct relationship between stresses and voltages, so stress variability should yield to variability in voltages. Figure 5-10 shows the difference in results in the pXXL models with different separation values. It was found that the more the contact

separation, the lower the compressive stress transferred to the piezoelectric plates. In addition, a lift up region is presented in the pXXL structure which shows the relieving of tensional stresses created in the perfectly bonded model. When the contact separation between piezoplate and metallic structure is increased, the tension stress decreases. Also, the tension and compressive stresses tend to shift to the region where the contact interaction occurs. Similar behavior and stress locations were also present in the case of pXL models but in a smaller magnitude scale. Small changes were found between the fully contacted interaction and the 0.2 mm of separated length at the corners. However, a great difference was found with 1.0 mm separation, which the metallic material did not tend to lift up as shown in the pXXL model. Instead the metallic material tended to present two areas of compressive stresses, which showed that the structures tend to deform downwards with two compressive stress points. This behavior is likely due to the small stiffness and high flexibility of these structures, due to the thinner material.

To validate the FEA results with experimental testing, compressive forces in the upper surfaces were compared with experimental recorded compressive forces. Table 5-3 and Table 5-4 show the forces applied at the upper rigid body to each of the different models with different separations compared to the experimental forces collected for each structure and FEA model. FEA force values were higher in magnitude in all the models compared to experimental forces from pXXL and pXL structures. The ratio between compressive forces in the FEA models and pXXL structures were almost 3.5 greater with fully bonded contact interaction at a strain value of 0.01. The ratio for fully bonded models at 0.02 decreased to 2.4 times greater. The higher the strain value, the more surfaces in contact and thus the less difference between an optimal structure (FEA) and the current experimental results. There is no optimal approach to predict an accurate strain value during experimental testing due to uneven manufactured surface. Also error while manufacturing structures yielded to more flexible structures compared to FEA stiffer models. As the separation interaction increases, the forces in FEA decreased making the ratios as small as 1.5 times higher. These results support the theory that the electro-mechanical structures varied due to the present manufacturing limitations such as mechanical bonding and inaccurate manufacturing dimensions. Similar behavior was

found when comparing the pXL structures with the different surface contact models. The ratio values for the pXL structures and models are presented in Table 5-4 Ratios varied from 3 times higher for fully contact models to 1.5 times higher for 2.0mm of separation as shown with the pXXL ratios.

Strain	**0.01**		**0.02**	
Experimental:	**Force (N)**	**FEA to Exp.**	**Force (N)**	**FEA to Exp.**
$pXXL_{AVG}$	43.79 (11.73)		87.16 (17.95)	
FEA:				
Full Contact	151.70	3.46	211.20	2.42
Separated (0.2mm)	91.74	2.09	185.00	2.12
Separated (1.0mm)	70.01	1.60	160.50	1.84
Separated (2.0mm)	62.43	1.43	151.80	1.74

Table 5-3. Experimental average forces of pXXL structures compared to the different FEA models at different interactions separations at the corners between the piezo-plates and the metallic structures.

Strain	**0.01**		**0.02**		**0.04**	
Experimental:	**Force (N)**	**FEA to Exp.**	**Force (N)**	**FEA to Exp.**	**Force (N)**	**FEA to Exp.**
pXL_{AVG}	20.55 (8.11)		25.51 (2.51)		34.34 (4.15)	
FEA:						
Full Contact	61.85	3.01	58.90	2.31	57.76	1.68
Separated (0.2mm)	62.13	3.02	59.01	2.31	57.34	1.67
Separated (1.0mm)	63.94	3.11	60.65	2.38	57.81	1.68
Separated (2.0mm)	27.43	1.33	50.00	1.96	63.24	1.84

Table 5-4. Experimental average forces of pXL structures compared to the different FEA models at different interactions separations at the corners between the piezo-plates and the metallic structures.

Even though there was variation in the results, it was shown that direct electrical stimulation could be achieved if adequate electronic components and adequate manufacturing process is used. There was a great voltage drop when voltages were rectified due to the electronic components used. Even though Schottky diodes were used with lower voltage drops (0.15-0.45 V) than normal diodes (0.7 – 1.7 V), they were still inadequate for this investigation since recorded voltages were smaller than predicted. However, proof of concept was achieved and with adequate electronic components such a precision rectifiers, higher magnitudes of direct electrical currents could be achieved. The highest direct electrical current found among all the structures was around 0.05 μA. According to standard considerations for electrical stimulators established by Cochran et. al. [29], values varied from 0.075 μA to 20 μA could enhance bone osteogenesis. Currently, the highest electrical current found in this investigation is too low to promote osteogenesis. If better electronic components are employed with a adequate bonding materials, the voltage drops will decrease resulting in higher voltage magnitudes and thus higher electrical.

Conclusion:

This study demonstrated proof of concept for the manufacture of novel metallic piezoelectric cellular solids with signal rectification, via recorded DC electrical values. Small voltages generated by the piezoceramics and the high voltage drops in the electronic components of the rectifier (such as with diodes and capacitors) resulted into very low DC electrical currents. The direct electrical current found (~0.05 μA) were smaller that the empirical value needed to enhance osteogenesis (0.75 to 20 μA). Further investigations with better electronic components (with lower voltage drops) could lead to higher direct voltages and electrical currents.

The high variability of the results was found to be due to a poor bonding and assembling when creating the specimens at this stage in the investigation. The stress

transferred through the piezo-plates occurred only at the corners of the structures according to FEA models, which showed an inefficient use of the piezoelectric material. Also inaccurate bonding at these regions was shown to yield to high variations on the stress distributions by the FEA analysis, and hence implicate bonding as the source of variability in the electrical output found in the experiments. Future investigations should consider a better geometry that would more appropriately incorporate the piezoelectric materials. A better geometry could be found by simulation using FEA. Once an adequate geometry is found, the structures must be manufactured with higher precision, since electrical behavior depends greatly in the forces transferred to the piezoelectric section. Rapid prototyping or solid free form fabrication should be considered. Despite limitations in this study, a DC electrical current was detected. The feasibility for a new generation on spine fusion implantable devices that can provide electrical stimulation together with efficient mechanical behavior has been established this investigation. Further investigations with new methodologies and different geometries but applying the same principles should follow this investigation to move this technology forward.

References:

[1]. Neuwirth, M., and Osborn, K., 2001, The scoliosis sourcebook, McGraw-Hill.
[2]. Surgery.com, "Spinal Fusion: Deomgraphics," http://www.surgery.com/procedure/spinal-fusion/demographics.
[3]. Brighton, C., Wang, W., Seldes, R., Zhang, G., and Pollack, S., 2001, "Signal transduction in electrically stimulated bone cells," The journal of bone and joint surgery, 83(10), p. 1514.
[4]. Fredericks, D., Petersen, E., Bobst, J., Gan, J., Simon, B., and Nepola, J., 2004, "Effects of capacitive coupling electrical stimulation on expression of growth factors in a rabbit posterolateral spine fusion model," North American Spine Society, Chicago.
[5]. France, J., Norman, T., Santrock, R., McGrath, B., and Simon, B., 2001, "The efficacy of direct current stimulation for lumbar intertransverse process fusions in an animal model," Spine, 26(9), p. 1002.
[6]. Marks, R. A., 2000, "Spine fusion for discogenic low back pain: outcomes in patients treated with or without pulsed electromagnetic field stimulation," Adv Ther, 17(2), pp. 57-67.
[7]. Meril, A. J., 1994, "Direct Current Stimulation of Allograft in Anterior and Posterior Lumbar Interbody Fusions. Lumbar Spine Surgery," Spine, 19(21), pp. 2393-2398.
[8]. Kane, W. J., 1979, "Facilitation of lumbosacral fusions by means of electronic bone growth stimulation," Scoliosis Research Society, Seattle.
[9]. Kane, W. J., 1988, "Direct current electrical bone growth stimulation for spinal fusion."
[10]. Park, J., Von Recum, A., Kenner, G., Kelly, B., Coffeen, W., and Grether, M., 1980, "Piezoelectric ceramic implants: A feasibility study," Journal of Biomedical Materials Research, 14(3), pp. 269-277.
[11]. Park, J., Kelly, B., and Kenner, G., 1981, "Piezoelectric ceramic implants--in vivo results," Journal of Biomedical Materials Research, 15, pp. 103-110.
[12]. Platt, S. R., Farritor, S., Garvin, K., and Haider, H., 2005, "The use of piezoelectric ceramics for electric power generation within orthopedic implants," IEEE/ASME Transactions on Mechatronics, 10(4), pp. 455-461.
[13]. Cowan, M., Riley, R., Brisken, A., and Echt, D., 2007, "Systems and methods for implantable leadless spine stimulation," United States Patent Application 20070293909
[14]. Demarest, K., 1998, Engineering electromagnetics, Prentice Hall.
[15]. Piezo_Systems_INC, 2008, "PSI-5A4E Piezoceramic Sheets and Their Properties," Electronic Version, http://www.piezo.com/prodsheet1sq5A.html.
[16]. Precision_Brand, 2009, "Stainless Steels Chromium-Nickel Types 302 (S30200), 304 (S30400), 304L (S30403),305 (S30500," Allegheny Ludlum Corporation, Pittburg.
[17]. Karsen, S. R. B. a. C. D. V., 1992, "Mechanical Fatigue Properties of Stress Relieved Type 302 Stainless Steel Wire," Journal of Materials Engineering and Performance, 1(3).

[18]. Meril, A. J., 1994, "Direct current stimulation of allograft in anterior and posterior lumbar interbody fusions," Spine, 19(21), pp. 2393-2398.
[19]. Yasuda, I., 1977, "Electrical callus and callus formation by electret," Clinical orthopaedics and related research(124), p. 53.
[20]. White, A., and Panjabi, M., 1990, Clinical biomechanics of the spine, Lippincott Philadelphia.
[21]. Becker, R., Spadaro, J., and Marino, A., 1977, "Clinical experiences with low intensity direct current stimulation of bone growth," Clinical orthopaedics and related research(124), p. 75.
[22]. Collier, M. A., Brighton, C. T., Rendano, V. T., Schryver, H. F., and Kallfelz, F. A., 1985, "Direct current stimulation of bone production in the pony: observations with a diaphyseal osteotomy mode," American journal of veterinary research (USA).
[23]. Kucharzyk, D. W., 1999, "A controlled prospective outcome study of implantable electrical stimulation with spinal instrumentation in a high-risk spinal fusion population," Spine, 24(5), pp. 465-468; discussion 469.
[24]. Rogozinski, A., and Rogozinski, C., 1996, "Efficacy of implanted bone growth stimulation in instrumented lumbosacral spinal fusion," Spine, 21(21), p. 2479.
[25]. Salman, N., and Park, J., 1980, "The effect of direct electrical current stimulation on the bone/porous metallic implant interface," Biomaterials, 1(4), p. 209.
[26]. Spadaro, J., 1982, "Bioelectric Stimulation of Bone Formation: Methods, Models, and Mechanisms," Electromagnetic Biology and Medicine, 1(1), pp. 99-128.
[27]. Tejano, N. A., Puno, R., and Ignacio, J. M., 1996, "The use of implantable direct current stimulation in multilevel spinal fusion without instrumentation. A prospective clinical and radiographic evaluation with long-term follow-up," Spine, 21(16), pp. 1904-1908.
[28]. Hart, D., 1996, Introduction to power electronics, Prentice Hall PTR Upper Saddle River, NJ, USA.
[29]. Cochran G.V.B., Johnson, M., Yv, P., and KADABA, P., "Design considerations in development of a prototype, piezoelectric internal fixation plate: A preliminary report."
[30] Bechmann, R. (1953). "The linear piezoelectric equations of state." British Journal of Applied Physics **4**: 210.

Chapter 6: Conclusion and Future Work

Conclusion

Mechanical and electro-mechanical structures of novel cellular solid piezo-metallic composites were characterized for possible use in spine fusion. It was hypothesized that controllable cellular bowties could be tailored to resemble mechanical characteristics of cancellous bone while providing electrical stimulation.

Results of mechanical evaluation for different structures with similar relative densities presented comparable mechanical behavior in stress-strain curves and modulus of elasticity. It was validated that changing the relative density of the cellular solid controlled the mechanical behavior of the structure. More accurate materials for potential bone grafts and the change of aspect ratios/relative densities could then be tailored to mimic the mechanical behavior of the tissue designated to be replaced. Controllable parameters of cellular solids and adequate biocompatible materials could yield to a very adaptable environment with similar characteristics as the bone tissues.

Non-linear behavior [36] of cancellous bone was hypothesized to be demonstrated by re-entrant structures. A previous study showed that re-entrant structures possess this characteristic [73]. However, it was concluded that the re-entrant bow-tie structure used in this study did not present true non-linearity at small strains. Previous investigations on the bowtie structure that showed non-linearity could be explained by experimental and specimen artifacts. The structures presented non-linear regions of behavior at small strains due to limitations in prototype manufacturing technique that produced uneven contact surfaces in the specimen. It was concluded that the nonlinearity was due to uneven surfaces coming in contact with the compressive platens at different times. When uniform contact is achieved between surfaces and compressive load platens, true linear behavior was presented. Finite element analysis (FEA) supported this conclusion by showing that every structure presented linear behavior similar to the values found during experimental linear regions, but with no non-linearity.

Feasibility of providing electrical stimulation through the graft materials was analyzed experimentally by embedding piezoelectric plates into the metallic bow-tie cellular solids. The ac voltages generated by applying compressive loads were rectified to provide a dc electrical current and results compared to previous electrical stimulation studies shown to enhance bone growth. Direct electrical current magnitudes found were smaller than those currents known to enhance bone osteogenesis. This was mainly due to manufacturing shortcomings and inadequate electronic testing components. Results also showed a great variability in electrical output for the hand-crafted prototype bow-tie structures. Variability of the results was validated using finite element analysis. It was found that compressive and tensional stresses were found only at the corners of each piezo-plate, which utilized less than 10% of the entire piezo-plate electro-mechanical behavior. In addition, these contact areas under compression were the regions subjected to the highest inaccurate and variability when manufactured. Parametric finite element analysis of the bonding error explained the variability between the experimental results. Better geometries with adequate electronic components and optimal manufacturing processes would most certainly create electrical currents high above the magnitudes necessary to enhance bone osteogenesis.

Future Work

The present research project utilized handcrafted prototype bowtie piezo-ceramic metallic composite cellular solids and FEA models. This geometry presented two-dimensional re-entrant behavior. Future investigations could focus on more advanced manufacturing processes for piezo-metallic cellular metallic structures. Potential 2-D or 3-D cellular solid structures with smaller dimensions could be first analyzed with FEA to develop the most adequate geometry where the use of piezo-plates is maximized. Once an adequate geometry with efficient piezoelectric utilization can be validated, a manufacturing process could begin. Manufacturing techniques should be improved greatly as it has been proven to be the main cause of variability in the results. Rapid prototyping or robotic-based free-form manufacturing techniques for manufacturing could be employed with adequate biocompatible piezoelectric materials and metallic cellular solid structures. Additionally, higher number of specimens with same geometries/dimensions should be manufactured to provide a statistical significance. More accurate electronic components need to be utilized to avoid high voltage drops. A precision rectifier could replace the simple full bridge rectification used in this study with Schottky diodes.

References:

.

[1]. Hart, D., 1996, Introduction to power electronics, Prentice Hall PTR Upper Saddle River, NJ, USA.

[2]. Gibson, L., and Ashby, M., 1999, Cellular solids: structure and properties, Pengamon Press.

[3]. D. Sculley, T. U., 2004, "Electronics Tutorial for Robotics," http://www.eecs.tufts.edu/~dsculley/tutorial/.

[4]. Simulia, I., 2008, "Abaqus User Manual v6. 8," Electronic Version.

[5]. Back.com, 2009, "Anatomy Lumbar," http://www.back.com/anatomy-lumbar.html.

[6]. WebMD, 2008, "Herniated Disc," http://www.webmd.com/hw-popup/herniated-disc.

[7]. Jaumard, N., 2008, "Mechanical and electromechanical characterization of a novel composite cellular solid for orthopaedic applications: A feasibility study," PhD, The University of Kansas, Lawerence.

[8]. Becker, R. O., 1978, "Electrical osteogenesis--pro and con," Calcif Tissue Res, 26(2), pp. 93-97.

[9]. Bowen, S. P., Mancini, J. D., Fessatidis, V., and Grabiner, M., 2008, "Why do electromagnetic pulses enhance bone growth?," Ann Biomed Eng, 36(2), pp. 195-203.

[10]. Collier, M. A., Brighton, C. T., Rendano, V. T., Schryver, H. F., and Kallfelz, F. A., 1985, "Direct current stimulation of bone production in the pony: observations with a diaphyseal osteotomy mode," American journal of veterinary research (USA).

[11]. Gan, J. C., and Glazer, P. A., 2006, "Electrical stimulation therapies for spinal fusions: current concepts," European Spine Journal, 15(9), pp. 1301-1311.

[12]. Steinberg, M. E., 1974, "Stress-induced potentials in moist bone in vitro," JBJS, pp. 704-713.

[13]. Toth, J. M., Seim, H. B., 3rd, Schwardt, J. D., Humphrey, W. B., Wallskog, J. A., and Turner, A. S., 2000, "Direct current electrical stimulation increases the fusion rate of spinal fusion cages," Spine, 25(20), pp. 2580-2587.

[14]. Surgeons, A. A. o. O., 2007, "Spinal Fusion," http://orthoinfo.aaos.org/topic.cfm?topic=a00348.

[15]. Kane, W. J., 1988, "Direct current electrical bone growth stimulation for spinal fusion."

[16]. Tejano, N. A., Puno, R., and Ignacio, J. M., 1996, "The use of implantable direct current stimulation in multilevel spinal fusion without instrumentation. A prospective clinical and radiographic evaluation with long-term follow-up," Spine, 21(16), pp. 1904-1908.

[17]. Meril, A. J., 1994, "Direct Current Stimulation of Allograft in Anterior and Posterior Lumbar Interbody Fusions. Lumbar Spine Surgery," Spine, 19(21), pp. 2393-2398.

[18]. Kane, W. J., 1979, "Facilitation of lumbosacral fusions by means of electronic bone growth stimulation," Scoliosis Research Society, Seattle.

[19]. Park, J., Von Recum, A., Kenner, G., Kelly, B., Coffeen, W., and Grether, M., 1980, "Piezoelectric ceramic implants: A feasibility study," Journal of Biomedical Materials Research, 14(3), pp. 269-277.
[20]. Park, J., Kelly, B., and Kenner, G., 1981, "Piezoelectric ceramic implants--in vivo results," Journal of Biomedical Materials Research, 15, pp. 103-110.
[21]. Platt, S. R., Farritor, S., Garvin, K., and Haider, H., 2005, "The use of piezoelectric ceramics for electric power generation within orthopedic implants," IEEE/ASME Transactions on Mechatronics, 10(4), pp. 455-461.
[22]. Cowan, M., Riley, R., Brisken, A., and Echt, D., 2007, "Systems and methods for implantable leadless spine stimulation," Application number: 11/764,574 Publication number: US 2007/0293909 A1 Filing date: Jun 18, 2007
[23]. Fitzsimmons, R., Ryaby, J., Mohan, S., Magee, F., and Baylink, D., 1995, "Combined magnetic fields increase insulin-like growth factor-II in TE-85 human osteosarcoma bone cell cultures," Endocrinology, 136(7), p. 3100.
[24]. McElhaney, J. H., 1967, "The charge distribution on the human femur due to load," J Bone Joint Surg Am, 49(8), pp. 1561-1571.
[25]. Applegate, E., 1995 "The Anatomy and Physiology Learning System: Textbook. WB Philadelphia: Saunders Company," Links.
[26]. Van De Graaff, K., 1998, Human anatomy, William C Brown Pub.
[27]. Wolff, J., 1869, "Ueber die bedeutung der architectur der spongiösen substanz für die frage vom knochenwachsthum," Zentralblatt für die Medizinischen Wissenschaften, 6, pp. 223-234.
[28]. Curry, J., 1984, "The mechanical adaptations of bones," New Jersey: Princeton.
[29]. Keith Bridwell, M., 1999-2009, http://www.spineuniverse.com/displayarticle.php/article1286.html.
[30]. White, A., and Panjabi, M., 1990, Clinical biomechanics of the spine, Lippincott Philadelphia.
[31]. Nachemson, A., and Morris, J., 1964, "In vivo measurements of intradiscal pressure: Discometry, a method for the determination of pressure in the lower lumbar discs," The journal of bone and joint surgery, 46(5), p. 1077.
[32]. Panagiotacopulos, N., Pope, M., Bloch, R., and Krag, M., 1987, "Water content in human intervertebral discs: Part II. Viscoelastic behavior," Spine, 12(9), p. 918.
[33]. Gerald, R., MD, 2008, "What should I know about lumbar spine," http://www.spineuniverse.com/displayarticle.php/article600.html.
[34]. Cook, S., Reynolds, M., Whitecloud, T., Routman, A., Harding, A., KAY, J., and Jarcho, M., 1986, "Evaluation of hydroxylapatite graft materials in canine cervical spine fusions," Spine, 11(4), p. 305.
[35]. Jacobs, C. R., 2000, "The mechanobiology of cancellous bone structural adaptation," J Rehabil Res Dev, 37(2), pp. 209-216.
[36]. Morgan, E. F., Yeh, O. C., Chang, W. C., and Keaveny, T. M., 2001, "Nonlinear behavior of trabecular bone at small strains," J Biomech Eng, 123(1), pp. 1-9.
[37]. Keaveny, T. M., Guo, X. E., Wachtel, E. F., McMahon, T. A., and Hayes, W. C., 1994, "Trabecular bone exhibits fully linear elastic behavior and yields at low strains," J Biomech, 27(9), pp. 1127-1136.
[38]. Burr, D., Martin, R., Schaffler, M., and Radin, E., 1985, "Bone remodeling in response to in vivo fatigue microdamage," J Biomech, 18(3), pp. 189-200.

[39]. Lee, T., Arthur, T., Gibson, L., and Hayes, W., 2000, "Sequential labelling of microdamage in bone using chelating agents," Journal of Orthopaedic research, 18(2).
[40]. Martin, R., 2002, "Is all cortical bone remodeling initiated by microdamage?," Bone, 30(1), pp. 8-13.
[41]. Bassett, C. A., 1968, "Biologic significance of piezoelectricity," Calcif Tissue Res, 1(4), pp. 252-272.
[42]. Chakkalakal, D., Johnson, M., Harper, R., and Katz, J., 1980, "Dielectric properties of fluid-saturated bone," IEEE Transactions on Biomedical Engineering, pp. 95-100.
[43]. Johnson, M., Chakkalakal, D., Harper, R., and Katz, J., 1980, "Comparison of the electromechanical effects in wet and dry bone," J Biomech, 13, pp. 437-442.
[44]. Baranowski, T., Black, J., Brighton, C., and Friedenberg, Z., 1983, "Electrical osteogenesis by low direct current," Journal of Orthopaedic research, 1(2), pp. 120-128.
[45]. Ohashi, T., 1982, "Electrical callus formation and its osteogenesis," Nippon Seikeigeka Gakkai zasshi, 56(7), p. 615.
[46]. Gjelsvik, A., 1973, "Bone remodeling and piezoelectricity. I," Journal of biomechanics, 6(1), p. 69.
[47]. Korostoff, E., 1977, "Stress generated potentials in bone: relationship to piezoelectricity of collagen," Journal of biomechanics, 10(1), p. 41.
[48]. Fukada, E., and Yasuda, I., 1957, "On the piezoelectric effect of bone," J. Phys. Soc. Japan, 12, pp. 1158-1162.
[49]. Reinish, G., and NOWICK, A., 1975, "Piezoelectric properties of bone as functions of moisture content."
[50]. Bur, A., 1976, "Measurements of the dynamic piezoelectric properties of bone as a function of temperature and humidity," Journal of biomechanics, 9(8), p. 495.
[51]. Lakes, R., Harper, R., and Katz, J., 1977, "Dielectric relaxation in cortical bone," Journal of Applied Physics, 48(2), pp. 808-811.
[52]. Park, J., and Lakes, R., 2007, Biomaterials: an introduction, Springer Verlag.
[53]. Athenstaedt, H., 1969, "Permanent electric polarization and pyroelectric behaviour of the vertebrate skeleton. IV. The cranial bones of man," Zeitschrift für Zellforschung und mikroskopische Anatomie (Vienna, Austria: 1948), 97(4), p. 537.
[54]. Athenstaedt, H., 1974, "Pyroelectric and piezoelectric properties of vertebrates," Annals of the New York Academy of Sciences, 238(1 Electrically Mediated Growth Mechanisms in Living Systems), pp. 68-94.
[55]. Lang, S., 1966, "Pyroelectric effect in bone and tendon."
[56]. Becker, R., Spadaro, J., and Marino, A., 1977, "Clinical experiences with low intensity direct current stimulation of bone growth," Clinical orthopaedics and related research(124), p. 75.
[57]. Yasuda, I., 1977, "Electrical callus and callus formation by electret," Clinical orthopaedics and related research(124), p. 53.
[58]. Kucharzyk, D. W., "A controlled prospective outcome study of implantable electrical stimulation with spinal instrumentation in a high-risk spinal fusion population."

[59]. Marino, A., and Becker, R. O., 1970, "Piezoelectric effect and growth control in bone," Nature, 228(5270), pp. 473-474.
[60]. Rogozinski, A., and Rogozinski, C., 1996, "Efficacy of implanted bone growth stimulation in instrumented lumbosacral spinal fusion," Spine, 21(21), p. 2479.
[61]. Goodwin, C., Brighton, C., Guyer, R., Johnson, J., Light, K., and Yuan, H., 1999, "A double-blind study of capacitively coupled electrical stimulation as an adjunct to lumbar spinal fusions," Spine, 24(13), p. 1349.
[62]. Aaron, R., Wang, S., and Ciombor, D., 2002, "Upregulation of basal TGFb1 levels by EMF coincident with chondrogenesis-implications for skeletal repair and tissue engineering," Journal of Orthopaedic research, 20(2), pp. 233-240.
[63]. Bodamyali, T., Bhatt, B., Hughes, F., Winrow, V., Kanczler, J., Simon, B., Abbott, J., Blake, D., and Stevens, C., 1998, "Pulsed Electromagnetic Fields Simultaneously Induce Osteogenesis and Upregulate Transcription of Bone Morphogenetic Proteins 2 and 4 in Rat Osteoblastsin Vitro," Biochemical and Biophysical Research Communications, 250(2), pp. 458-461.
[64]. Aaron, R., Boyan, B., Ciombor, D., Schwartz, Z., and Simon, B., 2004, "Stimulation of growth factor synthesis by electric and electromagnetic fields," Clinical orthopaedics and related research, 419, p. 30.
[65]. Guerkov, H., Lohmann, C., Liu, Y., Dean, D., Simon, B., Heckman, J., Schwartz, Z., and Boyan, B., 2001, "Pulsed electromagnetic fields increase growth factor release by nonunion cells," Clinical orthopaedics and related research, 384, p. 265.
[66]. Smith, T., Wong-Gibbons, D., and Maultsby, J., 2004, "Microcirculatory effects of pulsed electromagnetic fields," Journal of Orthopaedic research, 22(1), pp. 80-84.
[67]. Brighton, C., Wang, W., Seldes, R., Zhang, G., and Pollack, S., 2001, "Signal transduction in electrically stimulated bone cells," The journal of bone and joint surgery, 83(10), p. 1514.
[68]. Ryaby, J., Fitzsimmons, R., Khin, N., Culley, P., Magee, F., Weinstein, A., and Baylink, D., 1994, "The role of insulin-like growth factor II in magnetic field regulation of bone formation," Bioelectrochemistry and Bioenergetics, 35(1), pp. 87-92.
[69]. Simmons, J. W., 1985, "Treatment of failed posterior lumbar interbody fusion (PLIF) of the spine with pulsing electromagnetic fields," Clin Orthop Relat Res(193), pp. 127-132.
[70]. Linovitz, R., Pathria, M., Bernhardt, M., Green, D., Law, M., McGuire, R., Montesano, P., Rechtine, G., Salib, R., and Ryaby, J., 2002, "Combined magnetic fields accelerate and increase spine fusion: a double-blind, randomized, placebo controlled study," Spine, 27(13), p. 1383.
[71]. Choi, J., and Lakes, R., 1992, "Non-linear properties of polymer cellular materials with a negative Poisson's ratio," Journal of Materials Science, 27(17), pp. 4678-4684.
[72]. Wyman, J., 1865, "Notes on the Cells of the Bee," pp. 68-83.
[73]. Friis, E., Lakes, R., and Park, J., 1988, "Negative Poisson's ratio polymeric and metallic foams," Journal of Materials Science, 23(12), pp. 4406-4414.
[74]. Yang, J., 2005, An introduction to the theory of piezoelectricity, Springer.

[75]. Daining, F., Soh, A., and Jinxi, L., 2001, "Electromechanical deformation and fracture of piezoelectric/ferroelectric materials," Acta Mechanica Sinica, 17(3), pp. 193-213.
[76]. Jaffe, B., Cook, W., and Jaffe, H., 1971, Piezoelectric ceramics, Academic Press London.
[77]. Wul, B., and Goldman, I., 1945, "Dielectric constants of titanates of metals of the second group," pp. 154-157.
[78]. Piezo_Systems_INC, 2008, "Piezoelectric Terminology," Electronic Version, http://www.piezo.com/tech1terms.html.
[79]. Ikeda, T., 1990, Fundamentals of piezoelectricity, Oxford University Press Oxford.
[80]. Demarest, K., 1998, Engineering electromagnetics, Prentice Hall.
[81]. Fish, J., and Belytschko, T., 2007, A first course in Finite Elements, Wiley.
[82]. Gerald, C., and Wheatley, P., "Applied Numerical Analysis. 2004," Addison-Wesley Publishing Company.
[83]. Documentation, A., 2007, "Getting Started with Abaqus Interactive Edition," Version.
[84]. France, J., Norman, T., Santrock, R., McGrath, B., and Simon, B., 2001, "The efficacy of direct current stimulation for lumbar intertransverse process fusions in an animal model," Spine, 26(9), p. 1002.
[85]. Spadaro, J., 1982, "Bioelectric Stimulation of Bone Formation: Methods, Models, and Mechanisms," Electromagnetic Biology and Medicine, 1(1), pp. 99
[86]. Precision_Brand, 2009, "Stainless Steels Chromium-Nickel Types 302 (S30200),304 (S30400), 304L (S30403),305 (S30500," Allegheny Ludlum Corporation, Pittburg.
[87]. Systems, P., "Piezoceramic Materials and Properties," http://piezo.com/prodmaterialprop.html.
[88]. Karsen, S. R. B. a. C. D. V., 1992, "Mechanical Fatigue Properties of Stress Relieved Type 302 Stainless Steel Wire," Journal of Materials Engineering and Performance, 1(3).
[89]. Meril, A. J., 1994, "Direct current stimulation of allograft in anterior and posterior lumbar interbody fusions," Spine, 19(21), pp. 2393-2398.
[90]. Dep. Mechanical Engineering, C. M., "The Finite Element Method," http://www.me.cmu.edu/academics/courses/NSF_Edu_Proj/StrAnalysis_ANSYS/FEM.html.